UC San Diego

UC San Diego Electronic Theses and Dissertations

Title

Microscale Engineering of Phase Change and Radiation Heat Transfer

Permalink

https://escholarship.org/uc/item/9xb8s292

Author

Wang, Qingyang

Publication Date

2020

Peer reviewed|Thesis/dissertation

eScholarship.org Powered by the California Digital Library
University of California

UNIVERSTIY OF CALIFORNIA, SAN DIEGO

Microscale Engineering of Phase Change and Radiation Heat Transfer

A dissertation submitted in partial satisfaction of the requirements for the degree
Doctor of Philosophy

in

Engineering Sciences (Mechanical Engineering)

by

Qingyang Wang

Committee in charge:

Professor Renkun Chen, Chair
Professor Shengqiang Cai
Professor Carlos F. M. Coimbra
Professor Ping Liu
Professor David Saintillan

2020

Copyright

Qingyang Wang, 2020

All rights reserved

The Dissertation of Qingyang Wang is approved, and it is acceptable in quality and form for publication on microfilm and electronically:

_____

_____

_____

_____

_____

Chair

University of California, San Diego

2020

Dedication

Dedicated to my family for their unwavering love and support.

Table of Contents

List of Figures

Acknowledgements

I still remember on September 1, 2015, I landed in San Diego and moved into an empty apartment without even a mattress for sleep. I lay down on the carpet at night, struggled to fall asleep but could not due to jet lag, and I kept imagining about where at home I should hang my fancy PhD degree certificate after I graduate. Time flies, and I'm now finally approaching the end of my doctoral study I have been looking forward to. I knew the path to a PhD degree is never smooth, but I for sure didn't expect the many unimaginable difficulties and challenges I had to face and overcome along the way. Looking back, the past five years have been an incredibly enjoyable and valuable chapter of my life, and I must thank many great people who have made this journey successful and colorful.

First and foremost, I would like to express my deepest gratitude to my advisor, Prof. Renkun Chen, for his guidance, trust, encouragement, and inspiration throughout my PhD study. Renkun brought me into his research group five years ago when I just finished my undergraduate study and knew almost nothing about what a PhD student should do, and he magically shaped me into an independent researcher I have not even dreamed of being. Through countless meetings, discussions, lunches, dinners, happy hours, I have learned a lot from him, not only about fundamental knowledge and technical skills, but also about how to think critically and how to interact with people. The achievements I have made so far, if any, would be impossible without his persistent help and support. Renkun is a true mentor for me: his deep insights in heat transfer, his wide vision on engineering and technologies, his high standard for research, his dedicated attitude to work, and his great

patience for students, all make him a role model that I will try my best to become in my future career.

I am also deeply grateful to Prof. Carlos Coimbra, who gave me an incredible teaching opportunity as a graduate student. In Fall 2018, being the chair of the Dept. of MAE, Prof. Coimbra appointed me as the course instructor for the undergraduate level class MAE 101C-Heat Transfer. He trusted me to teach the class independently even though I didn't even have any TA experience, for which I was greatly honored. Teaching in Fall 2018 is indeed one of the best experiences I ever had in UCSD, through which I found out my love for teaching and interacting with students and eventually decided to become a professor. The 100% positive evaluations and the compliments from the students are truly one of the biggest accomplishments during my time at UCSD. Therefore, I also want to appreciate Dr. Mengying Li for her suggestions on how to teach, Zhouyi Liao for her help as the TA, and all the students who enrolled in my class for their trust in selecting me as their instructor, for their cooperation throughout the quarter, and for their recommendation and recognition of my teaching performance at the end of the quarter.

I would like to thank all my dissertation committee members, Prof. Carlos Coimbra, Prof. Shengqiang Cai, Prof. Ping Liu, and Prof. David Saintillan, for serving in my dissertation committee and providing valuable suggestions and comments for my research.

I am also thankful to Prof. Liang Pan from Purdue University and Profs. Peixue Jiang and Ruina Xu from Tsinghua University, for the training I obtained from working with them while I was an undergraduate student which helped me step into heat transfer research, and for the help I received from them when I was applying for graduate school.

Moreover, my gratitude also goes to the many collaborators of various interesting

projects I have worked on, without whom a lot of my research would not be possible. I would like to thank Young Jin Kim for the initial training he gave me which helped me get familiar to the lab quickly in my first year. I thank Prof. Sungho Jin and his team in NanoSD, Prof. Zhaowei Liu and Li Chen from Dept. of ECE, and Prof. Yu Qiao, Rui Kou and Ying Zhong from Dept. of Structural Engineering, for our collaboration on the SHIELD projects, which broadened my knowledge in materials sciences and optics. Moreover, I want to thank Jian Zeng, who joined Renkun's group two years after me, for our collaboration on multiple projects. He led the efforts in all these projects and showed incredible productivity and devotion to work, and he taught me how to plan experiments and write papers more efficiently. Besides, I want to thank Yang Shi for her help on the thin film boiling project. When I was stuck in China due to visa problem in summer 2018, she helped me continue the experiments so that we could wrap up the data and eventually publish the paper. Furthermore, I would like to thank Prof. Jian Luo and his team from Dept. of NanoEngineering for the enlightening collaboration on the high-entropy oxide project. In particular, Andrew Wright has demonstrated strong work ethics as a scholar, and I feel extremely fortunate to be able to work with him.

Additionally, I would like to express my sincere appreciation to all my fellow lab mates who have made my experience at UCSD fruitful. When I just started my PhD program, Matthew Wingert and Edward Dechaumphai always showed great patience when I asked stupid rookie questions, and their solid knowledge and nice personalities set very good examples for me to learn from. Jianlin Zheng and Shuang Cui were the only two Chinese students when I first joined the group, who helped me both in the lab and in my personal life. The restaurants we explored together, the sightseeing locations we went to

together, and the movies we saw together, all proved our friendship and made me feel enriched. Soonshin Kwon, Jeongmin Kim, and Sahngki Hong were senior to me, and they have not only helped me in many experimental details, but also showed me how to be responsible as a man and carry weight for his family. Sunmi Shin and Lizzie Rubin were my officemates for three years, and we chatted almost every day. Sunmi's tireless attitude always inspired me to work harder and tackle the problems when I faced setbacks, and Lizzie helped me get to know American culture better, for which I'm very thankful as an international student. Yuchao Hua from Tsinghua University and Prof. Lin Chen from NCEPU both visited our group and shared with me abundant stories and opinions, which helped me learn about the research community and faculty job in China. Moreover, the new generation of group members, Jian Zeng, Yang Shi, Ka Man Chung, Tianshi Feng, and Yu Pei, all helped me on various technical and nontechnical matters. We shared Chinese snacks in the office and made dumplings in Jian's apartment on the Spring Festival, and these are the essential moments that made me feel home in a different country. I also want to thank all the master's and undergraduate students and visiting scholars who have been part of the group and fulfilled my life at UCSD. Finally, I would like to acknowledge the group beer sessions (especially those paid by Renkun), which were supposed to be pressure-relieving, and it worked almost every time. It is very unfortunate that we cannot go to beer sessions regularly due to the COVID-19 lockdown, since the information one can grab from beer session is incredibly rich, including gossips of lab members and career advices from Renkun.

On a personal note, there are also many great people I must thank. Being a PhD student constantly under pressure, my life at San Diego would never be so joyful without

the presence of many friends. In particular, I must acknowledge Qiguang He, who has been my roommate for the entire past five years. He helped me in all aspects of my life, and he deserves my hearty appreciation which can never be described in one short paragraph. Thanks to Qiguang, I also became very good friends with many of his lab mates in Prof. Shengqiang Cai's group. We had dinner almost every Friday to talk about everything that were happening during the week. At various all-you-can-eat places, we celebrated birthdays and publications, and we patted each other on the back for failures and disappointments. It is the presence of these friends and the time we had together that saved me from the frustration when my experiments failed. Specifically, I want to thank Zhijian Wang, Xudong Liang, and Yang Wang from Cai group. With Qiguang together, five of us had beer multiple times to relieve both the stress from work and the anxiety for the uncertainties of future, which had proven to be very helpful. I also want to thank Yue Zheng for the conversations between us about lots of useful information and interesting stories, and for the discussions we've had about the plan of our academic careers, both of which have expanded my view and helped me make better decisions. Moreover, I would like to thank Bei Fan, Peng Chen, Yun Zhou, and my lab mates Shuang Cui and Yang Shi, for their support and company to my girlfriend when she moved to San Diego and needed new friends. I also owe my gratitude to many other friends I met here although I cannot list all of them. I would like to take this opportunity to thank everyone who have helped me in any aspect. I am sincerely grateful.

At last, I'm greatly indebted to my family for their unwavering love. This dissertation is dedicated to them. My parents raised me with patience and always gave me the best they can, my grandparents showed caring for me wherever I was, my sisters took

good care of my parents when I was thousands of miles away from home, and my lovely nieces and nephews were constantly asking me when I'll be back home during video chats, yet I rarely spoke out my love for them, even though I missed them almost every day. I'm terrible at expressing feelings to family, and in a lot of cases, I didn't even know what to talk with them when we were on video chats. Nevertheless, I know for sure that it is their unconditional love and endless support over the years that encouraged me to pursue my dream abroad, and there is no doubt that I am here because of them. I know they are proud of me, and I hope I can spend more time with them in the future. Lastly but most importantly, I would like to express my sincerest appreciation to my girlfriend, Xuan Feng, for the love she has been giving me for the past seven years. She has been incredibly supportive for everything I did, and her accompany with me here at San Diego is the reason that I could be less homesick and that my parents could be less worried about me. She is the constant source of joy and happiness for me, and I can never become who I am without her. I owe her everything.

Chapter 1, in part, is a reprint of the material as it appears in "Transition between thin film boiling and evaporation on nanoporous membranes near the kinetic limit", *International Journal of Heat and Mass Transfer* 154 (2020): 119673, by Qingyang Wang, Yang Shi, and Renkun Chen. The dissertation author was the first author of this paper.

Chapter 1, in part, is a reprint of the material as it appears in "Advanced Materials for High-Temperature Thermal Transport", *Advanced Functional Materials* 30.8 (2020): 1904815, by Sunmi Shin*, Qingyang Wang*, Jian Luo, and Renkun Chen. The dissertation author was the co-first author of this paper.

Chapter 2, in full, is a reprint of the material as it appears in "Ultrahigh flux thin film boiling heat transfer through nanoporous membranes", *Nano Letters* 18.5 (2018): 3096-3103, by Qingyang Wang and Renkun Chen. The dissertation author was the first author of this paper.

Chapter 3, in part, is a reprint of the material as it appears in "Widely tunable thin film boiling heat transfer through nanoporous membranes", *Nano Energy* 54 (2018): 297-303, by Qingyang Wang and Renkun Chen. The dissertation author was the first author of this paper.

Chapter 3, in part, is a reprint of the material as it appears in "Transition between thin film boiling and evaporation on nanoporous membranes near the kinetic limit", *International Journal of Heat and Mass Transfer* 154 (2020): 119673, by Qingyang Wang, Yang Shi, and Renkun Chen. The dissertation author was the first author of this paper.

Chapter 4, in part is currently being prepared for submission for publication of the material, by Qingyang Wang, Andrew J. Wright, Jian Luo, and Renkun Chen. The dissertation author was the first author of this material.

Vita

2015 Bachelor of Engineering, Tsinghua University

2016 Master of Science, University of California San Diego

2020 Doctor of Philosophy, University of California San Diego

Publications

1. **Q. Wang**, R. Chen, "Ultrahigh flux thin film boiling heat transfer through nanoporous membranes", *Nano Letters* 18.5 (2018): 3096-3103.

2. **Q. Wang**, R. Chen, "Widely tunable thin film boiling heat transfer through nanoporous membranes", *Nano Energy* 54 (2018): 297-303.

3. J. Zeng, S. Cui, **Q. Wang**, R. Chen, "Multi-layer temperature-responsive hydrogel for forward-osmosis desalination with high permeable flux and fast water release", *Desalination* 459 (2019): 105-113.

4. R. Kou*, Y. Zhong*, J. Kim, **Q. Wang**, M. Wang, R. Chen, Y. Qiao, "Elevating low-emissivity film for lower thermal transmittance", *Energy and Buildings* 193 (2019): 69-77.
   *These authors contributed equally to this work.

5. J. Zeng, **Q. Wang**, Y. Shi, P. Liu, R. Chen, "Osmotic pumping and salt rejection by polyelectrolyte hydrogel for continuous solar desalination", *Advanced Energy Materials* (2019): 1900552.

6. S. Shin*, **Q. Wang***, J. Luo, R. Chen, "Advanced materials for high-temperature thermal transport", *Advanced Functional Materials* (2019): 1904815.
   *These authors contributed equally to this work.

7. A. J. Wright, **Q. Wang**, C. Huang, R. Chen, J. Luo, "From high-entropy ceramics to compositionally-complex ceramics: a case study of fluorite oxides", *Journal of the European Ceramic Society* 40.5 (2020): 2120-2129.

8. A. J. Wright, **Q. Wang**, S. T. Ko, K. M. Chung, R. Chen, J. Luo, "Size disorder as a descriptor for predicting reduced thermal conductivity in multicomponent and high-entropy pyrochlores", *Scripta Materialia* 181 (2020): 76-81.

9. **Q. Wang**, Y. Shi, R. Chen, "Transition between thin film boiling and evaporation on nanoporous membranes near the kinetic limit", *International Journal of Heat and Mass Transfer* 154 (2020): 119673.

10. R. Kou, Y. Zhong, **Q. Wang**, J. Kim, R. Chen, Y. Qiao, "Thermal insulating polymer-air multilayer for window energy efficiency", *submitted*.

Abstract of the Dissertation

Microscale Engineering of Phase Change and Radiation Heat Transfer

by

Qingyang Wang

Doctor of Philosophy in Engineering Sciences (Mechanical Engineering)

University of California San Diego, 2020

Professor Renkun Chen, Chair

The rapid growth of modern economy and the increasingly high quality of human life over the last century are essentially attributed to the development of energy technologies, including the conversion, transport, storage, and utilization of energy. The transfer of thermal energy plays an instrumental role in virtually all energy related technologies. As such, exploring the fundamentals of heat transfer is of significant importance for both scientific advancement and technological development. Each of the basic heat transfer modes is governed by different length scales, understanding and engineering of which thus underpin the development of heat transfer technologies. In this dissertation, quantification and engineering of characteristic lengths in two different heat

transfer mechanisms, namely, phase change heat transfer (PCHT) and radiation heat transfer, are studied.

Liquid-vapor PCHT utilizes latent heat of vaporization to efficiently transport a large amount of thermal energy, which is being used in a variety of thermal energy conversion and management applications. The critical heat flux (CHF) of PCHT, either evaporation or boiling, is fundamentally limited by mass flux of the vapor departing from the liquid-vapor interface, known as the kinetic limit. This limit could be in theory greater than 1 kW cm^{-2} on a planar surface, but its experimental realization has remained elusive. In the first part of this dissertation, by leveraging the small length scale for heat conduction and vapor bubble departure within a thin liquid film, a new "thin film boiling" mechanism is proposed and realized by confining the boiling liquid within a microscale film on a nanoporous membrane. Superior heat transfer performance is demonstrated with a high CHF of over 1.8 kW cm^{-2}, which is among the highest reported values for PCHT on a planar surface and is within a factor of four of the calculated theoretical kinetic limit. Furthermore, by continuously shrinking the liquid film, a universal transition from boiling to evaporation is further identified for different fluids with varying surface tension values (water, ethanol, isopropanol, and perfluorohexane), and the heat transfer characteristics of the transition points are found to be close to the kinetic limit. The limiting factors dictating the transition between the two different heat transfer modes are also elucidated.

In advanced materials for high temperature thermal transport such as thermal barrier coatings for turbine blades and heat transfer media in concentrated solar power plants, the radiative thermal transport, which is often negligible at room temperature, becomes comparable to or even more important than heat conduction. However, an

effective thermal conductivity encompassing both heat transfer modes is often used at high temperatures, due to the lack of a convenient methodology to separate the contributions from conduction and radiation, especially for high temperature thermal measurement using the prevailing instrument called the laser flash analyzer (LFA). In particular, the characteristic length scale of radiation heat transfer is often elusive. In the second part of this dissertation, a transient coupled conduction/radiation model, with the realistic boundary conditions used in the LFA, is developed to study the transient heat transfer in high temperature materials. By identifying the propagation length of photons in different portions of the spectrum, heat transfer due to photons with direct transmission and diffusive transport is delineated. In the conductive thermal conductivity of semi-transparent materials obtained from the LFA, conventional models would still cause non-negligible error at high temperatures, while the coupled model developed here can accurately quantify the radiative contribution.

Chapter 1 Introduction

1.1 Background

The rapid growth of modern economy and the increasingly high quality of human life over the last century are essentially attributed to the development of energy technologies, including the conversion, transport, storage, and utilization of energy. The transfer of thermal energy plays an instrumental role in virtually all energy related technologies. For example, the majority of the electricity used worldwide is generated by heat engines in various power plants, where the thermal energy is produced from combustion of fossil fuels or nuclear reaction and then transferred to high temperature steam by boiling heat transfer happening in the boiler. In renewable energy systems such as concentrated solar power (CSP) plants, the conversion from light to heat, the transfer of heat using molten salt, supercritical CO_2 or particles, and the storage of heat for grid resiliency are all of significant importance to the efficient operation of the system. As such, exploring the fundamentals of heat transfer is vitally important for both scientific advancement and technological development.

In different heat transfer modes, the thermal transport behaviors are governed by different length scales. Understanding the fundamentals of a heat transfer problem requires the identification of the length scale pertinent to the problem, and the development of new technologies requires the engineering of the length scales for desirable heat transfer.

There have been extensive efforts made in the past several decades on understanding and engineering of the characteristic length scale in conduction heat transfer [1, 2]. At microscale, in non-metallic crystalline solids, the main heat carriers are the lattice

vibrational modes described as phonons, and the thermal conductivity k for a wide range of materials can be understood from the kinetic theory as $k = \frac{1}{3} C v \Lambda$ where C is the specific heat, v is the group velocity, and Λ is the mean free path of the phonons. The kinetic theory indicates that the mean free path Λ, representing the average distance a phonon travels between two successive scattering events, essentially determines the characteristics of heat conduction in solids. This characteristic length is fundamentally governed by multiple phonon scattering processes, including impurity scattering, boundary scattering, and *Umklapp* scattering [3-6] . Engineering the mean free path of phonons is vital to achieve desirable heat conduction properties. For example, complex crystal structure, high impurity density, and nanostructuring have been sought to enhance phonon scattering and obtain low thermal conductivity for thermal insulation and thermoelectric applications [7-9]. Meanwhile, defect free, low atomic mass simple crystals with large acoustic-optical phonon frequency gap have been explored to suppress the phonon scattering and obtain high thermal conductivity efficient heat dissipation [10, 11].

Compared with conduction, the length scales in other heat transfer modes are less explored. For example, in liquid-vapor phase change heat transfer (PCHT), the mean free path of the energy carrier, namely, molecules, does not determine the heat transfer performance of either boiling or thin film evaporation, unless the phenomena occur in the free molecule regime (e.g., at low pressure). Although it is widely acknowledged that the use of micro/nanoporous structures can reduce the conductive thermal resistance in the liquid for thin film evaporation [12], engineering the length scale to tailor the boiling heat transfer performance is not well understood. Moreover, at high temperatures, conduction and radiation are usually coupled. Although it is recognized that radiation heat transfer

contributes significantly to the total heat transfer at high temperatures even inside solid materials [13, 14], the photon thermal conductivity, which possesses different propagation lengths compared to phonon thermal conductivity, is usually not quantified, often rendering errors in thermal property measurements at high temperatures. In this dissertation, PCHT and high temperature coupled conduction-radiation heat transfer are studied, and their respective characteristic length scale are explored.

1.2 Overview of boiling and evaporation

The utilization of the latent heat of vaporization in liquid-vapor phase change heat transfer (PCHT) allows the transport of a large amount of thermal energy efficiently. As such, liquid-vapor PCHT has been used extensively for a variety of applications, such as power generation, refrigeration, water desalination and purification, and thermal management of electronics and electric vehicles [15-23]. In particular, the thermal management of electronic devices has become a key bottleneck for their future development toward greater compactness and higher performance [24], since the efficient removal of heat is of critical importance for the device performance and durability. Many of them require high heat flux dissipation (>100 W cm^{-2}) with low superheat, which becomes even more demanding for devices with high power density, such as light emitting diode, power electronics, high performance CPUs and GPUs, and laser devices [25]. For example, the CPU power density has been increasing exponentially for over one decade until early this century when the multicore processors were introduced and deployed and the power density plateaued at ~100 W cm^{-2} [26]. Moreover, for GaN-based high electron mobility transistors, heat flux over 1 kW cm^{-2} is expected with local hotspot exceeding 5

kW cm^{-2} [27]. In comparison, the radiative heat flux emitted from the surface of the sun is ~6 kW cm^{-2}. Such extreme heat fluxes create an unpresented challenge for thermal management solutions and cooling technologies.

Traditional single phase convective cooling has low heat flux and heat transfer coefficient and thus cannot meet the cooling demand unless microchannels are used which requires significant pumping power for high mass flux [28]. Due to its ability to achieve high heat flux with small temperature difference, liquid-vapor PCHT is considered to be one of the most promising solutions for the thermal management challenge of next generation high power electronic devices. Numerous studies have been carried out in various PCHT schemes, including two distinct modes, boiling and evaporation, to achieve high heat flux and low superheat for high heat transfer capability and efficiency. The theoretical maximum heat flux of PCHT for either evaporation or boiling is essentially the interfacial kinetic limit, which is fundamentally associated with the vapor flux leaving the interface and predicts orders of magnitude higher heat flux than typical PCHT experimental results.

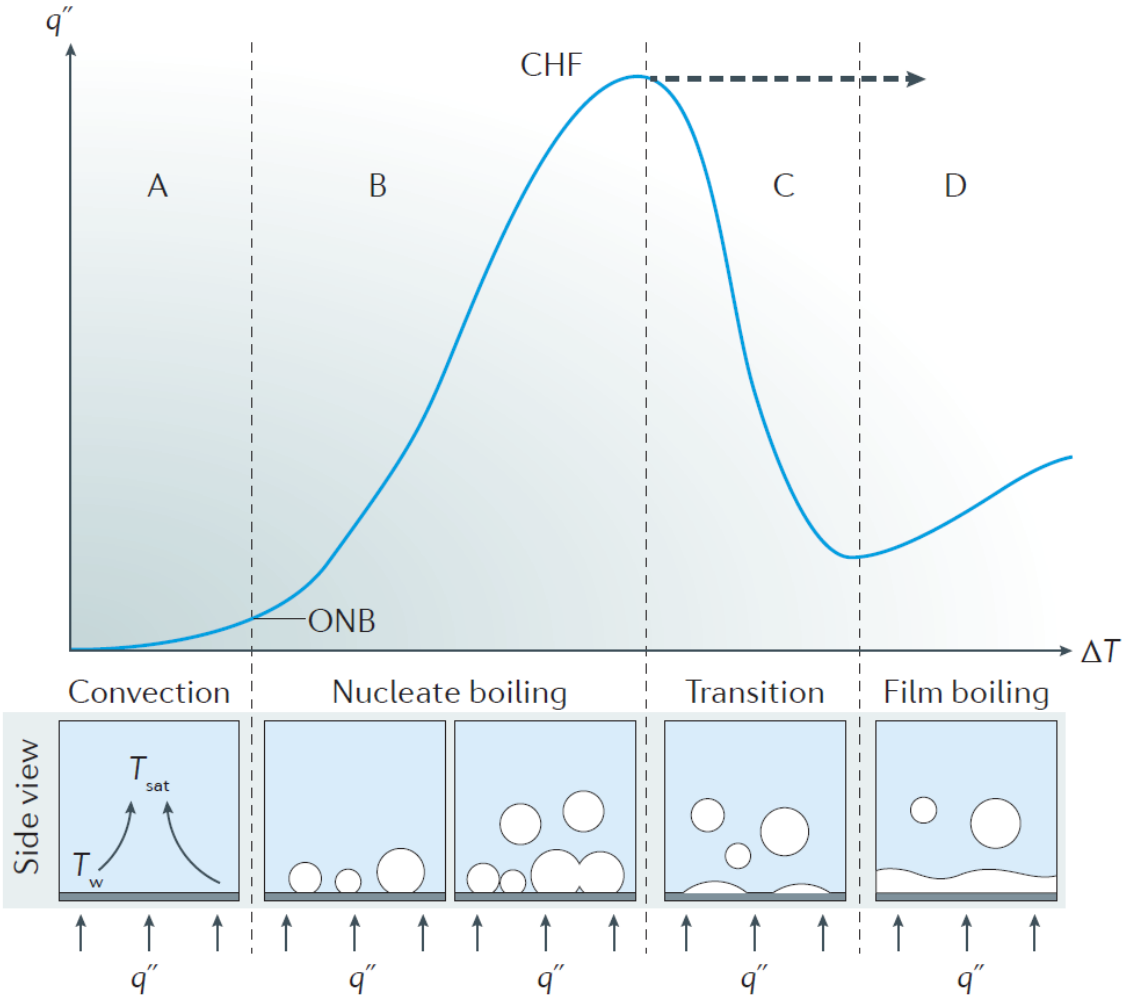

Figure 1.1: A typical boiling curve qualitatively showing heat flux versus wall superheat, and schematics showing the heat transfer modes at different regimes. Reproduced with permission from Ref. [29]. Copyright 2016, Springer Nature.

There are mainly two types of boiling studied in the literature: pool boiling and flow boiling. In pool boiling, a stagnant bulk pool of liquid is heated up and bubbles are generated on the heater surfaces. The heat transfer characteristics is usually represented by the boiling curve which shows the heat flux versus the superheat (the temperature difference between the wall and the liquid saturation temperature), as shown in Figure 1.1 (reproduced with permission from Ref. [29]). With increasing heat flux, the heat transfer

mode changes from natural convection to nucleate boiling, and finally transitions to film boiling when the bubbles coalesce and form a continuous vapor blanket that blocks further heat transfer, and the corresponding heat flux is the so-called critical heat flux (CHF). In pool boiling, the bubble behaviors dictate the heat transfer performance, and the CHF represents the maximum heat flux that can be dissipated under safe operation conditions, which is usually on the order of 100 W cm^{-2} for a flat surface for water at the atmospheric pressure. Extensive efforts have been made to enhance the CHF and decrease the wall superheat using various strategies, including managing the bubble nucleation sites [30-32], increasing the surface wettability/capillarity using micro/nanostructures, which usually also increases the nucleation site density and provides a fin effect with an enhanced heat transfer area [22, 33], increasing the contact line length [34, 35], providing separate liquid-vapor pathways for enhanced macroconvection [36, 37], preventing bubble coalescence by pinning the contact line [38], and combination of multiple mechanisms stated above. Figure 1.2 shows the literature reported CHF for pool boiling of water at atmospheric pressure using various structures [22, 37, 39-46]. Significant CHF enhancement has been demonstrated up to ~400 W cm^{-2} [47], but the CHF is still relatively low compared with flow boiling and other new configurations using water [48, 49]. Moreover, the CHF of pool boiling for nonaqueous fluids is usually significantly lower than that of water due to the difference in the thermophysical properties, such as the latent heat of vaporization. For example, CHF values were less than 30 W cm^{-2} for FC-72 [50] or HFE-7100 [51], as the latent heat of these fluids is more than one order of magnitude lower than that of water. In addition, for organic solvents and dielectric fluids that are desirable for cooling of

electronic devices, common approaches to manipulate the contact angels for water would not work.

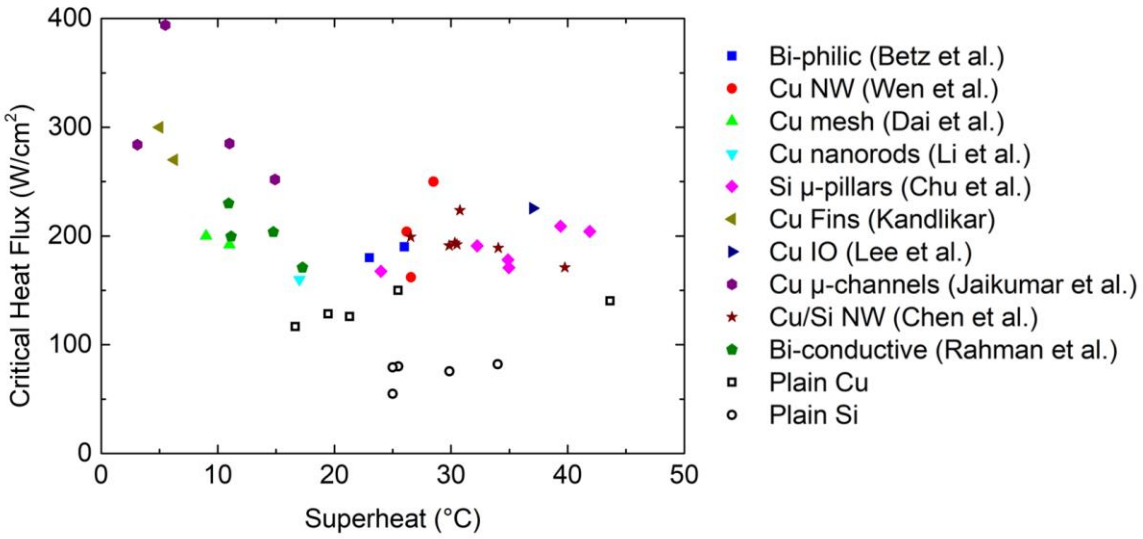

Figure 1.2: CHF for pool boiling of water at atmospheric pressure using various structures reported in Betz et al. [39], Wen et al. [37], Dai et al. [40], Li et al. [41], Chu et al. [42], Kandlikar [43], Lee et al. [44], Jaikumar et al. [45], Chen et al. [22], and Rahman et al. [46].

Flow boiling can significant increase the CHF and heat transfer coefficient (HTC) by forcing the liquid to flow along the heated surfaces, and have thus been intensively studied in the past and widely applied for cooling in various systems such as cooling of nuclear reactors, which demands superior stability and reliability for safety. The use of microchannels with various micro- and/or nanostructures [52-54] can significantly reduce the conductive resistance for heat transfer in liquid, promote bubble nucleation, and delay the occurrence of film boiling by enhancing liquid rewetting. However, the large volume expansion of phase change could lead to flow instability inside the microchannels and a pre-mature CHF if not properly designed [55]. For dielectric fluids, it is even more

challenging to enhance the CHF due to their poor thermophysical properties [56]. High mass flow rate, subcooled liquid, and delicate structural design have been investigated to achieve higher CHF [57, 58].

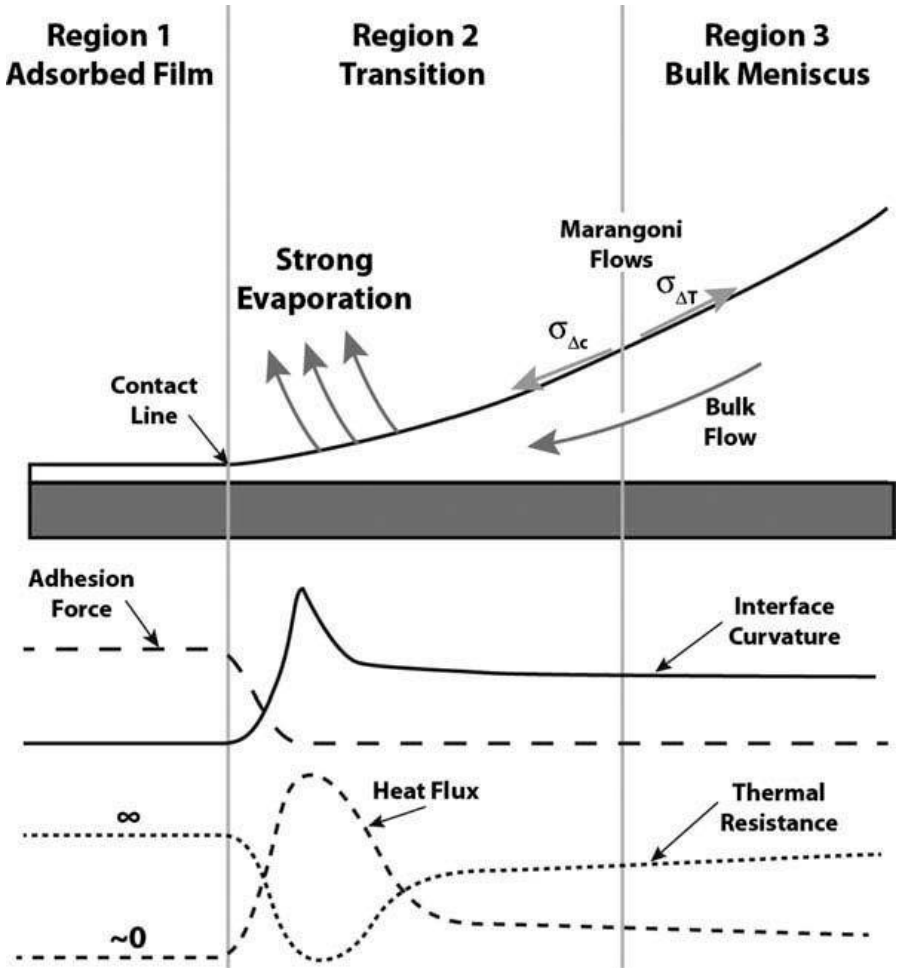

Figure 1.3: Variation in adhesion force, curvature, heat flux, and thermal resistance in the contact line region for an evaporating meniscus. Reproduced with permission from Ref. [12]. Copyright 2014, Taylor & Francis Group, LLC.

As another main mode of PCHT, evaporation from a thin liquid film has been used in heat pipes and vapor chambers. When using thin film evaporation to dissipate heat, the evaporating meniscus can be divided into three regions, namely, the absorbed film region,

the transition region, and the bulk meniscus region, as shown in Figure 1.3 (reproduced with permission from Ref. [12]). In the absorbed film region, there are a few layers of liquid molecules absorbed on the solid surface, and the strong attractive forces between the liquid and the solid prevent these molecules from evaporating. In the bulk meniscus region, the thick liquid layer introduces a large conduction resistance due to the intrinsic low thermal conductivity of the liquid, which renders the evaporation at the liquid-vapor interface inefficient. The majority of heat transfer takes place in the transition region of the liquid-vapor interface near the triple-phase contact line [12], where the small thickness of the liquid layer minimizes the conduction resistance inside the liquid while the thickness is also not too small to result in excessively large adhesion between the solid surface and fluid molecules. However, this transition region only constitutes a small portion of the entire interface, and therefore the heat flux of evaporation is low, which limits its application in high heat flux cooling. Micro/nanostructures can provide efficient heat conduction pathways, thereby increase the effective thin film area and decrease the characteristic length for heat transfer in liquid. Besides, they can also provide large capillary force to continuously pump liquid to the interface for vaporization. Thus, they are extensively applied in evaporation studies to minimize the thermal resistance of the system and enhance liquid supply [59-62]. However, these micro/nanostructures, usually with a porous geometry, induce large viscous resistance for fluid transport to the interface, which is dictated by the pore size and coupled with the pumping capillary force. Recently, nanoporous membrane configuration is proposed for achieving high heat flux evaporation by partially decoupling the viscous drag and the capillary driving force [63]. By supplying liquid from the cross-plane direction of the membrane and reducing the membrane

thickness, the liquid transport flow length is decreased to lower the viscous drag without significantly affecting the heat transfer and capillary force. Enhanced heat transfer performances have been predicted [64, 65] and demonstrated [66-68]. However, the achieved heat flux is still far lower than 1 kW cm^{-2}.

To summarize this section, despite intensive efforts from researchers during the past several decades, the experimentally realized heat transfer performance for PCHT, including both boiling and evaporation, is still far below the high demand for future application on high power electronics. Specifically, CHF values of most studies are still far below 1 kW cm^{-2} except for several reported works with delicate, mostly three dimensional (3D), structures which require complicated fabrication processes [49, 58, 69]. Besides, the high CHFs achieved usually benefit from extended area of 3D microstructures, indicating that the heat flux for a flat surface could be far lower than the reported value, and/or the heat transfer behavior may deteriorate if the system is scaled up. Moreover, the ultimate limit of the PCHT heat flux has not been approached, leaving behind a large gap between the theoretical limit and the experimental values. Furthermore, the boiling and evaporation from micro/nano- structures are usually considered to be two different modes of heat transfer, and the interaction and transition between them are rarely discussed. Therefore, in this dissertation, we aim to experimentally achieve high CHF for PCHT on a flat surface with scalable feature, as well as to fundamentally understand the limits of PCHT and the underlying mechanisms of boiling/evaporation transition.

1.3 High temperature thermal transport and thermal barrier coatings

Many industrial processes vital for energy and materials productions are currently operating or being pushed to operate at high temperature, namely, above 700 °C. The quest for high operation temperatures is primarily driven by two benefits: increasing the exergy or the thermal-to-electrical energy conversion efficiency and enhancing the kinetics of reactions or transport processes. For instance, there is an international effort to develop advanced ultra-supercritical (A-USC) power plants that can operate with steam at temperature above 700 °C and pressure at 35 MPa, up from today's temperature range of around 600 °C [70]. This increase in temperature and pressure is expected to boost the efficiency of coal-fired power plants from ~37% to ~45% [70, 71]. In the concentrating solar power (CSP) plants, the current roadmap outlined by US Department of Energy, named "Generation-3 CSP", aims to achieve a heat transfer fluid (HTF) temperature above 700 °C, up from today's temperature of approximately 600 °C. This increase in operation temperature will improve the solar-to-electricity conversion efficiency and consequently reduce the levelized cost of electricity (LCOE) to below $0.05 per kWh [72]. Gas turbine engines, widely used for aerospace propulsion and electricity generation from natural gas or liquid fuels, have been experiencing steadily increase in turbine rotor inlet temperatures above 1300 °C [73]. One of the conceived solar-fuel production methods at scale is based on two-step thermochemical water splitting using metal oxides, such as ceria, pervoskites, and spinel ferrites, which typically requires reduction temperature in excess of 1000 °C [74, 75], as required by both the thermodynamics and kinetics of the redox processes. Solid oxide fuel cells (SOFC) can achieve higher efficiencies than internal combustion engines. Despite tremendous efforts to lower the operation temperature [76], today's best SOFCs

are still operating at high operation temperature (650-850 °C) in order to attain high power density [77], due to the requirements on kinetics of catalytic oxygen reduction reaction (ORR) [78] and ionic conductivity in the electrolytes. Emerging solid-state thermal-electrical energy conversion devices, such as thermoelectric [79], thermophotovoltaic [80, 81], and thermionic [82], have also been considered and demonstrated as potential pathways towards low-cost utilization of ubiquitous thermal energy from the Sun and other heat sources [83]. As the power conversion efficiency of these devices are bounded by the Carnot limit, their efficiencies would generally increase at high temperature. Thermionic converters also need to operate at high emitter temperature (generally above 1000 °C) [84, 85] to yield a higher current density as described by the Richardson-Dushman equation. The radiation spectrum of thermophotovoltaic emitter has to be matched with the bandgap of the photovoltaic cell, which generally requires the emitter temperature to be at least 730 °C (1000 K) [86, 87] for practical power density and conversion efficiency. While thermoelectric devices have been used at room and moderate temperatures for refrigeration and waste heat recovery, there is a continued push for high-efficiency thermoelectric materials at high temperature, such as Si-Ge, half-Heusler, and oxides [88], for applications in space exploration [88], high-temperature waste heat harvesting (e.g., from industrial furnaces) [88], and combustion- or solar-driven generators [86].

Thermal transport plays a key role in all these high temperature processes, for example, in the design and implementation of high temperature thermal insulation materials, such as thermal barrier coatings (TBCs) for turbine blades, as shown in Figure 1.4 (reproduced with permission from Ref. [89]). In high temperature gas turbine engines, the TBCs insulate the turbine blades from the hot gas, thereby reduce the surface

temperature of the blades in the engine and enable an engine operation temperature much higher than the material allowable temperature of the blades made of superalloys. As shown in Figure 1.4, the TBC system contains the oxide ceramic coating (also called topcoat) which provides thermal insulation, the bond-coat layer which provides oxidization resistance, and the thermally grown oxide (TGO) layer which forms during operation due to the oxidation of bond-coat.

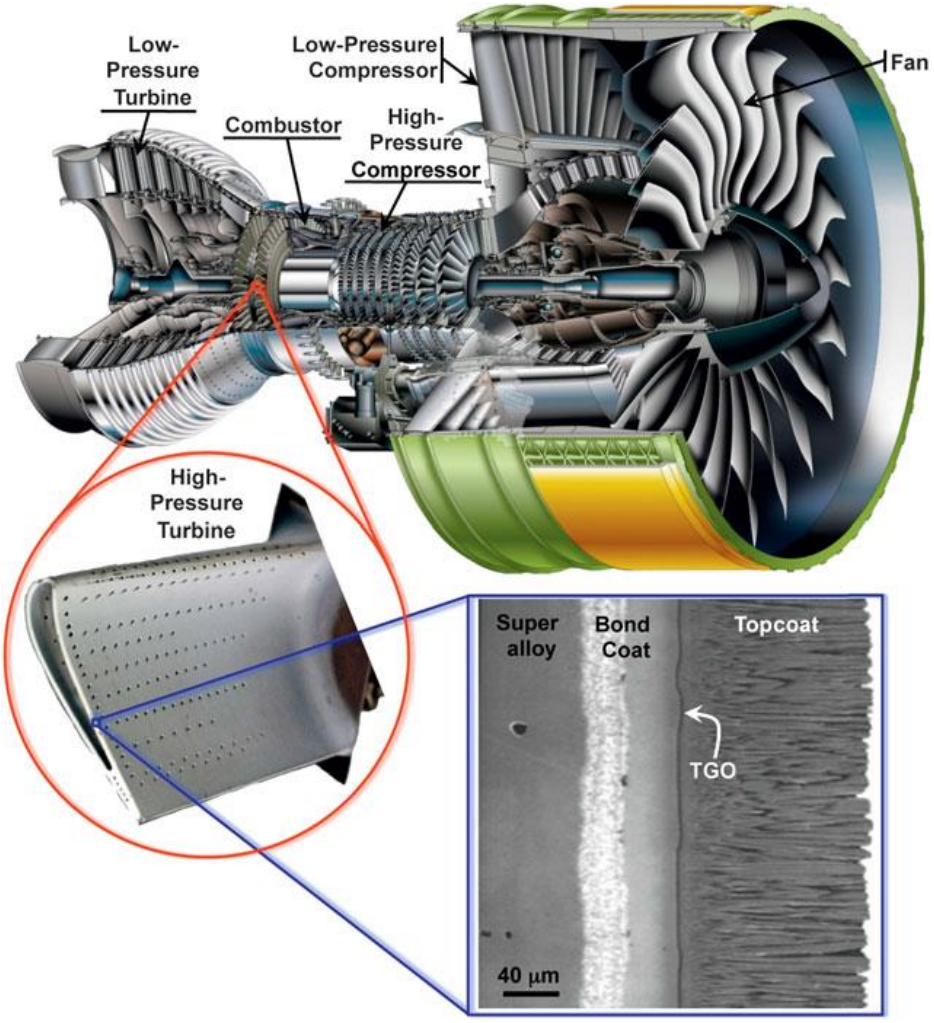

Figure 1.4: Cutaway view of an engine, photograph of a turbine blade with thermal barrier coating (TBC), and a scanning electron microscope (SEM) image of a cross-section of an electron beam physical vapor deposited 7 wt% yttria-stabilized zirconia TBC. Reproduced with permission from Ref. [89]. Copyright 2012, Materials Research Society.

Due to the extreme temperature and pressure conditions for TBCs to operate at, the TBC materials need to meet various stringent requirements [89]. For thermal protection of the superalloy parts, the TBC materials needs to be thermally insulative, indicated by a low thermal conductivity at high temperatures, and optically reflective or opaque in the wavelength range of the radiant heat from the hot gas. Meanwhile, the TBC materials should also have certain strain compliance to accommodate the mismatch between the thermal expansion coefficients of the coating material and the superalloy. Moreover, they should be chemically and mechanically stable at high temperatures, be able to withstand extreme thermal shock, and have long term cyclability between room and high temperatures.

Among all the different requirements that TBCs need to satisfy, low thermal conductivity at high temperatures is the primary performance metric [90]. There are several unique features pertaining to thermal transport in materials at high temperature. In the high temperature range considered here, the temperature is generally higher than the Debye temperature of most solids, thus leading to constant specific heat at the Dulong-Petit limit. For instance, the Debye temperature of zirconia with various stabilizers ranges from 575 to 625 K [91]. Perhaps the more prominent feature at high temperature is the dominant role of the *Umklapp* scattering due to the lattice anharmonicity. For instance, most oxides have thermal conductivity approaching the minimum value commonly seen in amorphous material at high temperature due to the strong *Umklapp* scattering [92]. Moreover, radiation heat transfer, which is usually negligible at room temperature, becomes an appreciable and even dominant thermal pathway at high temperature, as the radiative thermal conductance

scales as T^3. For example, from modeling of the temperature distribution of a typical TBC configuration where the TBC material is bonded with a metal layer and the TBC and metal are subjecting to hot gas and air convection on respective boundaries, it is found that compared with the opaque TBC condition where there is only conduction happening inside the TBC, if there is also radiation inside the TBC, the temperature of the metal can be significantly higher, and the heat flux transferred across the TBC is significantly larger, indicating a worse insulation performance of the TBC due to the significant radiation contribution [13].

The state-of-the-art TBC material is yttria-stabilized zirconia (YSZ), among which the 7~8 mol% YSZ (called 7YSZ or 8YSZ) is most widely used, with thermal conductivity of 2~3 W m^{-1} K^{-1} from room temperature to over 1000 °C in a dense form. Pure ZrO_2 transforms from the tetragonal to the monoclinic phase at about 1173 °C, and it is stable in preferred cubic fluorite phase only at about 2370 °C. Incorporating the stabilizer Y_2O_3 into ZrO_2 helps to stabilize the preferred high-symmetry cubic and tetragonal phases within the operation temperature window (e.g., 1000 to 1200 °C). Meanwhile, due to the difference in the charge valences between the Y^{3+} and Zr^{4+} cations, each Y^{3+} introduces an oxygen vacancy, thus providing an additional phonon scattering mechanism with the point defects to further lower the thermal conductivity. As shown in Figure 1.5, at 1000 °C, thermal conductivity of 8YSZ is about 2.36 W m^{-1} K^{-1}. In general, increasing the Y^{3+} concentration can provide more oxygen vacancies and lower the thermal conductivity. However, the oxygen vacancies could aggregate and form clusters instead of randomly distribute in the lattice when the concentration of oxygen vacancies is too high, which stops the trend of decreasing thermal conductivity and leads to an optimal concentration [93, 94].

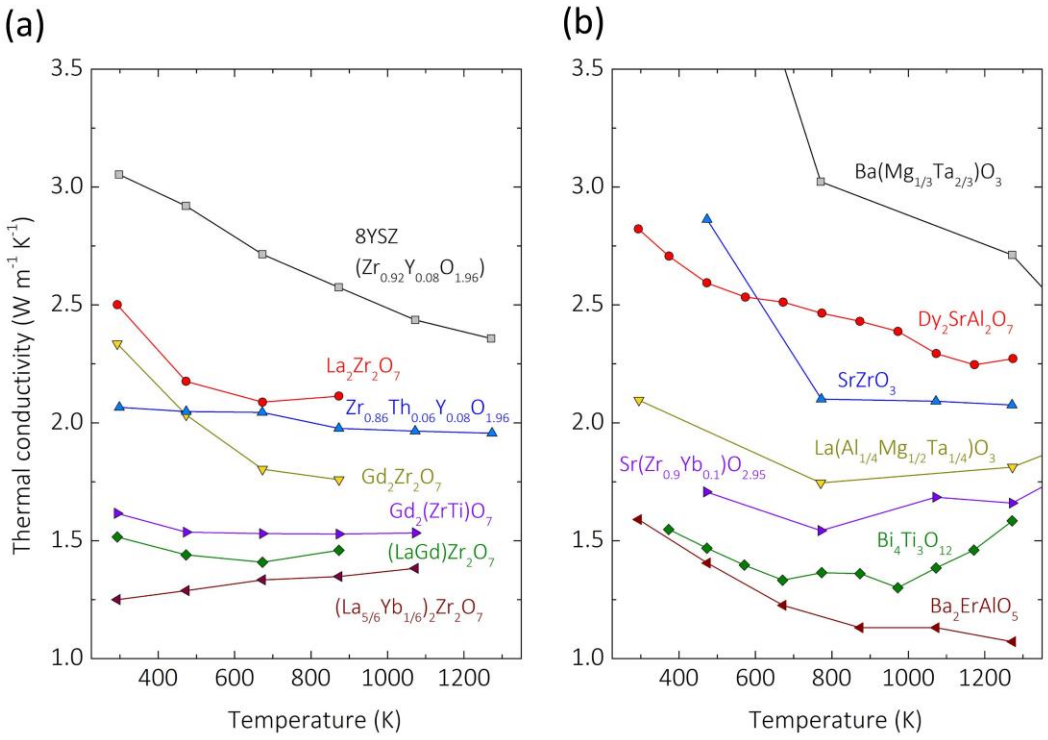

Figure 1.5: Thermal conductivity as a function of temperature for (a) fluorite or pyrochlore based structures and (b) perovskite-based structures.

Further reducing the thermal conductivity is desirable to ensure better insulation performance. There have been significant efforts in searching for other promising TBC materials. Substituting the cations in YSZ is one effective method to reduce the thermal conductivity. Replacing the stabilizer cation Y^{3+} with Gd^{3+}, Yb^{3+} or Nd^{3+} results in a lower thermal conductivity due to the increased scattering of phonons by the larger mass and size difference compared with the host cation Zr^{4+} [95-97]. Substituting a small fraction of the Zr^{4+} with other tetravalent cations [98-100], or doping the zirconia with multiple oxides with different valence [101, 102], both showed reduction of thermal conductivity due to

the added phonon scattering. Along the same line, an emerging new opportunity is to utilize the so called high-entropy fluorite (or other structures of) oxides [103] with multiple (typically five) cations and a "severely distorted lattice" with further increase the complexity and phonon scattering to further reduce the thermal conductivity, which will be discussed in detail subsequently.

It is recognized that increasing the complexity of the crystal structure results in increased optical phonon branches and enhance the phonon scattering and reduce thermal conductivity. Pyrochlore structure ($A_2B_2O_7$, where A is 3^+ cations: La, Sm, Gd, Nd, Yb, etc; and B is 4^+ cations; Zr, Hf, Ti, etc) has been explored due to its promise for low thermal conductivity, as well as relatively high thermal expansion coefficient, and high melting point [104]. The pyrochlore structure can be considered as a derivative from the zirconia fluorite structure. The unit cell of pyrochlore consists of eight fluorite-like sub-cells, each having one Zr atom replaced by the Ln atom and contains one oxygen vacancy site for charge neutrality. The large unit cell and the presence of oxygen vacancies lower the thermal conductivity. Indeed, thermal conductivity lower than that of 8YSZ was found in $Ln_2Zr_2O_7$ pyrochlore structures (Ln= La, Sm, Gd, Nd, Yb, Figure 1.5 (a)) [105]. Further thermal conductivity reduction can be realized by introducing two Ln elements [106-110], or by partially substituting/doping the Zr sublattice on the B site by other tetravalent metals [111], both of which could possibly increase the complexity of the crystal structure and enhance the phonon scattering. Two interesting mechanisms for low thermal conductivity are also introduced, namely the order-disorder transition [109] and the rattling effect [110]. More detailed discussion on the substitution effect on $Ln_2Zr_2O_7$ structure can be found in two comprehensive reviews by Zhao et al. [112] and Liu et al. [113].

It was also predicted by molecular dynamics simulation [114] that the difference in thermal conductivity among $Ln_2B_2O_7$ (where B is the 4^+ cation) with different Ln elements possessing different cation radii is not significant, while the change in the tetravalent element could result in a more clear trend. With increasing cation radius, a consistently decreasing thermal conductivity for B = Ti, Mo, Sn, Zr and Pb is predicted. Several studies [115, 116] validated the constructed contour map, but more experimental work is needed to confirm the results.

Figure 1.5 (a) shows the thermal conductivity as a function of temperature for several TBC materials with the fluorite or pyrochlore structure, including 8YSZ ($Zr_{0.92}Y_{0.08}O_{1.96}$) [100], $Zr_{0.86}Th_{0.06}Y_{0.08}O_{1.96}$ [100], $La_2Zr_2O_7$ [106], $Gd_2Zr_2O_7$ [106], $Gd_2(ZrTi)O_7$ [111], $(LaGd)Zr_2O_7$ [106], and $(La_{5/6}Yb_{1/6})_2Zr_2O_7$ [110]. The pyrochlore $La_2Zr_2O_7$ and $Gd_2Zr_2O_7$ possess lower thermal conductivity than the most common fluorite-structured 8YSZ, which can be attributed to the larger crystal unit cell and increased oxygen vacancies. $Zr_{0.86}Th_{0.06}Y_{0.08}O_{1.96}$ has lower thermal conductivity over the entire temperature range than 8YSZ, which can be attributed to the much larger atomic mass and cation size of Th^{4+} compared with Zr^{4+}, causing greatly enhanced phonon scattering. $Gd_2(ZrTi)O_7$ and $(LaGd)Zr_2O_7$ also show lower thermal conductivity than $Gd_2Zr_2O_7$, which can be similarly attributed to the substituting cation forming point defect and scattering phonons. $(La_{5/6}Yb_{1/6})_2Zr_2O_7$ has much lower thermal conductivity than $La_2Zr_2O_7$, and the reason can be explained by a smaller but heavier Yb^{3+} cation compared with La^{3+} causing a larger vibration amplitude, called the rattling effect [110]. Except for the structures with less point defect, namely 8YSZ, $La_2Zr_2O_7$, and $Gd_2Zr_2O_7$, other materials in the graph all show amorphous-like temperature-independent thermal

conductivity, which is due to the enhanced phonon scattering causing the mean free path of the phonons approaching the inter-atomic distance, a criterion for reaching the minimum thermal conductivity.

The ABO_3 perovskite oxide is another possible candidate for TBC materials. Figure 1.5 (b) shows the temperature dependent thermal conductivity for several typical perovskites, including $SrZrO_3$ [117], $Ba(Mg_{1/3}Ta_{2/3})O_3$ [118], $La(Al_{1/4}Mg_{1/2}Ta_{1/4})O_3$ [119], $Sr(Zr_{0.9}Yb_{0.1})O_{2.95}$ [118], Ba_2ErAlO_5 [120], and another two superlattice structures containing perovskite unit cells, $Dy_2SrAl_2O_7$ [121] and $Bi_4Ti_3O_{12}$ [122]. $SrZrO_3$ shows thermal conductivity of ~2.1 W m^{-1} K^{-1} at high temperatures, lower than 8YSZ in the same temperature range. B-site doping of the ABO_3 with other cations produces complex perovskite structures such as $Ba(Mg_{1/3}Ta_{2/3})O_3$ and $La(Al_{1/4}Mg_{1/2}Ta_{1/4})O_3$, with low thermal conductivity, high thermal expansion coefficient, and/or high melting temperature, which are merits of TBC materials. Substituting the B site cation with lower valence metal can also produce oxygen vacancies to scatter phonons, hence reducing the thermal conductivity, as demonstrated by $Sr(Zr_{0.9}Yb_{0.1})O_{2.95}$ and Ba_2ErAlO_5. Furthermore, superlattice structures containing perovskite/pseudoperovskite cells, such as the Ruddlesden–Popper structure with alternating perovskite and rocksalt layers ($Dy_2SrAl_2O_7$), and the Aurivillius structure with alternating pseudoperovskite and fluorite layers ($Bi_4Ti_3O_{12}$), possess large crystal unit cell with a large number of atoms in each unit cell, consistent with the phenomenological rules to select low thermal conductivity materials, and therefore exhibit lower thermal conductivity compared with the state-of-art TBC materials.

Figure 1.5 (a) also indicates temperature dependence of thermal conductivity does not follow typical phonon behavior, namely, T^{-1} dependence for 3-phonon *Umklapp* scattering or steeper than T^{-1} if four-phonon scattering is important. This calls into the question the validity of the phonon gas picture in these crystalline materials, especially at high temperature. As discussed earlier, as several of these materials possess thermal conductivity approaching the amorphous limit at high temperature, thermal transport mediated by diffuson should also come into the picture [123] . Recent work by Lindsay and coworkers [124] introduced a two-channel model, which includes both the low-frequency propagating phonons and high-frequency diffusons (uncorrelated oscillators) to successfully describe the ultralow thermal conductivity in single-crystalline Ti_3VSe_4. Their work shows that the diffuson, which has effective mean free path below the Ioffe-Regel limit and hence cannot be described by the phonon picture, can contribute to about half of the thermal conductivity in Ti_3VSe_4 at room temperature. A recent work by Ruan and coworkers [125] used the two-channel model to obtain mode-by-mode contribution of phonon and diffuson in $La_2Zr_2O_7$ pyrochlore and also revealed the importance of diffuson. The prominent role of diffuson, which is typically used to describe disordered amorphous materials [126], in crystalline pyrochlore [125], Ti_3VSe_4 [124] and halide perovskite [124], is quite remarkable. This highlights the complex nature of thermal transport in the complex crystals at high temperature and warrants further investigation.

The extensive efforts to identify new TBC materials are under way. Besides the more widely studied fluorite, pyrochlore, and perovskite oxides, other crystal structures are also considered for TBC applications. Rare earth aluminum oxides, metal phosphate, and rare earth silicates have all been demonstrated to have low thermal conductivity [127-131].

However, to implement these materials in TBC applications, other properties should also be taken into consideration, such as the high temperature stability, high thermal expansion coefficient, and high fracture toughness. For example, $Ba(Mg_{1/3}Ta_{2/3})O_3$ coating showed short thermal cycling lifetime due to the low fracture toughness, and $La(Al_{1/4}Mg_{1/2}Ta_{1/4})O_3$ showed secondary oxide phase formation during thermal cycling [119], both of which would limit their implementation in TBC applications.

A new class of materials referred as high-entropy alloys (HEAs), which consists of typically five or more principal elements of roughly equal atomic fractions, attracted extensive interests in the materials community since 2004 [132, 133]. In 2015, a single-phase rocksalt entropy-stabilized oxide (ESO, $(Mg_{0.2}Zn_{0.2}Cu_{0.2}Co_{0.2}Ni_{0.2})O$) was synthesized in the bulk form by Rost et al. [134], followed by the first non-oxide high entropy metal diborides (e.g., $Zr_{0.2}Hf_{0.2}Ti_{0.2}Nb_{0.2}Ta_{0.2})B_2$) reported by Gild et al. in 2016 [135], which extended the high-entropy materials from metals to ceramics. Since then, a variety of high-entropy ceramics have been synthesized, such as high-entropy perovskite [136], spinel [137], and fluorite [103] oxides, carbides [138, 139], and silicides [140, 141]. The rapidly increasing families of high-entropy ceramics provides an excellent platform in search for low thermal conductivity materials for high temperature applications, due to their complex crystal structures which could potentially enhance the phonon scattering or result in a larger fraction of diffuson. For example, Yan et al. [139] synthesized a high-entropy carbide ceramic, $(Hf_{0.2}Zr_{0.2}Ta_{0.2}Nb_{0.2}Ti_{0.2})C$, with a single phase rocksalt structure. They obtained thermal conductivity of 6.45 $W\ m^{-1}\ K^{-1}$ at room temperature, which is much lower than the binary carbides HfC, ZrC, TaC, and TiC and is comparable to NbC. Gild et al. [141] synthesized a high-entropy metal disilicide, $(Mo_{0.2}Nb_{0.2}Ta_{0.2}Ti_{0.2}W_{0.2})Si_2$, with a

measured thermal conductivity of 6.9 W m^{-1} K^{-1}, which is significantly smaller than all five constituent disilicides (with an rule-of-mixture average of ~40 W m^{-1} K^{-1}). Specifically, this thermal conductivity of the high-entropy $(Mo_{0.2}Nb_{0.2}Ta_{0.2}Ti_{0.2}W_{0.2})Si_2$ is approximately one order of magnitude lower than that of the widely-used tetragonal $MoSi_2$ and ~1/3 of those reported values for the hexagonal $NbSi_2$ and $TaSi_2$ with the same crystal structure.

More relevant to TBC applications, Gild et al. [103] first fabricated eleven fluorite oxides with five principal metal cations; eight of them formed single high-entropy phases (e.g., $Ce_{0.2}Zr_{0.2}Hf_{0.2}Y_{0.2}Yb_{0.2})O_2$) with high compositional homogeneity and low thermal conductivity ranging from 1.1~1.8 W m^{-1} K^{-1}. Shortly after Gild et al.'s article [103], Chen et al. [142] also reported the synthesis of another fluorite-structured $(Ce_{0.2}Zr_{0.2}Hf_{0.2}Sn_{0.2}Ti_{0.2})O_2$ (albeit some compositional inhomogeneity as shown in the EDS elemental maps) and obtained a thermal conductivity of 1.28 W m^{-1} K^{-1} at room temperature. Moreover, equiatomic quaternary $(Y_{1/4}Ho_{1/4}Er_{1/4}Yb_{1/4})_2SiO_5$ was synthesized as a new type of TBC/EBC [143]; in comparison with the rule-of-mixture average values of four individual rare earth silicates RE_2SiO_5 (RE = Y, Ho, Er, Yb), $(Y_{1/4}Ho_{1/4}Er_{1/4}Yb_{1/4})_2SiO_5$ exhibits a 19.1% reduction in the thermal conductivity at room temperature, but +7.4% increase in the Young's modulus [143]. Here, simultaneously achieving a reduced thermal conductivity with an increased stuffiness is rather unusual (and potentially beneficial for TBC/EBC applications), as discussed in more detail subsequently. Interestingly, the measured thermal conductivity of $(Y_{1/4}Ho_{1/4}Er_{1/4}Yb_{1/4})_2SiO_5$ initially decreases with the increasing temperature from 200K to ~800K (to a minimum value of < 2W m^{-1} K^{-1}), but it increases with further increasing

temperature from ~800K to 1300K [143]. Moreover, the measured thermal expansion coefficient of $(Y_{1/4}Ho_{1/4}Er_{1/4}Yb_{1/4})_2SiO_5$ is substantially lower than that of any of the individual RE_2SiO_5, but it is closer to that of SiC (being advantageous for potential T/EBC applications) [143]. Most recently, a high-entropy pyrochlore oxide has also been made, where a low room-temperature thermal conductivity of 0.76 W m^{-1} K^{-1} was reported for the as-synthesized $(La_{0.2}Ce_{0.2}Nd_{0.2}Sm_{0.2}Eu_{0.2})_2Zr_2O_7$ [144].

Braun et al. [145] studied their thermal conductivities of a series of high entropy oxides with a single-phase rocksalt structure carefully. Six different type of ESOs were fabricated, including the five-cation $(Mg_{0.2}Ni_{0.2}Cu_{0.2}Co_{0.2}Zn_{0.2})O$, and the six-cation $(Mg_{1/6}Ni_{1/6}Cu_{1/6}Co_{1/6}Zn_{1/6}X_{1/6})O$ where X = Sc, Sb, Sn, Cr or Ge. Regardless of the element added, the six-cation composition shows lower thermal conductivity than the five-cation composition (marked as J14 in the paper). This clearly suggests the trend that heavier mass of the sixth cation results in a lower thermal conductivity. Notably, the thermal conductivity of the six-cation compositions is close to the measured thermal conductivity of the amorphous form of J14 as well as the calculated amorphous limit of J14, which perhaps can also be described by the prominent role of diffusons in the two-channel model [124]. The significant reduction in thermal conductivity is attributed to the enhanced phonon scattering due to disordered interatomic force constants. More uniquely, the low thermal conductivity ESOs maintain the mechanical stiffness represented by the elastic modulus, and remarkably yielded the highest E/κ ratio at room temperature at the time of publication, indicating that the ESOs can help to approach the bottom-right corner for thermally insulative while mechanically stiff materials.

Different from aforementioned studies which focused on increasing the number of components to enhance phonon scattering and reduce thermal conductivity, Yang et al. [146] developed another material family, Ln_3NbO_7 (Ln = Dy, Er, Y, Yb), containing only binary oxide Ln_2O_3 and Nb_2O_5. The fours type of materials all showed low thermal conductivity below 1.5 W m^{-1} K^{-1} at room temperature, and thermally outperforms a variety of TBC materials in the entire temperature range from room temperature to 1000 °C. They also exhibit amorphous-like temperature dependence in thermal conductivity, indicating strong phonon scattering that brings the phonon mean free path to the lower limit. Remarkably, this group of material, in particular Dy_3NbO_7, possesses the record high atio of elastic modulus to thermal conductivity (E/κ) among the literature, exceeding all ESOs reported so far. The exact underlying mechanism of the low thermal conductivity of these materials are yet to be fully understood.

Despite extensive efforts to search for TBC materials with low thermal conductivity, most of the work has been focused on minimizing heat conduction. However, there is a unique feature pertaining to thermal transport in materials at high temperatures: radiation heat transfer, which is usually negligible at room temperature, becomes an appreciable and even dominant thermal pathway at high temperature, as the radiative thermal conductance scales as T^3. This is especially important for semi-transparent materials including some of the TBC materials (such as zirconia [14]) which are transmissive to the mid-infrared (MIR) (the dominant thermal wavelength at 700 °C is about 3 μm). Controlling the heat transfer with the often-coupled conduction and radiation heat transfer modes at high temperature becomes important when designing thermal

insulation materials. Therefore, in this dissertation, we aim to understand the coupled conduction-radiation heat transfer at high temperature.

1.4 Dissertation structure

In this dissertation, Chapter 1 introduces the background and motivation for studying the characteristic length in both PCHT and high temperature heat transfer, and provides a brief overview of past research on boiling and evaporation (Section 1.2) and high temperature TBC materials (Section 1.3). Chapter 2 discusses the thin film boiling concept and explains the mechanisms for the significantly enhanced heat transfer performance of thin film boiling. The experimental methodology to investigate the thin film boiling phenomena, including sample preparation procedure, experimental setup, measurement principle, and error analysis is also presented. Using water as the working fluid, ultrahigh heat flux by thin film boiling is experimentally achieved. In Chapter 3, a systematic study is performed which explored the interesting reversible heat transfer feature, demonstrated universal thin film boiling behavior and universal transition between thin film boiling and evaporation for various fluids, and elucidated the criteria and the underlying mechanisms governing the transition. The fundamental heat transfer condition at the transition points is found to be close to the kinetic limit. Chapter 4 describes a transient coupled conduction-radiation heat transfer model, which is used to extract the conductive thermal diffusivity from laser flash measurement and separate the radiation contribution from conduction. Finally, Chapter 5 summarizes the findings of this dissertation and provides roadmaps for future work.

Chapter 1, in part, is a reprint of the material as it appears in "Transition between thin film boiling and evaporation on nanoporous membranes near the kinetic limit", *International Journal of Heat and Mass Transfer* 154 (2020): 119673, by Qingyang Wang, Yang Shi, and Renkun Chen [147]. The dissertation author was the first author of this paper.

Chapter 1, in part, is a reprint of the material as it appears in "Advanced Materials for High-Temperature Thermal Transport", *Advanced Functional Materials* 30.8 (2020): 1904815, by Sunmi Shin*, Qingyang Wang*, Jian Luo, and Renkun Chen [148]. The dissertation author was the co-first author of this paper.

Chapter 2 Ultrahigh flux thin film boiling heat transfer through nanoporous membranes

2.1 Introduction

Liquid-vapor phase change heat transfer is fundamentally important for a variety of processes, such as power generation, refrigeration, water desalination and purification, and thermal management of high-power electronics [15-22]. Boiling is considered a promising cooling technique compared with other liquid-vapor phase change cooling phenomena such as jet impingement, spray cooling and thin film evaporation, which either have high operating temperature or have yet to be developed to achieve high heat fluxes [149, 150]. Both flow boiling and pool boiling has been studied extensively to enhance both critical heat flux (CHF) and heat transfer coefficient (HTC) [18].

In pool boiling, a heated surface is submerged inside a stagnant liquid pool, and the nucleation and subsequent bubble growth and departure carry the heat away from the heater. As a result, the CHF and heat transfer behaviors for pool boiling are largely dictated by the bubble dynamics. There are two different limiting cases associated with bubble evolution in pool boiling [151]. When the bubbles are small, the bubble growth is in the inertia-controlled regime where the growth is rapid and is limited by the inertia force of the surrounding liquid, and all the interface area has large superheat. When the bubble size increases and exceeds the thermal boundary layer thickness as shown in Figure 2.1 (a), the further growth of the bubble is in the heat-transfer-controlled regime, where the growth is slow due to the depleted superheat at the liquid-vapor interface. While it is evident that the

inertia-controlled regime is more desirable for more efficient heat transfer due to the faster bubble growth, it is difficult to prevent the transition into the heat-transfer-controlled regime as the bubbles grow. Therefore, pool boiling typically has low CHF, e.g., ~100 W cm^{-2} for water at the atmospheric pressure. Various strategies have been explored to study the bubble dynamics and enhance pool boiling CHF [30, 37, 39, 42, 152-154], but the CHF still remains below 250 W cm^{-2}.

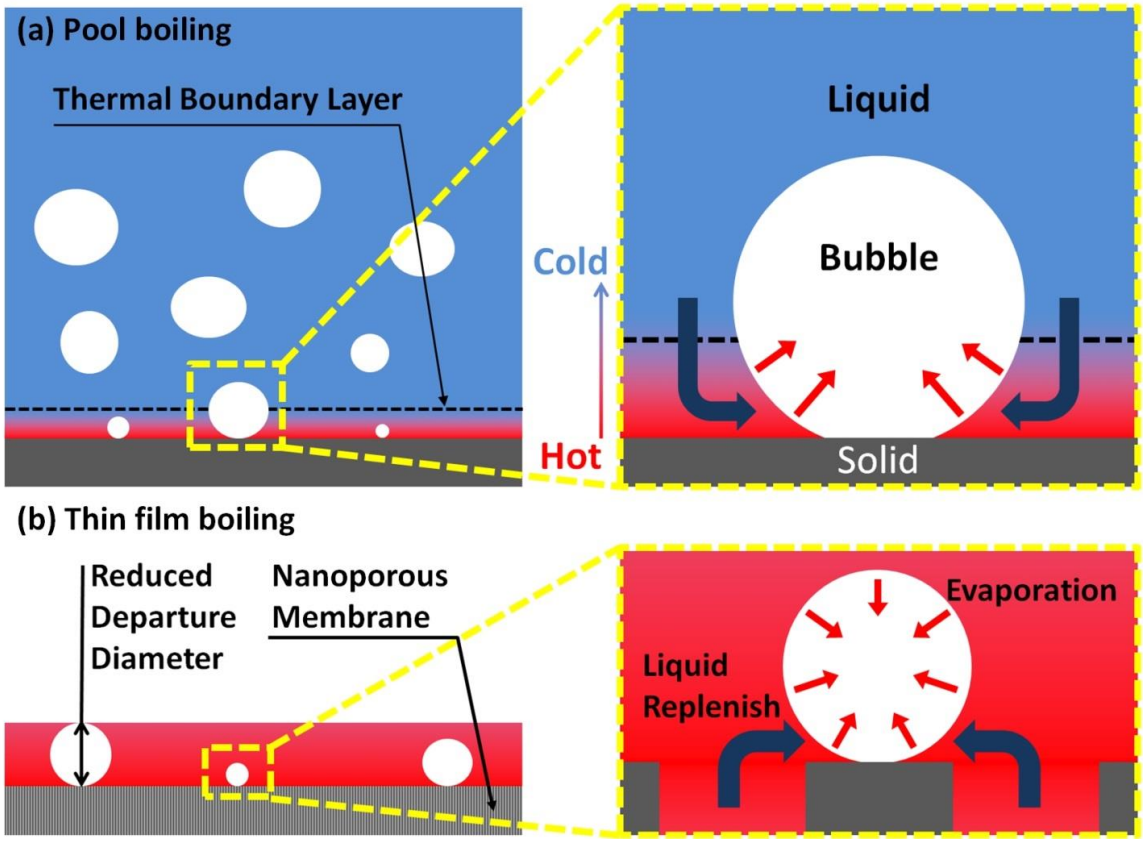

Figure 2.1: Schematics of the bubble growth behavior in (a) pool boiling and (b) thin film boiling. Different from pool boiling, when the liquid film thickness is smaller than the thermal boundary layer thickness in thin film boiling, the bubble growth is in the inertia-controlled regime where all the interface area participates in efficient evaporation. The bubble departure diameter is limited by the liquid film thickness. The liquid replenishment from the pores reduces the lateral length for liquid transport.

Flow boiling, on the other hand, can utilize fluid pumping to facilitate the bubble dynamics, as the liquid coolant is forced to flow along heated channels and the bubbles can be removed by the external pumping force. Therefore, flow boiling often has a higher CHF compared to pool boiling, especially in microchannels having small hydraulic diameter and consequently a large surface area-to-volume ratio. Recently, microchannel flow boiling devices with cooling flux close to or above 1 kW cm^{-2} has been reported with different channel configurations [53, 54, 155]. Other heat sinks [49, 69] implementing boiling heat transfer using three-dimensional (3D) geometry also show CHF over 1 kW cm^{-2}. In these cases, the channels, grooves and pin fins made of high thermal conductivity materials (such as Si, Cu and diamond) are the key to spread the ultrahigh heat flux from the heater area to the extended surface area, thereby effectively reducing the heat flux on the actual phase change area to be well below 1 kW cm^{-2}.

Despite these innovative 3D device designs achieving high CHFs, an interesting question still remains: what would be the upper limit of the heat flux in boiling heat transfer from *a planar surface*? The answer to this question would not only have fundamental significance on exploring the limit of phase change heat transfer but could have implications on future development of high power thermal management technologies as any enhancement on planar surface can be implemented into 3D architectures. In this work, we utilized a simple nanoporous membrane structure that exploits the benefits of both flow boiling and pool boiling, and realized a new boiling scheme, termed “thin film boiling”, with an unprecedentedly high CHF on a planar surface.

2.2 Thin film boiling concept

We propose a thin film boiling concept, which represents boiling heat transfer happening inside a thin liquid film. As shown in Figure 2.1 (b), the boiling occurs on the heated surface of a nanoporous membrane, and the resulting bubbles carry the heat from the solid surface to the vapor space, as in the case of pool boiling. However, instead of having an extensive liquid pool, the liquid film is very thin and spontaneously becomes thinner as heat flux increases, which results in a reduced thermal resistance for conduction and renders the entire bubble growth process within the inertia-controlled regime. Consequently, the bubble departure size is small due to the constraint of the liquid film thickness, which promotes the bubble departure. Further, the liquid is supplied from the nanoporous substrate through liquid pumping akin to flow boiling, rather than from the lateral liquid replenishing mechanism as in typical pool boiling. Therefore, separate liquid-vapor pathways [43, 47] can be created for better heat transfer performance. Moreover, earlier work [156] has shown that increased heater area resulted in decreased heat flux in microstructures for phase change heat transfer due to the longer distance for liquid transport. In the current configuration, the liquid is supplied in the cross-plane direction of the membrane, which ensures that the heat/mass transfer mechanisms will not be affected when scaling up to larger heater area.

2.3 Experimental methodology

2.3.1 Overview of experimental methods

The idea of thin film boiling concept in this dissertation is realized using a nanoporous membrane configuration. We experimentally investigated the phase change

heat transfer performance of this proposed configuration using various working fluids and nanoporous anodic aluminum oxide (AAO) membranes as the porous substrates (Figure 2.2 (a,b)). Liquid was driven across the membrane by pressure difference between the liquid and vapor sides of the membrane (Figure 2.2 (c)).

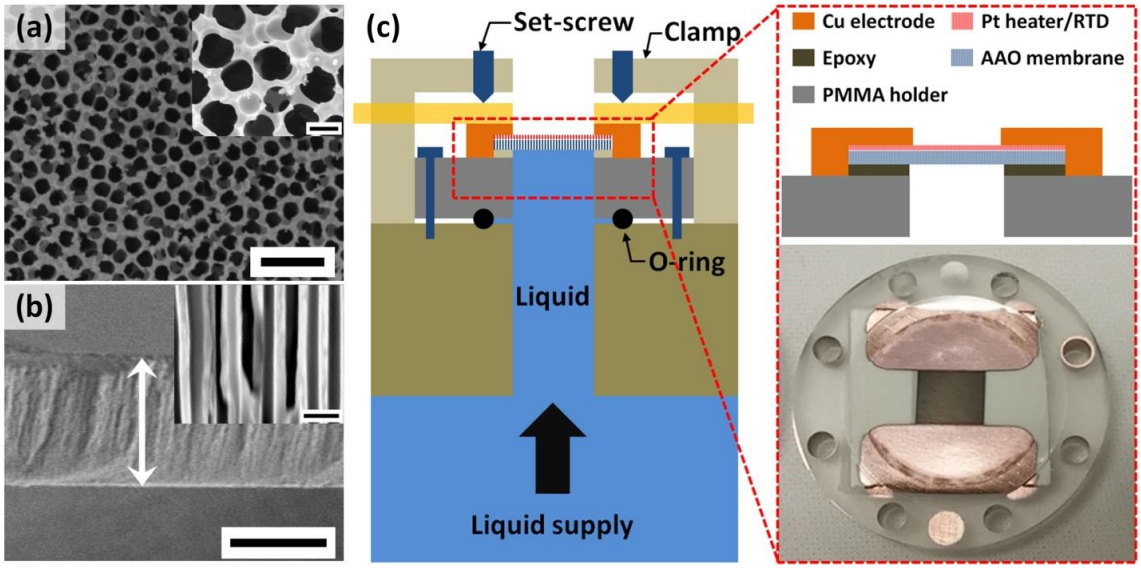

Figure 2.2: (a) and (b): SEM images of the AAO membrane, (a) Top view; (b) cross-sectional view. Scale bar: (a) 1 µm (inset: 200 nm); (b) 50 µm (inset: 500 nm). (c) Schematic and photo (zoomed-in bottom) of the sample assembly for the experiment.

Commercial AAO membranes with nominal pore size of 200 nm and thickness of 60 µm were characterized with scanning electron microscope (SEM) as shown in Figure 2.2 (a) and (b), for the top view and cross-sectional view, respectively. The membrane was attached onto a PMMA sample holder with a 0.71 × 0.71 cm^2 (0.50 cm^2) square hole with blade casted Torr Seal® Low Pressure epoxy. After epoxy curing, a ~70 nm thick square Pt layer with the same size as the holder opening and two 2 µm thick Cu contact pads connected to the heater were deposited by sputtering (Figure 2.2 (c) zoomed-in view). The

exact sizes of the Pt layer and the Cu pads were precisely determined by shadow masks fabricated using a computer numerical controlled (CNC) milling machine. A 10 nm thick Cr layer was sputtered and served as an adhesion layer before both Pt and Cu deposition processes. The Pt layer served as both a heater and a resistance temperature detector (RTD).

After the deposition of the Pt heater and the Cu contact pads, the PMMA sample holder attached with the AAO membrane was assembled onto a custom-made liquid supply channel using screws and O-ring sealing. The low thermal conductivity of PMMA ensures good thermal insulation and minimizes conduction heat loss (Section 2.3.6). To make good electrical contacts to the Cu pads, thick Sn foils were pressed against the contact pads using custom-made PMMA clamps and set screws, as shown in Figure 2.2 (c).

During the experiments, the pressures of both the vapor side (top) and liquid side (bottom) of the membrane were controlled and maintained at preset values. The heating power was applied to the sample through direct current (DC) power supply to the Pt heater incrementally and the corresponding temperature was determined by the Pt RTD. The heat flux reported in this study was the actual heating power divided by the physical area of the AAO membrane (0.5 cm^2). Heat transfer experiments were performed under variable liquid pressures, while the vapor pressure was maintained at the saturation pressure at 20 °C (17.5 Torr for water and 44.4 Torr for ethanol) for all the tests. Other details of experimental methodology will be presented in following sections.

2.3.2 Membrane characterization

Nanoporous membranes purchased from Sigma Aldrich (Whatman, 6809-6022) have nominal 0.2 μm pore diameter and 60 μm thickness. The membrane was characterized

by SEM as shown in the Figure 2.2 (a) and (b). The thickness of the membrane was measured for four different membranes from cross-sectional SEM images and averaged to be 61.46±5.76 μm. The membrane has straight pores as seen from the cross-sectional SEM image in Figure 2.2 (b). Therefore, the porosity η can be assumed to be represented by the pore area fraction from the top view image. Top view SEM images for five different membranes were analyzed and the porosity was averaged to be 47.06±4.61%. The pore size measured from the top view image can be used to represent the average channel size. Figure 2.3 (a) shows the SEM image used for pore size analysis while Figure 2.3 (b) shows the corresponding picture showing pore boundaries determined by ImageJ. The area A_p and the perimeter p of each pore were measured by the software. Due to the irregular shape of the pore, the hydraulic diameter $D_h = \frac{4A_p}{p}$ is used to represent the diameter of the pore. The circularity factor $f_c = \frac{4\pi A_p}{p^2} \leq 1$ describes how close the shape of the pore is to a perfect circle where $f_c = 1$. Here we eliminated the pores that have unclear boundaries and/or connected to each other for better accuracy by only recording the counts with $f_c \geq 0.5$. The pore size distribution is shown in Figure 2.3 (c). The averaged pore diameter is 239.31±18.68 nm.

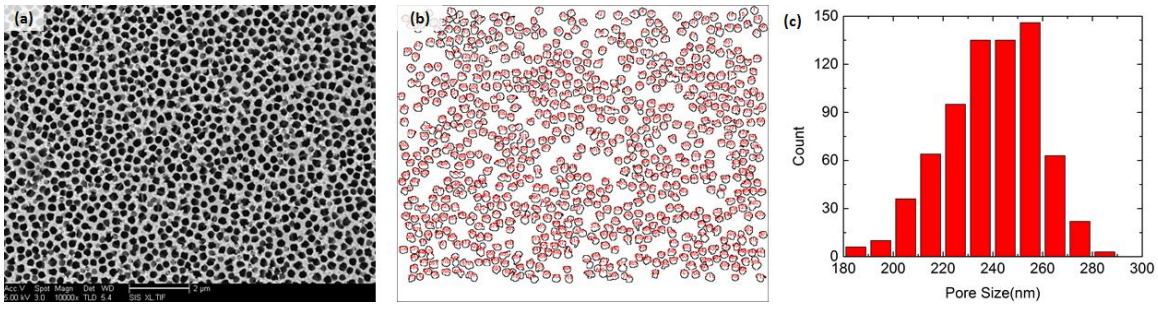

Figure 2.3: Membrane characterization. (a) Top view SEM image of the membrane (scale bar: 2 μm); (b) ImageJ analyzed pore boundary; (c) Pore diameter distribution graph.

2.3.3 TCR calibration of the Pt layer

The Pt layer deposited on top of the membrane served as both a heater and a resistance thermometer. The temperature coefficient of resistivity (TCR) of the Pt layer was calibrated for five samples and the averaged value was used in data processing. After Pt deposition, the sample was placed in a convective oven, where the temperature was controlled at a step-wise manner with 5 °C interval, and a K-type thermocouple was placed adjacent to the membrane (~1 mm above). Each step was held for 3 hours for temperature stabilization. The resistance and temperature were recorded simultaneously. Figure 2.4 shows a typical data set of the calibration. The resistance of the heater shows good linear relationship with temperature. The averaged calibrated TCR value was 0.00112±0.00010 $°C^{-1}$.

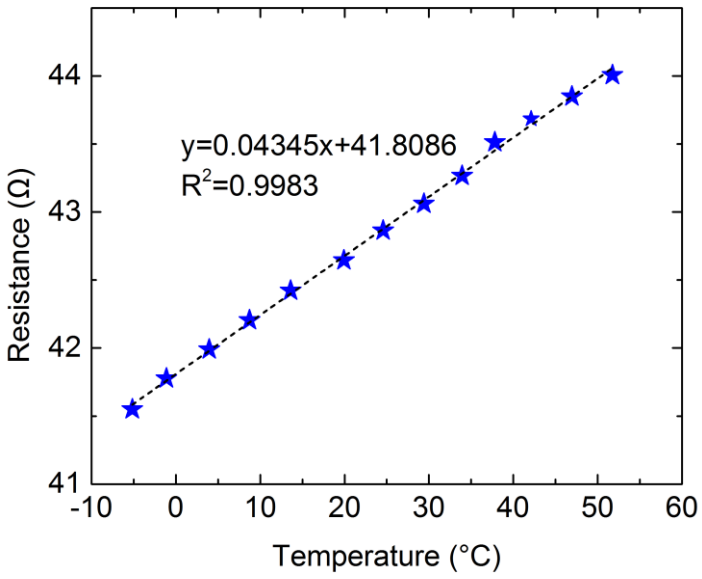

Figure 2.4: TCR calibration curve of the Pt layer.

2.3.4 Sample assembly

Figure 2.5 (a) shows the photo of the sample mounted on the Acrylic sample stage inside the vapor chamber, which was also schematically depicted in Figure 2.2 (c). To make good electrical contacts to the Cu pads, thick Sn foils were pressed against the contact pads using custom-made PMMA clamps and set screws, as shown in Figure 2.5 (a). Figure 2.5 (b) shows the procedure to assemble the sample. Figure 2.5 (c) shows the photo of the vapor chamber consisting of an aluminum chamber (to collect overflowed liquid) and a glass cover (to visualize the experiments). The electrical feedthrough into the vapor chamber is on the back side of the aluminum chamber and connected to the computer.

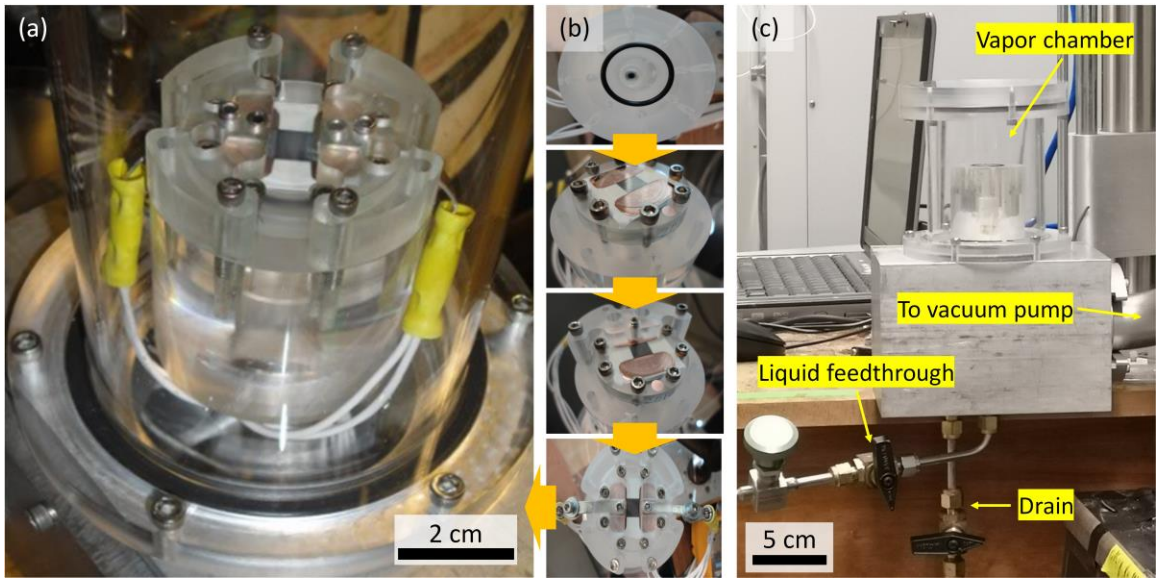

Figure 2.5: (a) Photo of one sample mounted for experiment. (b) Procedure of assembling one sample into the vapor chamber shown in (a). (c) Photo of the vapor chamber without sample.

2.3.5 Experimental procedure

A schematic diagram of the experimental setup is shown in Figure 2.6. Two vacuum sealed chambers are used in the experiments, served as vapor chamber and liquid chamber, respectively. For experiments using DI water as the working fluid, liquid was first degassed by vigorous boiling inside the water reservoir at 17.5 torr (saturation pressure of water at 20 °C) for a few minutes before each experiment. Before supplying water to the sample, the vapor chamber was pumped down by a vacuum pump to the saturated pressure of water vapor at 20 °C (~17.5 torr). The liquid chamber was pumped down (when the preset pressure is smaller than ambient pressure) by a vacuum pump or pressurized (when the preset pressure is larger than ambient pressure) by an air compressor to the preset liquid pressure. By carefully opening the valve, water was supplied from the reservoir to the bottom of the sample and flowed through the pores of the membrane. The vapor chamber pressure was maintained at 17.5 torr using PID control during the whole experiment. Heating power was supplied to the heater layer using a DC power source (Agilent 6575A #J09), and the heating current and voltage of the heater was recorded simultaneously using two digital multimeters (Agilent 34401A) at a 1 Hz frequency. Temperature of the heater was obtained from reading the resistance change and using the pre-calibrated temperature coefficient of resistivity (TCR) of the Pt RTD. After pressures of both chambers were stable, water was supplied to the bottom of the sample and flooded on top of the membrane. Heat flux was applied to the Pt heater incrementally. At each heat flux step, the system was allowed to reach the steady state (usually within ten seconds) and then the temperature was recorded continuously for at least 30 seconds before moving to the next step. Heat flux and corresponding temperature were averaged during the steady state period of each heat flux

level. HTC was calculated by dividing the heat flux by the temperature increase of the membrane compared with the saturation temperature of water in the vapor chamber (20 °C). CHF was reached when a drastic increase in temperature was recorded, after which the membrane usually broke within a few seconds due to overheating. High speed images were recorded with an IL-5 high speed camera (Fastec Imaging). All the samples were tested until CHF was reached.

For experiments using ethanol as the working fluid, all procedures are the same as described above except the pressure for liquid degassing and the vapor chamber pressure were 44.4 Torr instead.

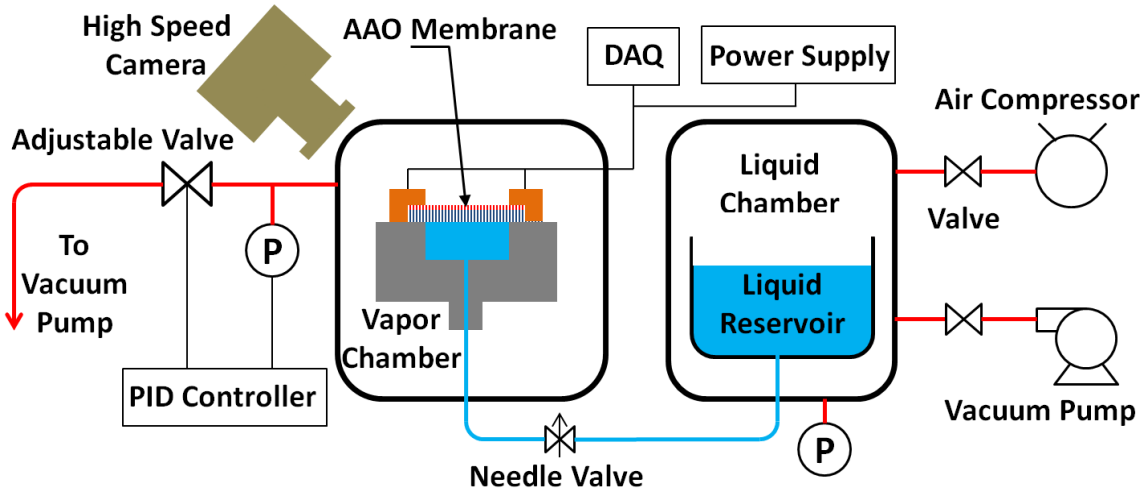

Figure 2.6: Schematic of the experimental setup.

2.3.6 Conduction heat loss

Aside from the sensible and latent heat of the liquid, the applied heat flux during the experiment can also be dissipated by heat conduction through experimental fixture. The heat loss through the fixture was measured by applying heat flux to one sample in the

experimental chamber with the same conditions except without liquid supply. As shown in Figure 2.7, the conduction heat loss is linearly related to the sample temperature with a slope of ~0.00171 W K^{-1}. The maximum heater temperature during the whole experiment was below 100 °C, indicating a maximum heat loss of less than 0.171 W or 0.342 W cm^{-2}, which is negligible compared with the heat flux recorded in the experiments.

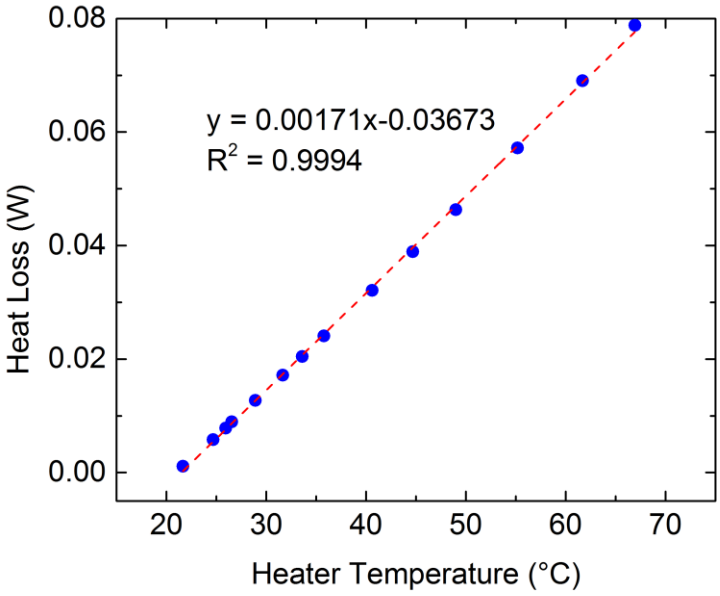

Figure 2.7: Measured conduction heat loss as a function of the heater temperature.

2.3.7 Effect of water electrolysis

During the experiments with water as the working fluid, Pt heater was in contact with water and under high DC voltage. It is possible that water electrolysis can happen and dissipate the power supplied to the heater, although DI water with resistivity of 18 Ω-cm was used in the experiments and nearly zero electrical current went through water. In order to eliminate this effect, we followed Wilke's work [157] and fabricated a sample with open circuit heater for electrolysis as shown in Figure 2.8 (a). The measured current versus

supplied voltage was shown in Figure 2.8 (b). During the real experiments, the maximum supplied voltage was below 110 V (the instrument limit), corresponding to a maximum power dissipated by electrolysis of less than 0.02 W. Therefore, the water electrolysis was negligible compared with the power dissipated by heat transfer.

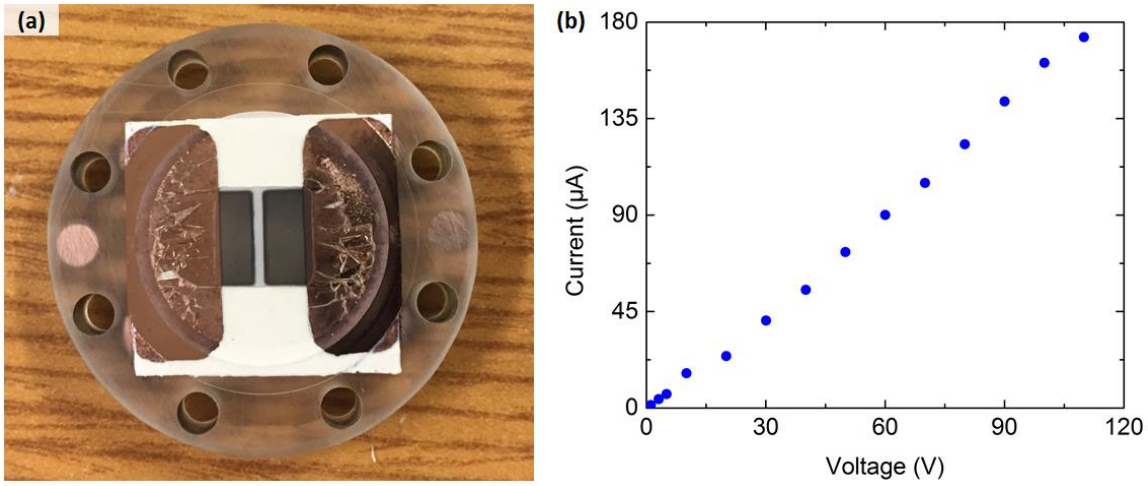

Figure 2.8: (a) Sample fabricated for water electrolysis test. (b) Current vs voltage during water electrolysis test.

2.3.8 Uncertainty analysis

The errors in a steady state measurement mainly come from instrument as well as standard deviation (STD) through the measured time. The total measurement error of quantity M can be expressed as $|\delta M| = \sqrt{(\delta M)_{ins}{}^2 + (STD)_M{}^2}$.

The heat flux in the experiments was given by $q'' = \frac{VI}{A}$ where V and I are the voltage and current applied on the heater, respectively, and A is the heater area. Voltage V was measured by an Agilent 34401A digital multimeter. During the experiments, the minimum voltage recorded was above 10 V. The instrument gives an error of 0.0020% of

reading + 0.0006 % of range for both 10~100 V and 100~1000 V measurement range. Therefore, before voltage exceeded 100 V, the maximum instrumental error was $\left|\left(\frac{\delta V}{V}\right)_{ins}\right| = 0.0020\% + 0.0006\% \times \frac{100}{10} = 0.008\%$ while after the voltage exceeded 100 V, the maximum instrumental error was $\left|\left(\frac{\delta V}{V}\right)_{ins}\right| = 0.0020\% + 0.0006\% \times \frac{1000}{100} = 0.008\%$. The standard deviation of the voltage for a steady state measurement at highest voltage level was below 0.005 V. Therefore, the maximum error in the voltage measurement is $\left|\frac{\delta V}{V}\right| = \sqrt{0.008\%^2 + \left(\frac{0.005}{10}\right)^2} = 0.05\%$. Similarly, the maximum error in the current measurement is $\left|\frac{\delta I}{I}\right| = 0.35\%$. The heater area was dictated by the sputtering masks which were fabricated by computer numerical controlled milling machine with negligible error. The maximum error for heat flux is thus $\left|\frac{\delta q''}{q''}\right| = \sqrt{\left(\frac{\delta V}{V}\right)^2 + \left(\frac{\delta I}{I}\right)^2} = 0.35\%$.

The wall superheat was calculated by $\Delta T = \frac{R - R_0}{R_0 \times TCR}$. The sample resistance $R = V/I$ has an error of $\left|\frac{\delta R}{R}\right| = \sqrt{\left(\frac{\delta V}{V}\right)^2 + \left(\frac{\delta I}{I}\right)^2} = 0.35\%$. The initial sample resistance R_0 has the same maximum error $\left|\frac{\delta R_0}{R_0}\right| = \left|\frac{\delta R}{R}\right| = 0.35\%$. The TCR value has an error of $\frac{\delta(TCR)}{TCR} = 8.93\%$. Therefore, the maximum error for ΔT is $|\delta(\Delta T)| = \sqrt{\left(\frac{\partial(\Delta T)}{\partial R}\right)^2 (\delta R)^2 + \left(\frac{\partial(\Delta T)}{\partial R_0}\right)^2 (\delta R_0)^2 + \left(\frac{\partial(\Delta T)}{\partial(TCR)}\right)^2 \left(\delta(TCR)\right)^2}$. Due to the large error coming from the TCR value, it is reasonable to ignore errors from resistance measurement, meaning $\left|\frac{\delta(\Delta T)}{\Delta T}\right| \approx \left|\frac{\delta(TCR)}{TCR}\right| = 8.93\%$.

Pressure of the vapor chamber was controlled by the PID valve and recorded by pressure transducer (MKS Baratron® Type 127A) which has an accuracy of less than 0.25% for the measurement range, or an error of ~0.04 torr. Pressure of the liquid chamber was measured by two pressure gauges (McMaster-Carr) with minimum scale equal to 0.5 inHg (12.7 torr) and 0.5 psi (25.9 torr) for pressures below and above atmospheric pressure, respectively, corresponding to a reading error of 6.4 torr and 13.0 torr, respectively. The error for the pressure difference is therefore the same as the error for the liquid pressure.

2.4 Results and discussion

Our experiment is a hybridization of flow boiling and pool boiling, as the liquid (water) was pumped through the porous AAO membrane using the pressure difference between the liquid pressure (P_l) and vapor pressure (P_v) (Figure 2.2 (c)). Different from flow boiling where liquid is also pumped and flows along the microchannels, this pumping force does not cause convective boiling inside the nanopores (as discussed later). Rather, the liquid pumping is only used to overcome the viscous resistance of liquid transport through the nanopores and to ensure a liquid film is efficiently replenished on top of the membrane (Figure 2.1 (b)). As we shall see later, the membrane was covered with a liquid film throughout the entire experiment, so the phase change surface area was the same as the heater area. Figure 2.9 shows the boiling curves, or heat flux versus the superheat. Here the heat flux is defined as the applied heating power divided by the physical area of the membrane (0.71×0.71 cm^2, 0.50 cm^2). Each curve in Figure 2.9 represents one sample tested at a certain liquid pressure, and each data point in the curve represents values averaged over the time of one steady state measurement (at least 30 seconds). Figure 2.10

shows the high-speed camera images of the boiling surface at different heat fluxes for a specific test with the liquid pressure of 760 torr.

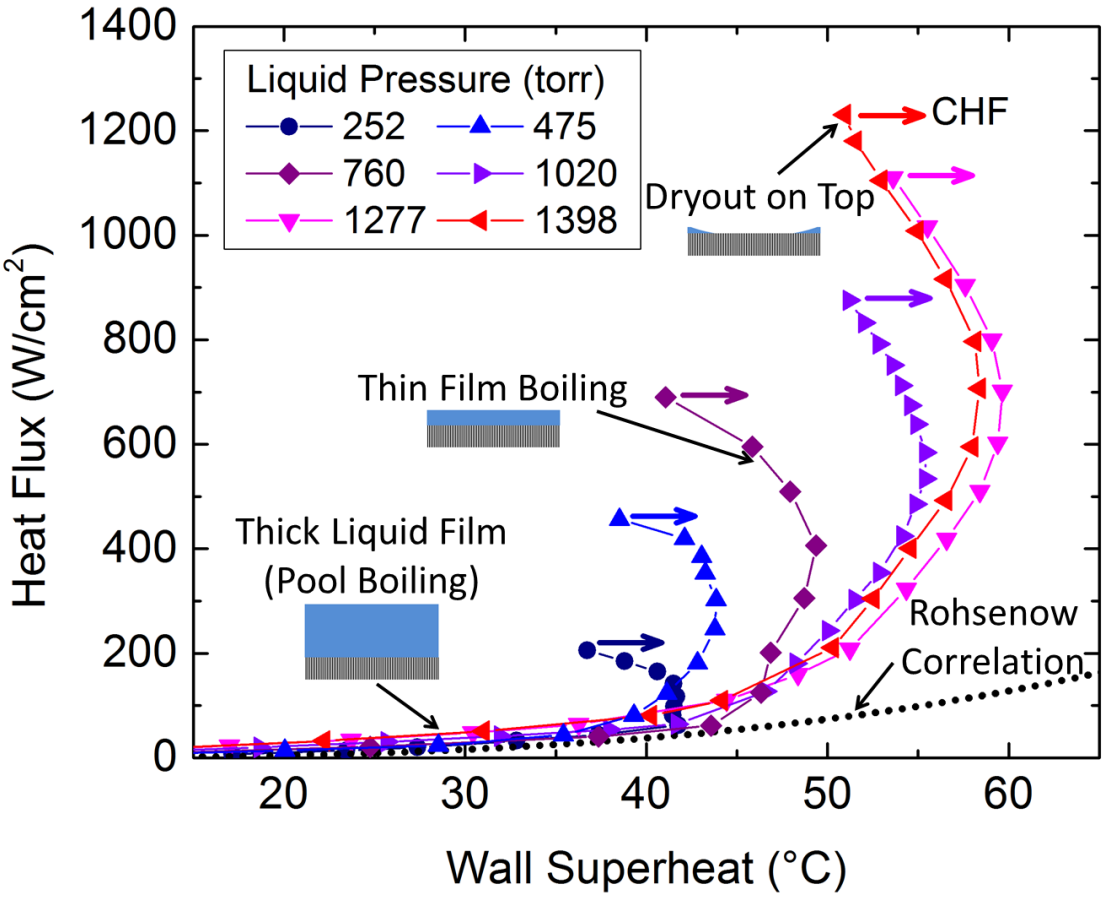

Figure 2.9: Boiling curves under different liquid pressures. The vapor pressure was maintained at 17.5 torr (20 °C saturation temperature). The arrows indicate the CHF for each curve. The highest CHF of 1230.7 W cm^{-2} was achieved with liquid pressure at 1398 torr.

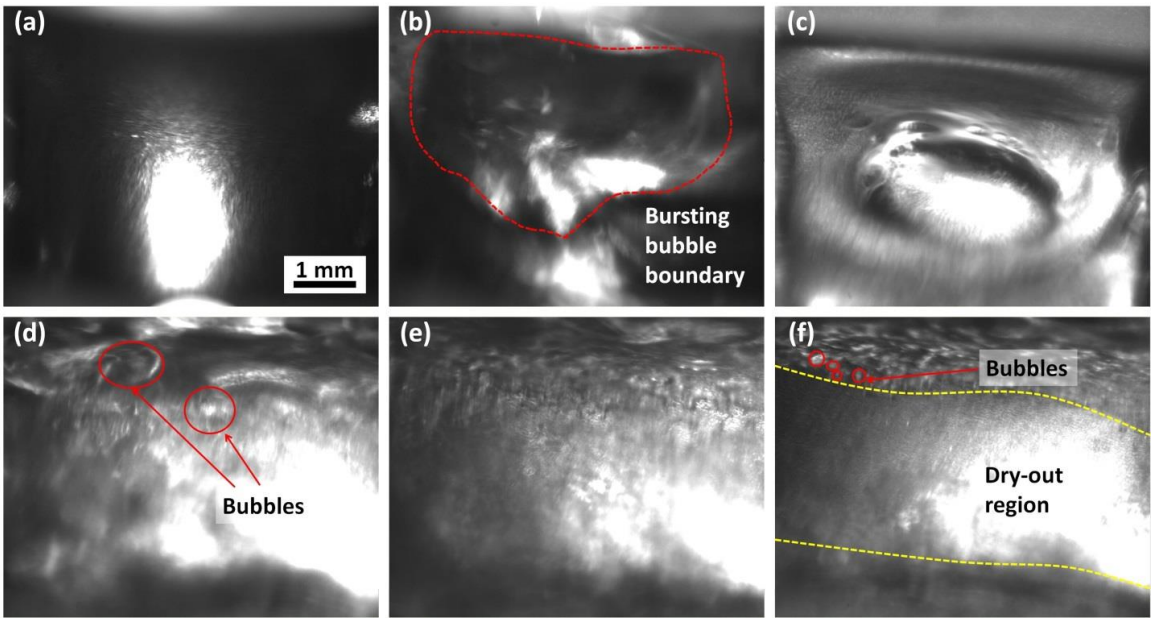

Figure 2.10: High speed images of the boiling surface at different heat fluxes under 760 torr liquid pressure. (a) 0 W cm^{-2}, thick liquid puddle formed on top of the membrane, the white part was the reflection of light from the large liquid puddle; (b) 3.7 W cm^{-2}, bubble nucleation started; (c) 55.2 W cm^{-2}, a clear bubble base shows mm-scale bubble size; (d) 337.5 W cm^{-2}, bubbles were smaller than Rohsenow regime; (e) 571 W cm^{-2}, much smaller bubbles formed over the entire area; (f) 700 W cm^{-2} (near CHF), center dry out occurred on top of the membrane, while the surrounding area still showed small bubbles.

The boiling curves display a similar shape under different liquid pressures. At the beginning of the experiment with low heat flux, there was no bubble nucleation on top of the membrane. Water flooded on top of the membrane and formed a liquid layer, while the excess amount of liquid overflowed and dropped to the bottom of the vapor chamber. The liquid formed a thick puddle (>1 mm thick) on top of the membrane and the heat transfer mechanism was simply single phase convection (see Figure 2.10 (a)). Bubble nucleation started after the wall superheat exceeded ~5 °C, where the bubbles burst and the liquid splashed inside the chamber (as seen in Figure 2.10 (b)), and the heat flux was dissipated by both sensible and latent heat of the liquid. Since the heat flux causing the bubble nucleation (~5 W cm^{-2}) is usually orders of magnitude smaller than CHF in our

experiments, this onset of nucleate boiling was not shown in the graph in Figure 2.9. As shown in Figure 2.9, with relatively low heat fluxes, the boiling curves have a small slope and the boiling behavior is in the nucleate boiling regime and is well captured by the Rohsenow correlation [158], which relates the heat flux q'' to the superheat ΔT in nucleate boiling as

$$q'' = \Delta T k_l \sqrt{\frac{g(\rho_l - \rho_v)}{\gamma}} \frac{1}{{C_{nb}}^3 Pr^m} \left(\frac{c_p \Delta T}{h_{fg}}\right)^2 \tag{2.1}$$

where g is the gravitational acceleration, k_l, ρ_l, ρ_v, γ, Pr, c_p, and h_{fg} are the liquid thermal conductivity, liquid density, vapor density, surface tension, liquid Prandtl number, liquid specific heat, and latent heat of vaporization, respectively. The constants C_{nb} and m are chosen as 0.013 and 2, respectively, for water on platinum surface [158]. The agreement between the experimental boiling curves and the Rohsenow correlation can be attributed to the thick liquid layer on top of the membrane acting as a liquid pool, as in the case of pool boiling.

As the heat flux kept increasing, the boiling curves deviated from Rohsenow correlation and started to show a gradually larger slope, and, after a certain heat flux, an even negative slope. This behavior, a clear departure from the pool boiling as described by the Rohsenow correlation, can be attributed to the thin liquid film formation on the heater. When the film thickness is smaller than the bubble departure diameter in pool boiling (mm-scale), the boiling behavior would deviate from pool boiling.

The increasing and the eventual negative slopes in the boiling curves at the high heat flux are the hallmarks of the thin film boiling regime. The behavior can be attributed to the following factors: with increasing heat flux, as more liquid was vaporized while the

mass flux was constant with a fixed pressure difference between liquid and vapor chambers ($\Delta P = P_l - P_v$), the mass of excess amount of liquid that remained on top of the membrane decreased, which yielded a decreasing liquid layer thickness. In fact, at higher ΔP, the boiling curves deviated from Rohsenow correlation at a higher heat flux and wall superheat, which can be attributed to higher liquid mass flux delaying the onset of the thin film boiling regime. Previous work [156] with Si micropillars also showed very similar thin film boiling behavior with high heat flux, in which the liquid film thickness was mainly determined by the pillar height.

The negative slopes in the boiling curves, that is, a decrease in wall superheat with increasing heat flux at high fluxes, can also be understood from the thin film geometry. Similar phenomena have been observed in the literature and were usually due to the hysteresis associated with the activation of nucleation sites, and therefore were usually observed at the onset of the nucleate boiling. However, this negative slope, termed "boiling inversion" in Kandlikar's work [159], could also result from enhanced macroconvection [36]. In our study, due to the unique thin liquid film configuration, three possible mechanisms can explain these negative slopes, namely, the enhanced conduction inside the liquid layer, the promoted bubble departure, and the separate liquid-vapor pathways.

Thinner liquid layer at higher heat flux reduces the conduction thermal resistance inside the liquid layer and consequently provides inertia-controlled bubble growth. We hereby analyze an exemplary boiling curve with $\Delta P = 1259.5$ torr (the magenta curve in Figure 2.9) as follows. Hsu [160] suggested the criteria for the incipience of nucleation for pool boiling as $\frac{12.8\sigma T_{sat}(P_l)}{\rho_v h_{fg} \delta_t \theta_w} = 1$, where σ, ρ_v, h_{fg} are the surface tension, vapor density, and latent heat of water, respectively. In this particular test, bubbles were observed at a

wall superheat of 16.2 °C (which is the first point recorded on this curve). Therefore, the incipience of nucleation occurred before the wall superheat θ_w reached 16.2 °C, which yields a thermal boundary layer thickness δ_t larger than 395 μm. The thermal boundary layer thickness of nucleate boiling can also be estimated by [161] $\delta_T = 3.22k/h_{boil}$ where k is the liquid thermal conductivity and h_{boil} is the boiling heat transfer coefficient, which results in an estimated thermal boundary layer thickness of ~200 μm at the transition of pool boiling to thin film boiling in this work (at $\Delta T \sim 40$ °C), which is within the same order of magnitude with the thermal boundary layer thickness estimated before. Therefore, it is expected that a liquid layer thinner than ~100s μm will result in notable heat transfer enhancement. The liquid layer thickness close to CHF is estimated to be tens of microns (see Section 2.4.3). During experiments, the liquid layer thickness would decrease from >1 mm at zero heat flux to zero at CHF (since the layer dries out at CHF), which means that at certain heat flux, the liquid layer thickness will be smaller than this thermal boundary layer thickness. Therefore, at sufficiently high heat flux, the liquid layer on top of the membrane will be superheated and the temperature of the whole liquid layer will be close to the wall temperature as depicted in Figure 2.1 (b). The small thickness and the superheating of the liquid pool resulted in the enhanced conduction inside the liquid layer and therefore the bubble growth of the boiling process was entirely in the inertia-controlled regime, in which all of the liquid-vapor interface area was efficiently evaporating and the bubble growth was fast for the entire growth period.

The second possible reason for the reduced overall thermal resistance is the promoted bubble departure in the thin liquid layer. For an extensive liquid pool, the bubble departure diameter d_d is usually comparable with the capillary length [151] $l_c =$

$\sqrt{\frac{\sigma}{g(\rho_l-\rho_v)}}$. Given water properties at 20 °C, $l_c \approx 2.7$ mm is at least one order of magnitude larger than the liquid pool thickness at high heat fluxes. Therefore, the bubbles in the thin liquid film would depart before growing to the size of l_c; hence, the real bubble departure diameter would be close to the liquid layer thickness. Although it is difficult to obtain a clear bubble boundary from the images at high heat flux due to the interference of the fluctuating liquid layer and the intensive ejection of liquid above the sample, it can still be seen that the relative bubble size in Figure 2.10 (d-f) (in the high heat flux regime) is much smaller than both the characteristic length of ~2.7 mm and the bubble size at low to moderate heat flux in Figure 2.10 (b) and (c). This indicates that the bubble departure will happen much more frequently than that in normal pool boiling with the same superheat due to the small liquid thickness and the dominantly inertia-controlled growth regime, which can also be responsible for the greatly enhanced heat flux beyond the Rohsenow regime.

Another possible mechanism responsible for the heat transfer enhancement is the efficient liquid replenishment. Since the heat flux was supplied to the solid wall of the membrane, the nucleation will more likely to occur at the top of the solid walls and liquid is replenished after bubble departure. As shown in Figure 2.1 (b), we hypothesize that bubbles depart vertically upward while liquid was supplied to the nucleation sites laterally from the pores without interference, providing enhanced macro-convection heat transfer [36], which has been shown previously to cause boiling inversion [36, 47, 159]. The separate liquid-vapor pathways provided by the nanoporous configuration can also partly explain the heat transfer enhancement. Also, the lateral length-scale needed for liquid to travel in order to replenish the nucleation sites is on the order of several hundred

nanometers (determined by the pitch size between pores) and is much shorter compared with mm-scale (determined by bubble size) as in the case of pool boiling.

From Figure 2.9, it can be seen that the boiling heat flux of the nanoporous configuration in this work is clearly dependent on the pressure difference (ΔP) between the liquid chamber (P_l) and the vapor chamber (P_v). The CHF of nanoporous surface increases with increasing ΔP, which can be explained by the limiting mechanism for CHF in the current configuration. In some of the boiling experiments on micro- or nanostructures, the capillary limit is the ultimate limit for the CHF condition [59-61, 162, 163]. Liquid-vapor interfaces confined in these structures generate large capillary force which drives the liquid to the phase-change sites and the CHF is achieved when the capillary driving pressure is balanced by the viscous drag of liquid transport. However, in our current configuration, the membrane was always covered by the liquid, and there was no meniscus liquid-vapor interface inside the nanopores of the AAO membrane. This is clearly shown in Figure 2.11, which depicts the CHF vs. ΔP with the linear fitting of the plot passing through the origin, meaning a zero heat flux (and mass flux) corresponding to no external liquid pumping pressure. Therefore, the driving force for liquid transport across the membrane comes *entirely* from the external pressure difference across the membrane, i.e., ΔP between the liquid chamber and the vapor chamber (the hydraulic resistance in the tubing is negligible). This pressure difference will provide an almost constant liquid mass flux inside the nanopores for each individual experiment with fixed ΔP (assuming the liquid properties are insensitive to temperature and pressure). CHF is achieved when the mass flux is completely vaporized and further increase of heat flux would result in membrane dry out.

Therefore, the increased ΔP in this configuration is thus similar to increased mass flux in a flow boiling device.

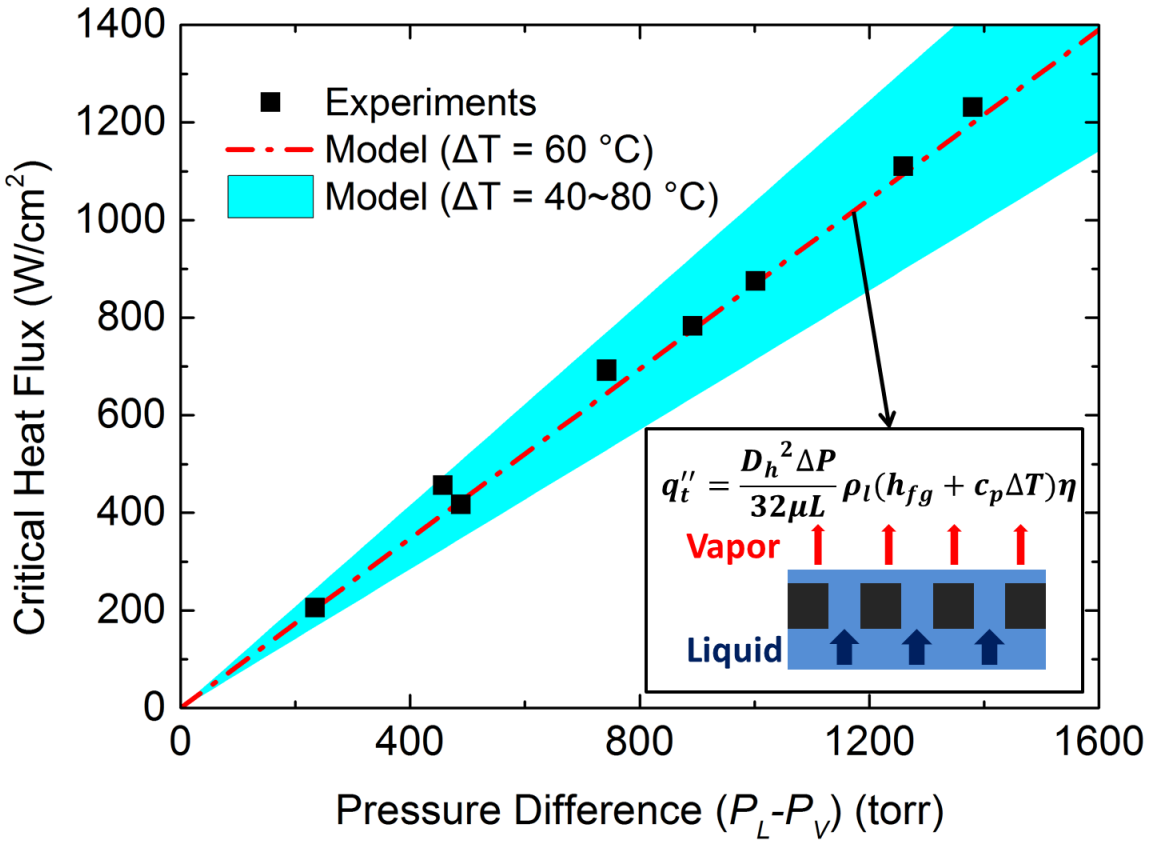

Figure 2.11: Experimental and theoretical CHFs vs. pressure difference. The experimental CHFs and modelling for theoretical CHFs with 60±20 °C superheat agree well. The linear extrapolation of the curve has a zero intercept at zero pressure difference, meaning no capillary pumping effect. The theoretical CHF model used Hagen-Poiseuille equation through circular pores to calculate the liquid mass flux and assumed all of the liquid was vaporized (see Section 2.4.1 for details).

The maximum heat flux that can be dissipated before membrane dry out can be expressed as $q_t'' = \dot{m}_{tot}(h_{fg} + c_p \Delta T)/A$ where $\dot{m}_{tot}$ is the total mass flux provided by the pressure difference. According to the laminar viscous flow theory, $\dot{m}_{tot}$ is proportional to ΔP, indicating that the total heat flux q_t'' is also proportional to ΔP, since water density and

latent heat do not vary too much with temperature and the sensible heat is an order of magnitude smaller than latent heat given the small temperature rise in the experiments. Figure 2.11 clearly shows that the experimental CHFs are linearly related to ΔP and match well with the theoretical results with wall superheat at 60 °C.

The maximum CHF of 1230.7 W cm^{-2} reported here is among the highest numbers for boiling heat transfer. Due to the nanoscale confinement of the pores, cavitation inside the pores is not expected (the critical bubble radius for water at 20 °C saturation temperature and 60 °C superheat is ~16 μm, much larger than the ~200 nm pore size), which indicates that the phase change occurred only on top of the membrane, and the actual phase change area is equal to the planar membrane area. Therefore, our current configuration does not rely on surface area enhancement and the nanoporous membrane is merely used for sustaining a thin liquid film to realize the proposed thin film boiling mechanism. This thin film boiling mechanism is different from most of the previous publications about micro/nanostructure enhanced phase change heat transfer [162, 163], and is a new approach for achieving high heat flux dissipation. It is worth mentioning that the ratio of power consumption of the liquid pumping and the maximum heat dissipation can be approximately estimated by $\Delta P/\rho_l h_{fg}$ and is less than 0.01% for the experiments of this work, indicating the potential benefit of implementation of thin film boiling into a high coefficient of performance heat sink, where the heat is conducted through microchannel ridges to the suspended nanoporous membranes, similar to the device structures demonstrated by Wang and coworkers [64, 68].

Although the liquid supply for vaporization in the present thin film boiling configuration is similar to traditional flow boiling, it does not experience the flow

instabilities commonly seen in flow boiling. During the experiments, the dynamic temperature profiles at each heat flux step was recorded and averaged. Figure 2.12 shows the temperature and heat flux profiles of one typical experiment (CHF=1230 W cm^{-2} with liquid pressure at 1398 torr). As opposed to flow boiling where dramatic temperature fluctuation exists, the current configuration showed stable wall temperature at all the range of heat fluxes with a small standard deviation of 0.19, 0.19, and 0.27 °C for heat fluxes of 12, 707, and 1230 W cm^{-2}, respectively. At low heat flux, similar to homogeneous nucleate boiling, temperature was stable because the bubbles at the local nucleation sites only occupy a small fraction of the entire area. The stability of temperature at higher heat flux can be attributed to the way liquid was supplied as well as the small thickness of the liquid layer. In flow boiling, due to the large volume expansion of liquid-vapor phase change as well as the compressibility of vapor in the confined channel, flow instabilities such as Ledinegg instability and pressure drop instability tend to happen [55, 164, 165]. In our current thin film boiling, liquid was supplied from the cross-plane direction through nanoscale pores, which suppressed the cavitation and bubble formation inside the pores. The phase change phenomenon happened on top of the membrane in a large vapor space, and therefore, flow instabilities can be eliminated. Furthermore, unlike flow boiling where the liquid mass flux decreases along the channel due to vaporization, in this configuration, the liquid mass flux at all locations of the heater surface was nearly the same. The thin liquid layer can also constrain the bubbles to a small diameter and prevent vapor accumulation. Therefore, the lateral coalescence of bubbles and the resulting formation of vapor blanket can be eliminated until the heat flux approaches CHF where vapor volume fraction is sufficiently high to form a local hotspot and cause dry-out.

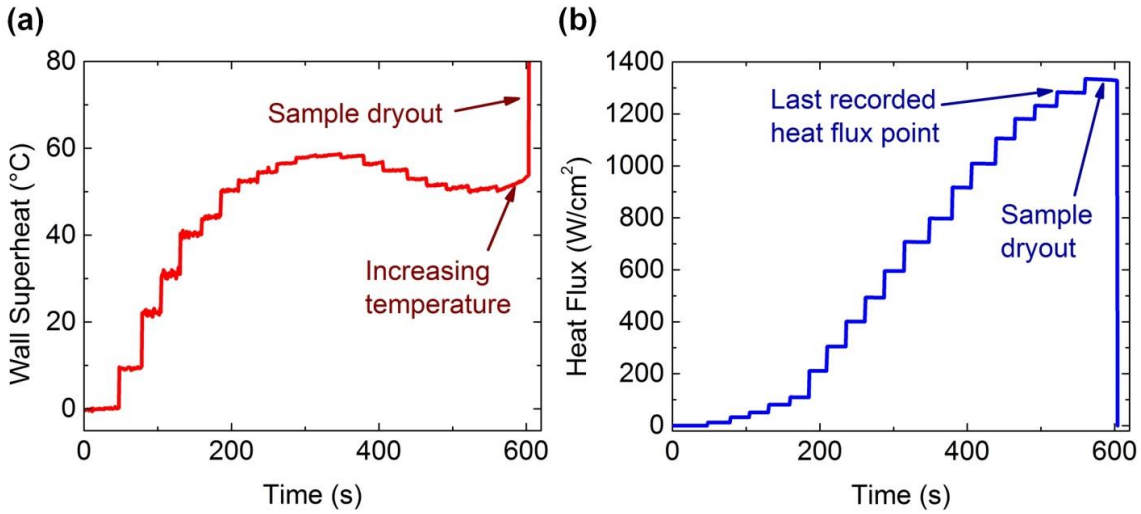

Figure 2.12: Dynamic temperature and heat flux profiles. (a) Temperature as a function of time. (b) Heat flux as a function of time. Data represents the experiment with 1398 torr liquid pressure (CHF at 1230 W cm^{-2}).

The heat flux observed in our study, up to ~1.23 kW cm^{-2}, is at least 10 times higher than previous work by Wang and coworkers [63, 67] on similar setups using AAO membranes. In Refs. [63, 67], after the top liquid layer dried out and all the liquid covering the membrane was vaporized, thin film evaporation from the nanopores will continue dissipating higher heat flux. Supposedly, after heat flux reaches a certain value such that the liquid covering the membrane is completely dried out, the liquid-vapor interface will recede inside the nanopores and form a meniscus shape, and consequently provide extra driving force for liquid supply by the meniscus-generated capillary pressure, as clearly observed in Refs. [63, 67]. However, in our experiments, from visual observation (Figure 2.10 (f)) as well as the dynamic temperature measurement in the experiment (Figure 2.12), the wall temperature kept increasing and could not reach a steady state as soon as a dry spot appeared on top of the membrane (Figure 2.12 and Figure 2.15); this overheating

eventually caused membrane failure and the CHF. Figure 2.10 (f) shows a typical image right before the CHF, which indicated that the central area of the membrane was dried out. Therefore, we infer that the evaporation regime with receding meniscus inside the pores could not be reached under our experimental conditions. This is further supported by the fact that the linear fitting of the CHF vs ΔP in Figure 2.11 has zero intercept at zero pressure difference, indicating the absence of the capillary liquid pumping.

Combing our observation and those from Wang and coworkers [63, 67], we suggest that the condition to reach the capillary-driven evaporation regime (with menisci residing inside the nanopores) depends on the heat flux prior to the dry out of the liquid layer covering the membrane. If the heat flux prior to the dry out is lower than what could be achieved in the capillary-driven evaporation inside the nanopores, then, with increasing heat flux, the phase change will transition to the evaporation regime after the dry out, as observed by Wang and coworkers [63, 67], where the heat flux for this transition was below 30 W cm^{-2} due to the much lower permeability of the AAO membranes they used (smaller pore size and lower porosity). In our experiments, the CHF in the thin film boiling regime (> 1 kW cm^{-2}) is likely already higher than the heat flux attainable from the evaporation inside the nanopores. Therefore, a stable evaporation regime could not be reached.

The remaining question is, of course, why the heat flux from the evaporation inside the nanopores is not higher (say, > 1 kW cm^{-2}). We hypothesize that the most probable reason is the vapor diffusion limit of the evaporation inside pores. The evaporation heat flux from nano-pores could be governed by three transport resistances: the hydraulic resistance of liquid transport, the kinetic limited interfacial resistance of evaporation, and the vapor diffusion resistance from interface to the far field in the vapor space. We can first

eliminate the hydraulic resistance limit because the capillary force would have provided extra driving pressure of several hundred kPa, which would have led to a heat flux much higher than 1 kW cm^{-2}, as we can infer from the heat flux vs. ΔP plot in Figure 2.11. Second, we can also estimate that the kinetic limit would have been much higher. Previous modeling work [65, 166] has shown that the kinetic limited heat flux of evaporation from nanopores can reach as high as several kW cm^{-2}. Recently, Duan and coworkers [167] experimentally measured the kinetic limit of water evaporation inside nanochannels and found that the kinetic limited evaporation heat flux was even an order of magnitude larger than theoretical prediction. Therefore, the heat flux at the moment of liquid layer dry-out in our experiments was still lower than the kinetic limit. Therefore, we hypothesize that the vapor diffusion limit would have prevented the liquid from receding into the nanopores and forming evaporating menisci. When the liquid-vapor interface recedes inside the pores, the vapor generated at the interface from liquid phase has to exit the pores in order to enter the bulk vapor volume. As described in Ref. [167], the evaporation flux from each channel would be suppressed when the nanochannel was adjacent to other channels, indicating the vapor removal being the limit for evaporation. In our experimental configuration, the nanopores are closely packed with a pore-to-pore distance of ~100 nm, which is highly possible to induce a very large vapor advection/diffusion resistance to limit the evaporation heat flux. In our experiments, as the maximum evaporation heat flux limited by vapor diffusion was smaller than the maximum heat flux attainable in the thin-film boiling regime when liquid-layer-dryout heat flux, no thin film evaporation regime could be stably reached.

We noticed that in some of the experiments, instead of an instant sudden burn out of the sample beyond the CHF reported in the paper, a higher heat flux was dissipated for a period time. For example, one test with 760 torr liquid pressure (CHF ~700 W cm^{-2}) was able to maintain a heat flux of ~728 W cm^{-2} after the top dryout happened for over 100 seconds. This extra heat flux is indicative of the additional liquid mass flux generated from evaporation, when the liquid receded into the pores and induced a capillary driving force. However, although this heat flux was dissipated for a relatively long time, the wall superheat read from the resistance of the RTD was not stable and kept increasing with a rate of 0.055 °C sec^{-1}, and the sample broke soon after increasing the heat flux to 764 W cm^{-2}.

One possible reason for the unstable resistance is the formation of a local hotspot due to the non-uniform heating and the non-uniform pore size distribution of the membrane. The membrane has a wide pore size range which indicates that at CHF, some pores were still flooded while some pores already had receded liquid. At the portion (usually the center of the membrane) where heat flux is higher than the average, the smaller pores might already have long receding length of the interface, for which the vapor diffusion/advection resistance is significant and a local hotspot is likely to form which causes local degradation and eventually membrane failure. Additionally, the Pt layer was not very hydrophilic and could have limited the lateral liquid spreading when there was a local dryout or liquid receding into the pores. Another reason could be due to the pore clogging. Similar superheat increasing behavior was observed [68] and was attributed to the clogging of the pores by the accumulation of contaminants due to the increase of contaminant concentration caused by liquid evaporation. For the samples tested under

different pressure conditions, this superheat increase period ranges from several seconds to a few minutes before a hotspot form and sample burnout, which is possibly resulted from the variation of both the liquid contamination and the pore size distribution of the membranes.

Returning to our initial question regarding the upper limit of heat flux from a planar surface, it would be interesting to compare our results to the theoretical limit in phase change heat transfer. Although bubbles are present in the thin film boiling regime, the ultimate upper limit for the heat flux is essentially the same as the maximum interfacial heat flux on a planar surface, which is achieved when all of the molecules at the liquid-vapor interface would escape to the vapor phase with certain speed (usually considered on the order of the speed of sound [151, 168]) and without returning to the liquid, i.e., $q''_{max} = \rho_v c h_{fg}$ where c is the average vapor speed. However, this simple equation only accounts for the mass conservation, and does not represent the non-equilibrium behavior in the Knudsen layer during an intensive evaporation. Here we employed an approximate method from the Boltzmann transport equation with consideration of conservation of mass, momentum and energy to describe the interfacial flux of intensive evaporation [169]. The calculated interfacial flux for a liquid layer at 70 °C (corresponding to the superheat of 50 °C at the CHF condition in Figure 2.9) evaporating to the vapor space at 20 °C is close to 5 kW cm^{-2} (see Section 2.4.2). Our experimental CHF is only within a factor of 4 of this limit. Moreover, it should be noted that this CHF has so far *only* been limited by mechanical strength of the membrane. By increasing the pressure difference to provide larger liquid mass flux or by decreasing the membrane thickness to reduce the liquid flow resistance, higher CHF and HTC can be achieved. However, both of these approaches compromised

the mechanical strength of the devices and have led to fracturing of the membranes, as shown in Figure 2.13. Better membrane design with support structure or using other materials with better strength should be used for future pursuit of higher heat flux.

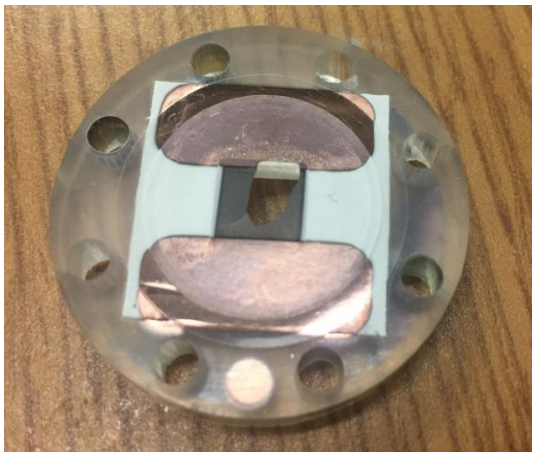

Figure 2.13: Picture of one sample cracked due to high liquid pressure.

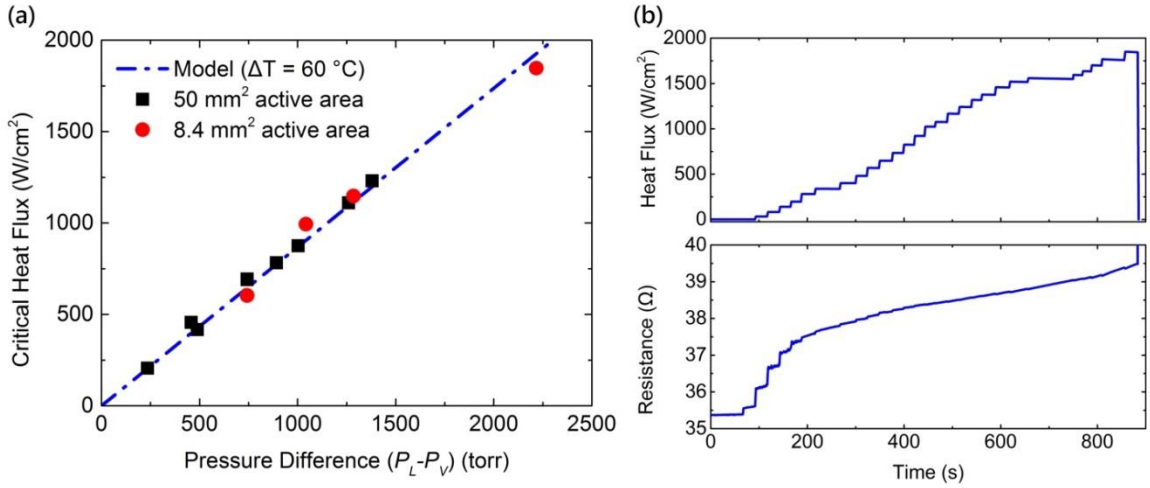

Figure 2.14: (a) CHF as a function of pressure difference of samples with both 50 mm^2 and 8.4 mm^2 active area. (b) Heat flux as a function of time and resistance as a function of time during experimental test with 8.4 mm^2 sample area and 2234 torr liquid pressure.

To demonstrate this feasibility, we designed new sample holders and deposition masks with defined opening area of 8.4 mm^2, and performed boiling experiments with higher liquid pressure, and the CHF results are shown in Figure 2.14 (a) along with the CHFs of 0.5 cm^2 samples.

The CHFs of the samples with 8.4 mm^2 active area shown in Figure 2.14 (a) follow the trend of the previous experiments and the model prediction, indicating that the heat transfer fundamentals remained the same after reducing the sample area -- the CHF is still limited by liquid transport. One important issue observed in these samples with small active area is the drift of the temperature reading. Even with zero heat flux, the resistance of the Pt RTD continues to increase for over 50 min when subjecting to 2150 torr pressure difference, which will give a temperature reading increase of ~60 °C. Both the heat flux and the resistance as a function of time during the test at 2234 torr liquid pressure with CHF of 1.85 W cm^{-2} are shown in Figure 2.14 (b), showing clear resistance drift during the entire experiment. The real sample temperature is thus difficult to obtain to produce a meaningful boiling curve. Since the experiments were conducted by applying the heat flux incrementally, the right-shift will be more significant at higher heat flux due to longer time of accumulated resistance drifting. This could possibly explain why the resistance of the sample at 2234 torr liquid pressure does not decrease at high heat flux, and therefore a monotonic boiling curve without inversion, if plotted.

Although the boiling curves of the samples with 8.4 mm^2 active area cannot be obtained to represent their real boiling behavior due to inaccurate temperature reading, the CHFs recorded here is still accurate enough to compare with the previous results. Notably, to our best knowledge, the heat flux achieved in the 8.4mm^2 heater size (1.85 kW cm^{-2}) is

the highest amongst all the phase change heat transfer experiments with heater area larger than 1 mm^2, even though the boiling only occurred on a planar surface in our experiments.

We note that the CHF vs. liquid pumping pressure ($P_L - P_V$) dependence is exactly the same between the two heater sizes (Figure 2.14 (a)), suggesting the same boiling heat transfer behaviors for the heater sizes ranging from 8.4 to 50 mm^2. This further indicates that our thin film boiling mechanism is scalable for different heater sizes due to the cross-plane liquid supply strategy, and larger heat flux can be achieved if mechanical strength of the membrane can be improved or the mechanical deformation can be reduced. Therefore, the idea presented in this work can be readily used with improved material mechanical property and structure design to achieve much higher heat flux dissipation.

2.5 Modeling and analysis

2.5.1 Theoretical CHF modeling

The Hagen-Poiseuille equation gives the pressure drop of fully developed laminar flow inside a circular tube to be $\frac{dP}{dx} = -\frac{128\mu Q}{\pi D^4}$ where D is the diameter of the tube and Q is the volumetric flux. For a non-circular tube, which is the case of the nanopores of AAO membranes used in the experiments (see Figure 2.2 (a) and Figure 2.3 (a)), the diameter can be replaced by the hydraulic diameter defined by $D_h = \frac{4A_p}{p}$ where A_p and p are the area and perimeter of the pores, respectively. The total mass flux is represented by $\dot{m}_{tot} = Q\rho_l \frac{A\eta}{A_p}$ which gives the theoretical maximum heat flux $q_t'' = \frac{{D_h}^2 \Delta P}{32\mu L}\rho_l(h_{fg} + c_p\Delta T)\eta$. In this equation, the water properties vary little with temperature except for the viscosity. We evaluate the liquid viscosity at $T_{ave} = 20\ ℃ + \Delta T/2$ in the above equation as the average

temperature of liquid flow inside the pore. Density and specific heat are also chosen at T_{ave} while the latent heat is chosen at T_h.

The calculated q_t'' curve with $\Delta T = 60\,°\mathrm{C}$ was in good agreement with the experimental CHFs. The recorded ΔT at CHF in the experiments were smaller, which is likely due to the non-uniformity of heat flux caused local high superheat (higher than global value recorded) since the dry out spot was often observed at the center of the membrane (see Figure 2.15).

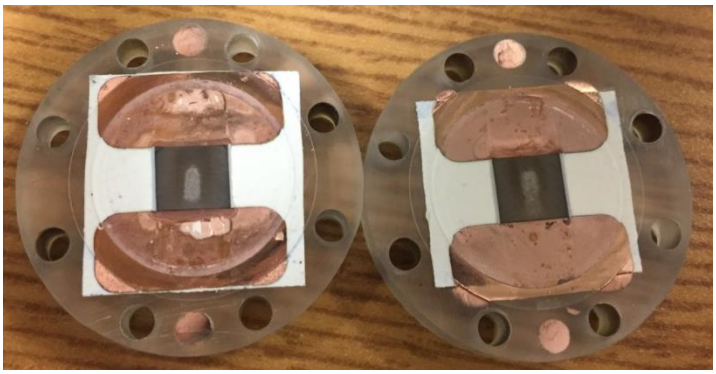

Figure 2.15: Samples used in the experiments after CHFs were reached. The dryout spots appeared on top of the membranes and gradually expanded, indicating a local high superheat at the center of the membranes.

2.5.2 Modeling of the upper limit of CHF

The upper limit of CHF is modeled with a one-dimensional evaporation configuration following Labuntsov and Kryukov [169]. The schematic of the configuration is shown in Figure 2.16.

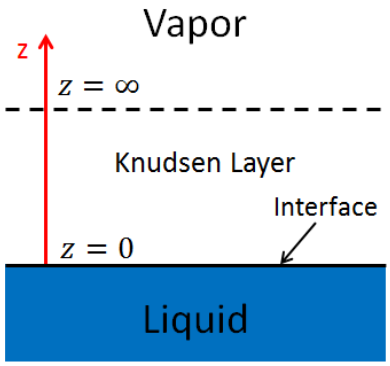

Figure 2.16: Schematic of the upper heat flux limit model.

The semi-infinite liquid space occupies the z<0 region with the liquid-vapor interface at coordinate z=0. The vapor evaporates from the interface and escapes at $z = \infty$, where the vapor velocity field is no longer dependent on the coordinate and is in equilibrium. The conservation equations of mass, momentum and energy of the vapor phase produce the following relations:

$$m \int \xi|_{z=0}\, u_z d^3\mathbf{u} = m \int \xi|_{z=\infty}\, u_z d^3\mathbf{u} \tag{2.2}$$

$$m \int \xi|_{z=0}\, {u_z}^2 d^3\mathbf{u} = m \int \xi|_{z=\infty} {u_z}^2\, d^3\mathbf{u} \tag{2.3}$$

$$m \int \xi|_{z=0}\, u_z \frac{\mathbf{u}^2}{2} d^3\mathbf{u} = m \int \xi|_{z=\infty}\, u_z \frac{\mathbf{u}^2}{2} d^3\mathbf{u} \tag{2.4}$$

where ξ is the velocity distribution function in the vapor space and m is the mass of a single molecule. The distribution function at $z = \infty$ (Euler equilibrium flow) is represented by

$$\xi|_{z=\infty} = \frac{n_\infty}{(2\pi R T_\infty)^{3/2}} \exp\left[-\frac{{u_x}^2 + {u_y}^2 + (u_z - u_\infty)^2}{2RT_\infty}\right] \tag{2.5}$$

where n_∞ is the number density of molecules, R is the gas constant, and T_∞ is the temperature at the equilibrium state. The distribution function at $z = 0$ is represented by

$$\xi|_{z=0,\,u_z<0} = \frac{Cn_\infty}{(2\pi RT_\infty)^{3/2}} \exp\left[-\frac{{u_x}^2 + {u_y}^2 + (u_z - u_\infty)^2}{2RT_\infty}\right] \tag{2.6}$$

$$\xi|_{z=0,\,u_z>0} = \frac{n_s}{(2\pi RT_s)^{3/2}} \exp\left[-\frac{{u_x}^2 + {u_y}^2 + {u_z}^2}{2RT_s}\right] \tag{2.7}$$

where C is a dimensionless constant to be solved, n_s is the number density of vapor molecules in equilibrium with the liquid at the interface, and T_s is the liquid temperature at the interface. Given T_∞, T_s and n_s, the unknown parameters C, n_∞, and u_∞ can be solved from the conservation equations and the resulting heat flux limit is

$$q_m'' = h_{fg}\dot{m} = h_{fg} m n_\infty u_\infty \tag{2.8}$$

Using the experimental condition of $T_\infty = 293.15$ K, $T_s = T_\infty + \Delta T = 343.15$ K, and assuming n_s is the saturation number density of molecules at T_s, the upper limit of heat flux is ~5 kW cm^{-2}. This result is within an order of magnitude difference with the experimental CHF. It is worth noting that this upper limit heat flux is highly sensitive to the superheat, and the upper limit will be higher for higher superheat.

2.5.3 Estimation of the liquid layer thickness

The liquid layer thickness at the transition from pool boiling to thin film boiling, i.e., the onset of thin film boiling, is estimated to be a few hundred μm from thermal boundary layer thickness estimation. The liquid layer thickness near CHFs can also be estimated roughly.

According to Tien [161], the thermal boundary layer (TBL) thickness of nucleate boiling can be estimated by $\delta_T = 3.22k/h_{boil}$ where k is the liquid thermal conductivity and h_{boil} is the boiling heat transfer coefficient. This indicates that the effective thermal conductivity of the liquid inside the TBL can be estimated by $k_{eff} = 3.22k$. By assuming

a constant effective thermal conductivity and apply the one-dimensional heat conduction equation, the liquid layer thickness calculated by $d = k_{eff}/(q''/\Delta T)$ at the CHFs ranges from 10~40 μm for different liquid pressure conditions presented later. Note that the effective thermal conductivity of the liquid layer could be larger with higher heat flux due to more significant bubble behavior and its induced convection, which will result in a thicker liquid layer. This length scale of tens of microns is also in agreement with the critical bubble radius [151] for water at 20 °C saturation temperature and 60 °C superheat (~16 μm), which indicates that when the liquid layer is thinner than this thickness, the bubble growth is not stable, which will result in the termination of the thin film boiling regime. Therefore, in this work, the liquid layer thickness is estimated to be ~10s μm near the CHF.

This range of liquid thickness for thin film boiling is generally larger than that in the thin film evaporation regime, which has been reported to be in the range of a few microns, as reported by several researchers [156, 170, 171]. In our work, boiling occurs inside the liquid layer which induces enhanced convection due to the bubble motion, and the resultant heat transfer could be more efficient even with a much thicker liquid film compared to the thin film evaporation regime.

2.6 Summary

In summary, we realized a new "*thin film boiling*" mechanism using nanoporous membranes to achieve the highest CHF of boiling heat transfer on a planar surface. By controlling liquid pressure while maintaining a constant vapor pressure, different mass flux across the membrane, and consequently different CHF values, can be provided. The

achieved highest CHF values were 1230 W cm^{-2} and 1850 W cm^{-2} on heater sizes of 50 and 8.4 mm^2, respectively. These CHF values are within a factor of four of the upper limit of CHF, and were only limited by the mechanical strength of the membrane. Increasing and eventually negative slopes were observed in the boiling curves due to the thin liquid film geometry. The enhanced boiling performance was attributed to the separate liquid-vapor pathways, the thin liquid layer promoted bubble departure, and the reduced conductive thermal resistance. This study also provides a new approach for achieving ultrahigh heat flux in boiling heat transfer for thermal management of high power devices.

Chapter 2, in full, is a reprint of the material as it appears in "Ultrahigh flux thin film boiling heat transfer through nanoporous membranes", *Nano Letters* 18.5 (2018): 3096-3103, by Qingyang Wang and Renkun Chen [172]. The dissertation author was the first author of this paper.

Chapter 3 Transition between thin film boiling and evaporation near the kinetic limit

3.1 Introduction

Nanoporous structures including single nanopores and nanoporous membranes have been utilized as a platform to study fundamental liquid-vapor phase change heat transfer (PCHT) processes as well as a promising candidate for high flux heat dissipation. Previously, we implemented nanoporous membranes to support a thin liquid film for boiling, which was termed "thin film boiling", and realized high heat transfer performance as shown in Chapters 2. Besides thin film boiling, thin film evaporation through nanoporous structures have also been demonstrated to achieve high heat flux as discussed in Chapter 1, but these two mechanisms are usually considered two mutually exclusive regimes operated under vastly different conditions, and the factors dictating how close the PCHT process is to the kinetic limit are elusive.

To achieve high heat flux PCHT, the theoretical limit of the phase change process is considered to be the kinetic limit, which, according to the Hertz-Knudsen (HK) or Schrage formula, essentially relates the maximum vapor mass flux leaving the liquid-vapor interface to the speed of sound. Recent work by Lu et al. [173] and Li et al. [174] showed evaporation near the kinetic limit in nanoporous membranes and single pores, respectively, thus suggesting the prospect of achieving high CHF and high HTC. Nevertheless, the near kinetic limit processes were only observed with low vapor pressure (or low Mach number),

thus the attained vapor velocity and eventually the heat flux were not very high, about 340 W cm^{-2} in Lu et al. [173] and 294 W cm^{-2} in Li e al. [174].

This leads us to ask whether or not the near kinetic limit behavior can be universally observed, for example, across different fluids and more importantly, feasible under conditions with larger vapor pressure or Mach number that would result in higher absolute heat flux. Answering these questions would help us better understand and eventually mitigate the factors preventing the PCHT processes from reaching the theoretical limit. In this study, we systematically controlled the experimental conditions such that the PCHT can be tuned to be close to or far away from the kinetic limit. This level of control was achieved by leveraging the concept of "thin film boiling" on nanoporous membranes recently demonstrated by us, which showed high CHF and HTC for boiling due to the small liquid thickness. In this thin film boiling regime, liquid flows through the membrane and forms a thin liquid film for boiling, as shown in Figure 3.1 (a). Both the bubble growth and departure are more efficient compared with boiling from a thick liquid pool due to the small thickness of the liquid film. Meanwhile, liquid supply through the porous membrane provides separated liquid-vapor pathways for enhanced liquid rewetting. Therefore, thin film boiling resulted in a significant heat transfer enhancement compared with pool boiling.

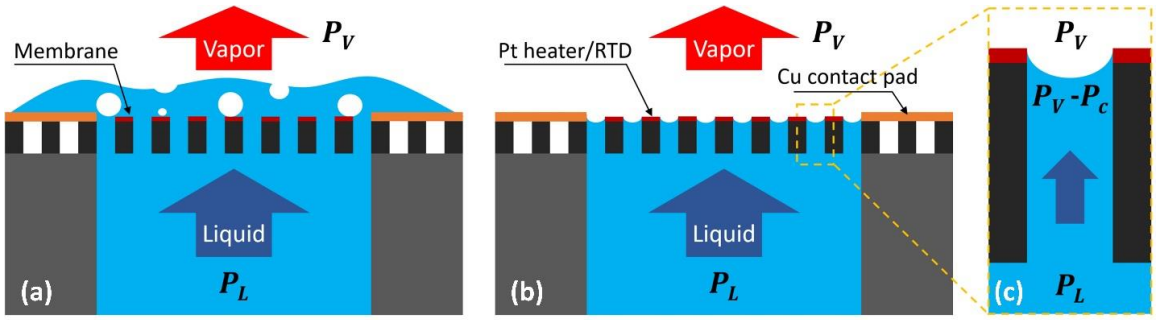

Figure 3.1: Schematic illustrations showing (a) thin film boiling, where bubbles are generated on top of the heated nanoporous membranes, (b) pore-level thin film evaporation when the liquid is receded into the pores, and (c) zoom-in schematic of a single pore from (b) showing the capillary pressure aided liquid supply.

In the thin film boiling configuration, the liquid floods atop the membrane so there is no capillary force from the nanopores in the membrane. As such, the liquid supply through the membrane is driven by the pressure difference across the membrane, and the flow rate associated with this liquid supply governs the maximum heat flux in this regime, as we observed previously in water (Chapter 2). By comparing the work between evaporation studied by Wang and coworkers [63, 67] and thin film boiling by us on nanoporous membranes, as well as recent work on evaporation from nanochannels and nanopores by Duan and coworkers [167, 174], it is evident that both heat transfer mechanisms could take place on nanoporous structures. However, it remains unclear what are the conditions leading to boiling or evaporation and if a transition between these two regimes is possible. We note that as the liquid on top of the membrane is dried out, it could recede into the nanopores and form liquid-vapor menisci, as shown in Figure 3.1 (b,c). If this occurs, the capillary pressure inside the pores can provide extra liquid flow rate, exceeding the amount driven by the external liquid pumping pressure.

In this work, we found that the thin film boiling phenomena are universally observed on multiple fluids with vastly different surface tension values, including water, ethanol, isopropyl alcohol (IPA), and perfluorohexane (FC-72). More importantly, for these fluids, upon further increase of the heat flux, the thin film boiling regime was transitioned to the capillary-driven pore-level evaporation regime when the liquid layer on top of the membrane was depleted by the high heat flux. The heat flux and HTC at the transition points were close to those of the kinetic limit owing to the unique configuration of our experiment which renders the interfacial resistance being the dominant resistance. However, further increase of the heat flux beyond the transition points led to decreasing HTC and deviation from the kinetic limit, which can be attributed to the increasing vapor resistance in the vapor space and inside the nanopores. This increasing vapor resistance was also confirmed by experiments on IPA with different vapor pressures. Our work could lead to a better understanding of the underlying mechanisms of PCHT on nanoporous structures and will benefit the applications such as the design of high heat flux heat sink and thermal devices for thermal management and thermal regulation.

3.2 Experimental

3.2.1 Sample preparation and experimental procedure

The sample preparation and experimental procedure used in this work is the same as presented in Chapter 2, Section 2.3. We used nanoporous anodized aluminum oxide (AAO) (Whatman 6809-6022) as the nanoporous membrane. The membrane was epoxy-bonded onto an acrylic sample holder with a 0.71×0.71 cm^2 (0.5 cm^2 area) hole for liquid flow. A thin Pt film (~70 nm) was deposited on the membrane using magnetron sputtering

to serve as the heater and resistance temperature detector simultaneously. In the current work, we implemented a much thinner shadow mask compared to our previous work (Chapter 2) for Pt deposition, which resulted in a more uniform thickness of the Pt layer to reduce the non-uniformity of heating. Two thick Cu contact pads (~2 μm in thickness) were also deposited to allow electrical connection. A 10 nm thick Cr layer was deposited and served as adhesion layer before both the Pt and Cu deposition processes. The size and location of the Pt heater matches the square opening on the sample holder, such that the area with liquid flow matches the area for the heat flux supply. Four different fluids were used in the experiments: water, ethanol, IPA, and FC-72. De-ionized (DI) water was obtained from a laboratory Milli-Q system. Ethanol (Koptec Pure Ethanol 200 Proof), IPA (ThermoFisher Scientific, HPLC Grade, purity ≥99.9%), and FC-72 (3M Fluorinert) were procured from various vendors. Before experiments, the liquid was first degassed by vigorous boiling inside a liquid reservoir at 2.3, 5.9, 4.4, and 25.2 kPa for water, ethanol, IPA, and FC-72, respectively (the saturation pressure of 20 °C for respective fluid) for a few minutes before each experiment.

3.2.2 Reversibility test

For reversibility demonstration, one sample was tested with the previously mentioned procedure using ethanol, except with two cycles of increasing and decreasing of the heat flux, at 101.3 kPa (760 Torr) liquid pressure condition to show the reversibility of the heat transfer regimes. The heat flux applied to the sample was first increased to 138.32 W cm^{-2} and then decreased to zero. After the first run, the heat flux was again incrementally applied up to 193.8 W cm^{-2} and then decreased to zero again, completing a

second test run for the reversibility test. The heat flux was finally increased from zero up to CHF of 219.36 W cm^{-2}, after which the sample burned out and broke.

3.2.3 Tunability tests

The dynamic tunability tests were performed using ethanol as the working fluid, by changing the liquid pressure while varying the heat flux, with the vapor side pressure maintained at 5.9 kPa (44.4 Torr) for all the tests. The tunability test 1 demonstrates the tunability between transition points of different liquid pressures. The liquid pressure was modulated with the change of applied heat flux so that the heat flux was equal to the transition heat flux (which is the heat flux at the lowest superheat point, obtained from the heat flux-superheat curve, as defined later in Section 3.3 later) at that liquid pressure. The tunability test 2 demonstrates the ability to maintain the wall superheat with varying heat flux. The tunability test 3 demonstrates the ability to modulate the wall superheat at a constant heat flux. The tunability test 4 demonstrates the modulation of conductance from the lowest to the highest. All of these tests were achieved by changing the liquid pressure and heat flux at the same time so that a certain working condition was reached. Each test was performed with liquid pressure change for at least one increasing-decreasing cycle.

3.3 PCHT experiments and heat transfer curves

We tested the heat transfer using four fluids at various liquid pressures and a fixed vapor pressure for each fluid. Figure 3.2 shows the heat transfer curves of four different working fluids: water, ethanol, IPA, and FC-72. For the curves shown in Figure 3.2, the vapor pressure P_V for water, ethanol, IPA, and FC-72 were fixed at 2.3, 5.9, 4.4, and 25.2

kPa, respectively. These pressures are the saturation pressures of 20 °C vapor for the respective fluid types. The liquid pressure P_L was varied for each fluid.

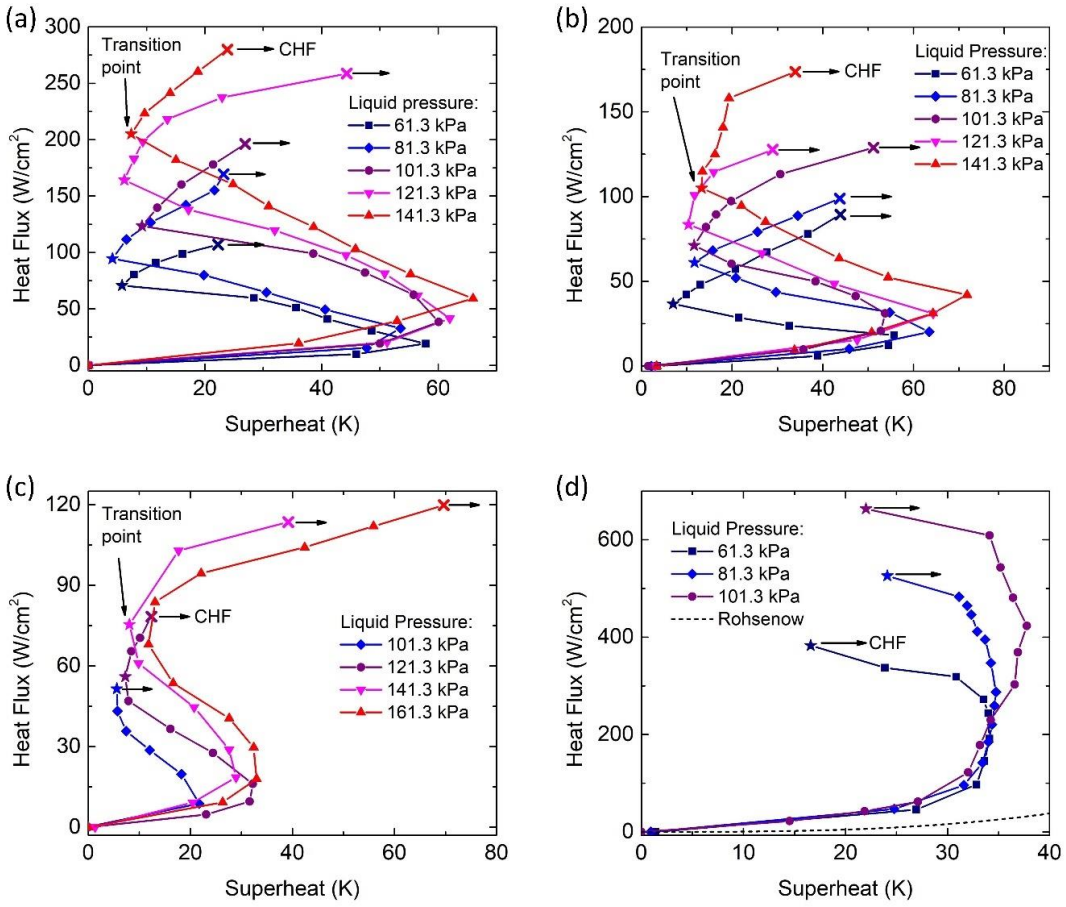

Figure 3.2: Heat transfer curves for (a) ethanol, (b) IPA, (c) FC-72, and (d) water at 20 °C saturated vapor with varying liquid pressures. The vapor pressure for water, ethanol, IPA, and FC-72 were fixed at 2.3, 5.9, 4.4, and 25.2 kPa, respectively. The "transition points" indicate the transition from thin film boiling to thin film evaporation, represented by the stars. Beyond these transition points, there are thin film evaporation regimes in ethanol, IPA, and FC-72, but not in water. The Rohsenow correlation for nucleate boiling under the experimental condition is also plotted in (d), showing that the small slope portion of the curves are close to the Rohsenow model prediction.

It can be seen from Figure 3.2 that for all of the fluids tested in this work, the curves display a small-slope regime at low heat fluxes, which represents the well-known pool

boiling regime, as shown previously in Chapter 2. This is because at low heat fluxes, the liquid flow across the membrane driven by the pressure difference ($P_L - P_V$) was much larger than the vaporization flux, which resulted in a thick liquid puddle on top of the membrane and led to heat transfer behavior similar to pool boiling. When the liquid film is much thicker than the thermal boundary layer thickness, which is tens to a few hundred μm for these fluids using the scaling analysis (Section 2.4.3), the boiling lies in the pool boiling regime, where the bubble departure diameter is ~mm and the bubble behavior is similar to pool boiling, as described in previous chapters. The bubble formation also indicates that the beginning of the curves with small (positive) slopes are already in the nucleate boiling regime instead of natural convection.

It is worth mentioning that due to the more uniform thickness of the deposited Pt layer (as described in Section 3.2), we obtained higher heat flux and HTC in the pool boiling regime than those obtained in Chapter 2 for the same fluid (i.e., water). The heat transfer curves are still largely following the trend predicted by the Rohenow correlation as shown in Figure 3.2 (d), but with higher HTC, which can be attributed to the finite thickness of the liquid film as well as the nanoporous morphology of the membrane that could possibly offer more nucleate sites [22, 37].

As the heat flux increases, the slope of the curves becomes negative, which is what we referred to as the "thin film boiling" regime. In this regime, the increase of heat flux caused the reduction of the liquid layer thickness on top of the membrane, which led to a smaller thermal resistance for bubble growth and smaller bubble departure diameter, and consequently the decrease of superheat. This regime gave rise to the interesting negative slopes in the boiling curves, as shown in all the four fluids in Figure 3.2. It is worth

mentioning that negative slopes in boiling curves have been reported before for pool boiling [22, 175], which were attributed to the activation of small nucleation sites and thus exhibited hysteresis when increasing and decreasing the heat flux. On the contrary, in this thin film boiling regime, the negative slope was fully reversible and showed no hysteresis since it was caused by the liquid layer thickness change, as will be discussed below in Section 3.5. In this regime, as the liquid layer thickness decreased, the bubble size also reduced to tens to a few hundred μm.

Different trends can be observed between the curves for water and the curves for other fluids at the end of the thin film boiling regime. In the case for water, after the termination of the negative slope portion, the curves ended, and no higher heat flux was achieved in the experiments. On the other hand, in the curves for low surface tension fluids, another portion with a positive slope emerged. The extra positive slope in the curves for low surface tension fluids represented the pore-level thin film evaporation regime, and the point where the slope of the curve turned from negative to positive was considered the "transition point", namely, indicating the transition from thin film boiling to pore-level evaporation. When the vaporization flux is balanced by the maximum liquid flux that can be provided by the pressure difference ($P_L - P_V$) across the membrane, liquid layer on top of the membrane would dry out, which occurred at the transition points. Any further increase of the heat flux would cause the liquid-vapor interface to recede inside the pores and generate capillary pressure for sustaining the higher liquid flux until the eventual CHF was reached. In this capillary-aided evaporation regime, as more vapor needs to be removed from the interface with increasing heat flux, the vapor removal resistance becomes increasingly dominant, resulting in the positive slope, as will be discussed in

Sections 3.7.2 and 3.7.3. The absence of this pore-level evaporation regime in the water experiments will be discussed in Section 3.4.

3.4 Comparison between ethanol and water experiments

Different heat transfer characteristics have been observed for water and other fluids as shown in Figure 3.2. In this section, we discuss the differences by taking ethanol as an example for low surface tension fluids, and compare the results of ethanol and those of water.

3.4.1 Contact angle difference

The Pt layer deposited on top of the nanoporous membrane is the heating surface of boiling process, and the contact angle of liquid on this layer dictates important boiling dynamics and the difference of contact angle for different liquids can be used to explain the differences between the heat transfer curves of them.

To verify the discussions above, contact angle measurement were conducted for water and ethanol on the nanoporous membrane as shown in Figure 3.3, where (a) and (c) shows the tilted view of Pt surface after placing the liquid droplet on top, and (b) and (d) shows the contact angle measurement. The contact angle on the nanoporous Pt layer is ~60° for water and ~0° for ethanol.

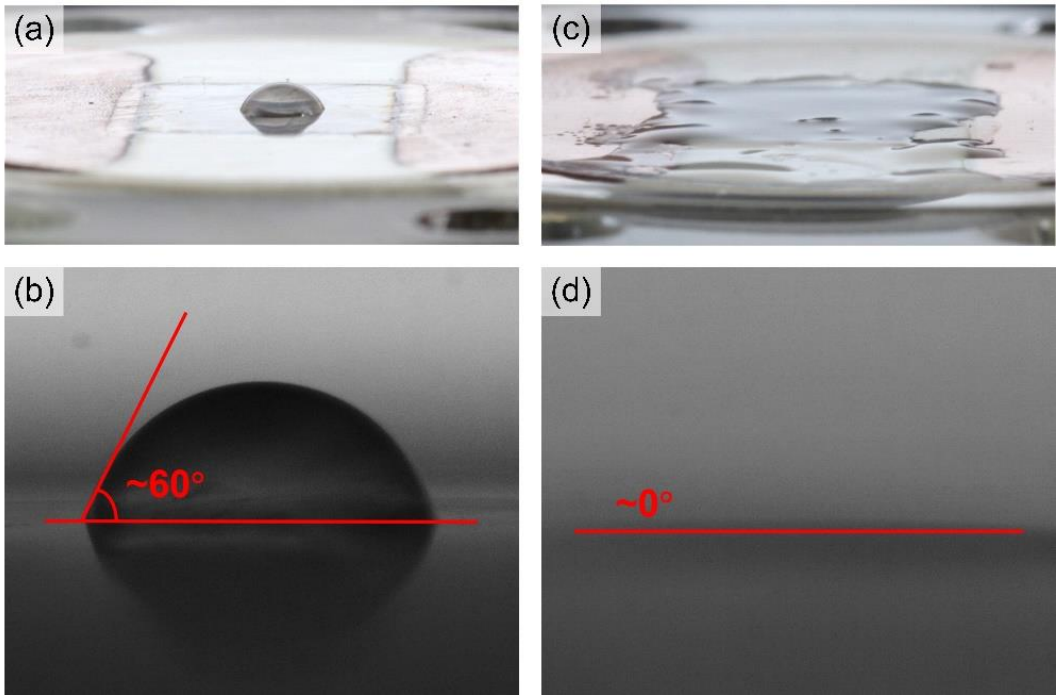

Figure 3.3: Contact angle measurement of (a,b) water and (c,d) ethanol on the Pt heater on top of the nanoporous membrane. The contact angle is ~60° for water and ~0° for ethanol.

Therefore, the absence of the pore-level evaporation regime in the water experiments was probably caused by the poor wettability of water on the heater surface, such that any local dry-out spots cannot be quickly replenished by lateral spreading of water on the heater surface. When the thin film boiling regime ended (marked by the stars in Figure 3.2, including the transition points in Figure 3.2 (a-c) and CHFs in Figure 3.2 (d)), the non-uniform heating from the Pt film would inevitably cause some local spots having larger heat fluxes relative to the rest area of the heater, for example, due to variations in the pore size and the Pt film thickness. These hot spots could cause pre-mature CHF before the evaporation regime was established in water. On the contrary, this pre-mature failure caused by local hot spots can be prevented for low surface tension liquids due to their better lateral liquid spreading capability. The liquid spreading due to the wetting of

liquid on the membranes can help dissipate higher heat flux [174] and mitigate the hotspots, thus enabling the formation of stable pore-level evaporation regime.

3.4.2 Different range of negative slope

In Chapter 2, thin film boiling of water was reported and negative slope at high heat fluxes in the boiling curves were observed. Compared with the results of thin film boiling of ethanol, the negative slope portion, i.e., the negative slope part of the curve in water experiments in Chapter 1 is narrower (with a smaller temperature range), as shown in Figure 3.2. The reason for a wider range of negative slope in ethanol compared with water is due to the different thermophysical properties between these two fluids, which resulted in very different superheats when the thin film boiling regime ended.

When the thin film boiling regime ended, the superheat was largely dependent on thermal resistance of the liquid layer, or layer thickness divided by the effective thermal conductivity of the liquid and bubbles. We can estimate this liquid film thickness using the two methods reported in Chapter 2. The effective thermal conductivity of the liquid film during boiling can be estimated by $k_{eff} = 3.22k$ and the liquid film thickness can be then estimated as $d = k_{eff}/(q''/\Delta T)$, which gives a liquid film thickness of 1~5 μm at the transition points. We can also assume the liquid film thickness is close to the critical bubble radius, which is given by,

$$r = \frac{2\gamma T_{sat}}{\rho_v h_{fg}(T_L - T_{sat})} \tag{3.1}$$

and is estimated to be ~7 μm for ethanol at 20 °C saturation temperature and 10 °C superheat representing the point before transition (because the transition points already represent pore-level evaporation regime as can be seen later in Figure 3.7 (c) and (f)).

Therefore, the liquid film thickness at the final stage of the thin film boiling regime in ethanol experiments is ~10 times smaller than the thickness estimated for water in our previous experiments (~tens of microns). Ethanol has only ~3x lower thermal conductivity than water (0.166 W m^{-1} K^{-1} vs. 0.598 W m^{-1} K^{-1} at 20 °C), so we expect ~3x smaller conduction resistance across the ethanol liquid film at the end of the thin film boiling regime compared to that of water. This lower thermal resistance contributed to the lower superheat. The experiments in ethanol also had about 5x smaller heat flux than water, which also led to a smaller superheat (superheat = heat flux × thermal resistance).

Another reason for the lower superheat with ethanol could be the smaller vapor coverage on the heater area. In the thin film boiling regime, bubble diameter is on the same order with the liquid layer thickness, so the smaller liquid thickness for ethanol than for water indicates a smaller bubble diameter in experiments with ethanol than with water. During boiling, liquid with a larger contact angle on the solid surface will have bubbles with larger pinning area on the solid surface; consequently, with similar liquid layer thickness, the bubbles in water will cover a larger area on the heated surface than the bubbles in ethanol, as shown in Figure 3.4. Therefore, in our previous experiments using water as the working fluid, a large portion of the heated surface is covered by vapor at high heat fluxes due to large bubble size (due to thicker liquid film) and large bubble base area, resulting in a higher superheat; while in our current work using ethanol, vapor occupies less fraction of the surface due to smaller bubble size and smaller bubble base area, and liquid rewets the bubble base more efficiently, which results in a lower superheat.

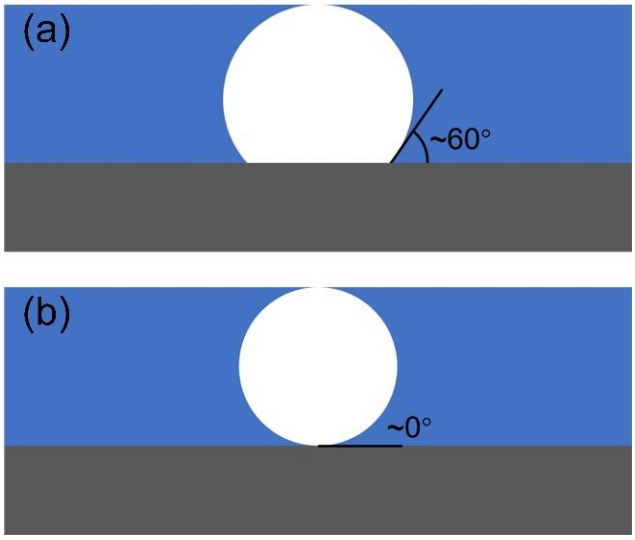

Figure 3.4: Different vapor coverage of the bottom surface with different wetting property of the liquids. (a) Water with ~60° contact angle having a large bubble base area; (b) ethanol with ~0° contact angle having very small bubble base area.

The lower superheat at the termination of thin film boiling regime during experiments with ethanol gives a more drastic negative slope in the boiling curves compared with experiments with water, and therefore a wider range of negative slope portion is observed.

It is worth mentioning that the superheat observed at low heat fluxes is several times higher than what has been observed in a recent work on liquid film boiling [62]. This can be explained by the differences in the conductive thermal resistance of the liquid film. In Wen, et al. [62], the copper mesh structure is surrounded by the boiling liquid film. Due to the high thermal conductivity of the copper mesh, heat transfer inside the mesh is much more efficient than through the liquid film, i.e., the liquid film has a high effective thermal conductivity and small conductive thermal resistance, and consequently the boiling surface has a low superheat. In our current thin film boiling configuration, at low heat fluxes, the liquid forms thick film on top of the nanoporous membrane, a large conductive resistance

due to the low thermal conductivity of the liquid causes a relatively higher superheat. Nevertheless, the superheat range of ethanol curves is similar to pool boiling experiments of ethanol at similar subatmospheric pressures [176], which is reasonable since the heat transfer regime at low heat fluxes is pool-boiling-like. Furthermore, this large superheat at low heat flux can also be reduced. In Figure 3.8 (a), we showed that superheat can be reduced even for lower superheat if we actively reduced the liquid pumping pressure to reduce the liquid film thickness (tunability test 1 in Figure 3.8 (a)). This can be combined with Wen, et al.'s idea [62] to further reduce the superheat, i.e., embedding metal structures inside the liquid film to reduce the superheat.

3.4.3 Transition from thin film boiling to pore-level evaporation

The heat transfer curves of our current ethanol experiments showed transition points at relatively high heat fluxes, where the curve changed from negative slope to positive slope again. We believe this transition represents the heat transfer regime transition from thin film boiling to thin film evaporation inside pores. When all the liquid mass flux driven by the pressure difference across the porous membrane (P_L-P_V) is vaporized, the top surface of the membrane will dry out, and the liquid-vapor interface will recede inside the pores, form menisci, and generate high capillary pressure which will provide extra driving force for liquid transport. The observed heat fluxes at the second transition points in ethanol were well correlated with the mass fluxes expected from the external liquid pumping pressure (as will be discussed later), i.e., the Hagen-Poiseuille equation. This suggests that additional heat fluxes beyond these transition points were driven by the capillary pumping effect when the liquid receded into the nanopores.

In the heat transfer curves of water, there is no second transition from thin film boiling to pore-level evaporation corresponding to the transition from negative slope to positive slope again. However, this second transition was in fact observed, but not stable. During the experiments with water, after the top of the membrane dries out which represents the end of the thin film boiling regime, the superheat was kept increasing slowly with a fixed heat flux. We attribute this phenomenon to the non-uniform heating of the membrane due to non-uniform Pt layer deposition. In that case, after the top surface dries out, some local area with higher-than-average heat flux would already have receded meniscus inside the pores [65], resulting in an extra resistance for vapor removal from the interface deep inside the pores, and consequently a local hotspot is likely to form which causes local degradation and eventually membrane failure. In ethanol experiments, stable pore-level evaporation was observed, possibly due to the better wettability of ethanol on the Pt layer. Since the pore diameters are not uniform (as shown in Figure 2.2), after this second transition when pore-level evaporation becomes the dominant heat transfer mode, the pores with larger diameter will still be flooded, i.e., the mass flux driven by pressure difference is larger than the local vaporization flux. These flooded pores supply extra liquid on top of the membrane, and due to the highly wetting surface property, the extra liquid can efficiently spread over the surface and compensate the area where either the local heat flux is higher or pores have smaller diameter, and the liquid-vapor interface already recede deep inside the pores. Therefore, the wettability of ethanol can effectively suppress the formation of local hotspot, eliminate the premature CHF caused by possible hotspot and stabilize the pore-level evaporation regime.

3.5 Reversibility and tunability

The negative slope of heat transfer curves has also been observed previously in boiling experiments, and most of them are associated with the activation of smaller nucleation sites at higher heat flux [22, 175]. Therefore, the negative slope is usually irreversible, meaning that there will be hysteresis when the sample goes through a thermal cycle. However, the negative slope in this work is caused by the unique thin film boiling configuration, where increasing heat flux leads to smaller liquid layer thickness and consequently lower thermal resistance. Due to the reversibility of the liquid layer thickness change, the heat transfer curve should also be reversible. Moreover, the reversible feature could enable a unique ability to control the thermal conductance of heat transfer by controlling the liquid film thickness, as schematically shown in Figure 3.5. In this section, we demonstrate the reversibility and tunability of the curves using ethanol as an example.

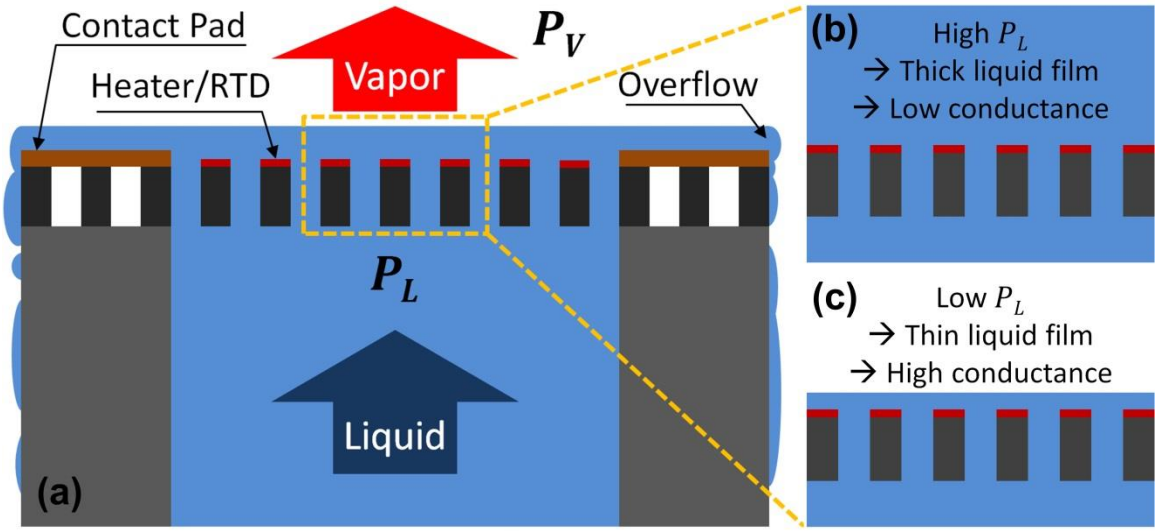

Figure 3.5: Schematic of the modulation concept. (a) Schematic of the nanoporous membrane configuration. The pressure difference between liquid pressure (P_L) and vapor pressure (P_V) drives liquid across the membrane. Heat flux applied to the heater is dissipated by vaporization of liquid on top of the membrane, and the rest of the liquid overflows. (b,c) Schematics of operation conditions with (b) high and (c) low P_L. Higher P_L provides higher liquid mass flux across the membrane, and therefore a thicker liquid layer and lower thermal conductance.

We tested the reversibility of the negative slope in the thin film boiling curves using ethanol, as shown in Figure 3.6. The sample was tested at 101.3 kPa liquid pressure (P_L), with two thermal cycles of increasing and decreasing the heat flux. Both cycles went through the upper heat flux higher than the transition heat flux, thus covering the entire negative slope regime. In the third and final run, the heat flux was increased until reaching the CHF. The five curves in Figure 3.6, each representing one increasing or decreasing run, show exact the same shape and overlap on each other, demonstrating the reversibility of the heat transfer behaviors, including within the negative slope regime.

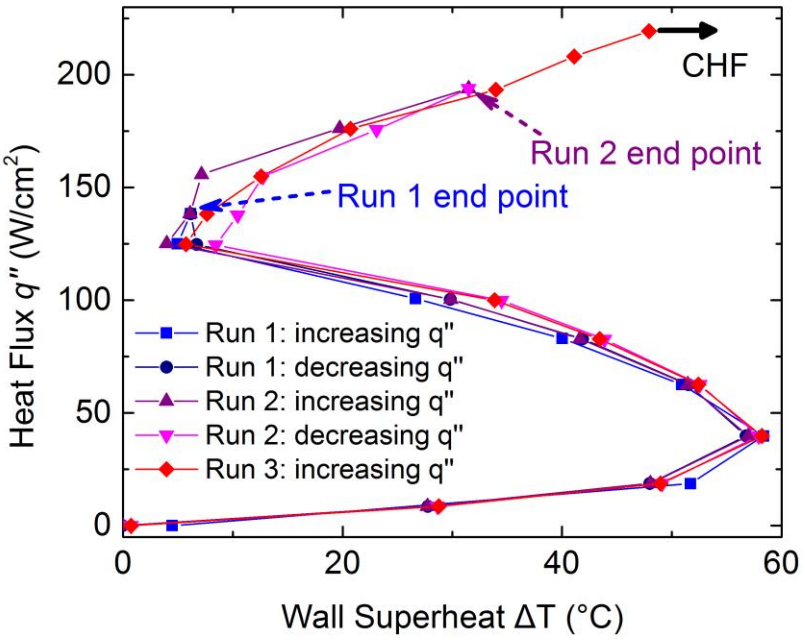

Figure 3.6: Heat flux as a function of wall superheat during the reversibility test with liquid pressure P_L=101.3 kPa.

Figure 3.7 shows the high-speed images of the sample surface during heat transfer experiments using ethanol. Figure 3.7 a-c and d-f confirm that the bubbles became smaller as heat flux increases with fixed liquid pressure, consistent with our previous explanation in Chapter 2 which attributes the lower thermal resistance to the smaller bubble size and higher bubble departure frequency. Moreover, the high-speed images in Figure 3.7 also show that with different liquid pressure, the same boiling heat transfer phenomena can be maintained under different heat fluxes. For example, mm-sized bubbles were observed both at $q'' = 19.3\ \mathrm{W\ cm^{-2}}$, $P_L = 760$ Torr (Figure 3.7 (a)) and at $q'' = 14.4\ \mathrm{W\ cm^{-2}}$, $P_L = 610$ Torr (Figure 3.7 (d)), while bubbles of ~100 um were observed both at $q'' = 99.0\ \mathrm{W\ cm^{-2}}$, $P_L = 760$ Torr (Figure 3.7 (b)) and at $q'' = 78.6\ \mathrm{W\ cm^{-2}}$, $P_L = 610$ Torr (Figure 3.7 (e)). Therefore, the heat transfer modulation can be realized by actively changing the liquid pressure. Given the reversibility of the heat transfer curves, we

performed four tunability tests demonstrating the ability for various types of thermal switches with wide modulation range of thermal conductance, heat flux, and superheat.

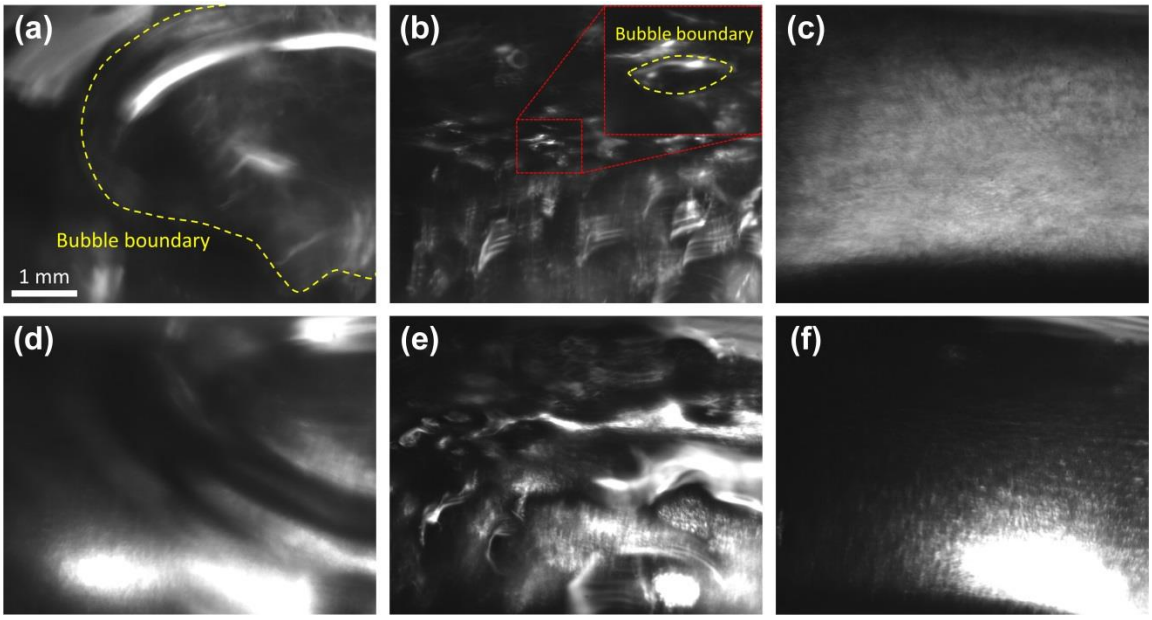

Figure 3.7: High speed images of the heated surface at different heat fluxes during the experiments with 760 Torr (a-c) and 610 Torr (d-f) liquid pressure. At 760 Torr liquid pressure: (a) 19.3 W cm^{-2}; (b) 99.0 W cm^{-2}; (c) 123.5 W cm^{-2}. At 610 Torr liquid pressure: (d) 14.4 W cm^{-2}; (e) 78.6 W cm^{-2}; (f) 107.4 W cm^{-2}. At each liquid pressure, the bubble size decreases as the heat flux increases (a,b and d,e) until a dry top surface appeared at transition points (c and f). Similar heat transfer behaviors appeared at different heat fluxes under different liquid pressures, as shown in (a) & (d), (b) & (e), and (c) & (f).

The tunability tests results are shown as colored curves in Figure 3.8 (a). The heat transfer characteristic curves at different liquid pressures ranging from 460 to 1060 Torr are also shown as gray curves in Figure 3.8 (a), which are the same curves shown in Figure 3.2 (a) but truncated at the transition points. The symbols in the curves for each tunability test represent the liquid pressures shown in the legend.

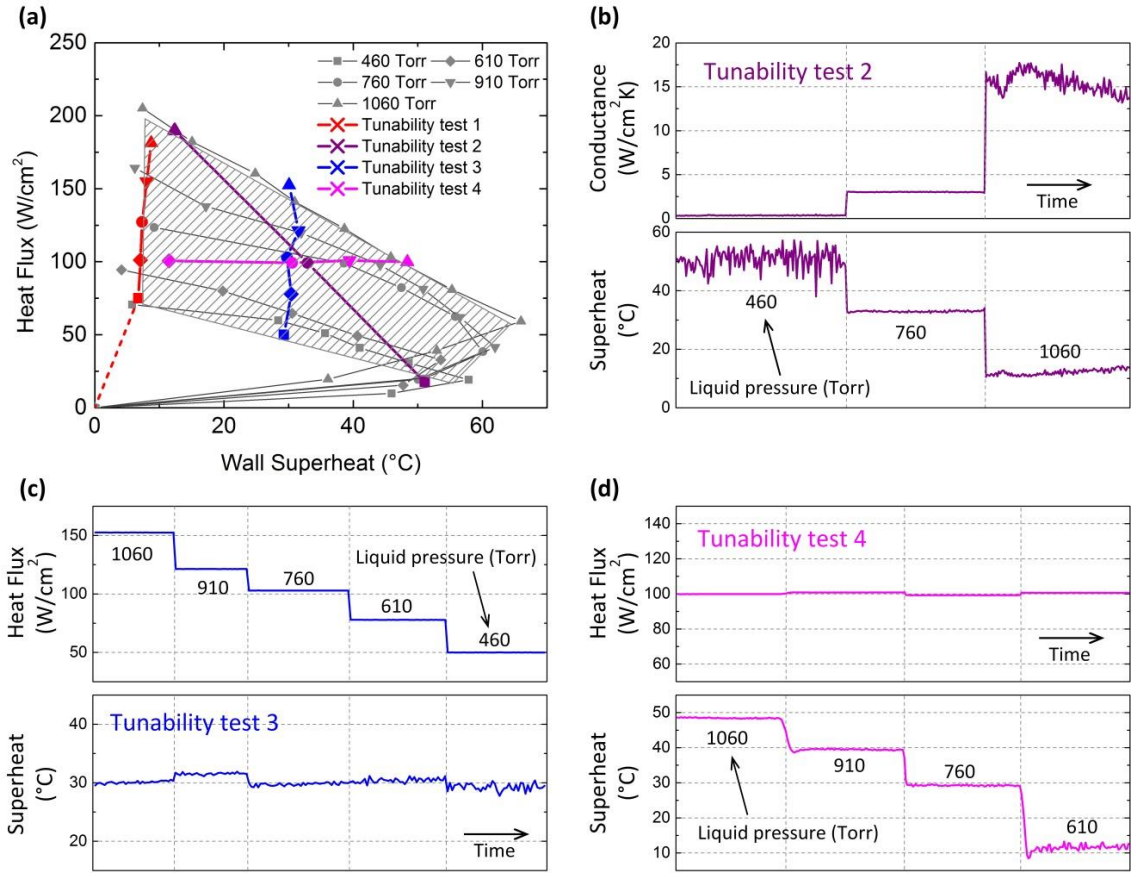

Figure 3.8: Working map of the tunable thermal switch and tunability demonstration by three tests. (a) Working map for the tunable thermal switch. The shaded area represents the attainable working regimes from the thin film boiling configuration. The gray curves represent the original boiling curves under various liquid pressures as in Figure 3.2 (a), shown up to the transition points, and the colored curves represent the various tunability tests: test 1 results in the lowest wall superheat at each applied heat flux (q'') by tuning the applied liquid pressure (P_L), leading to an effective boiling curve with high heat flux and low superheat, while tests 2-4 show the tunable conductance, heat flux, and wall superheat, respectively. (b) Tunability test 2 (purple curve in (a)) showing the modulation from the lowest conductance to the highest conductance by tuning both the liquid pressure (P_L) and heat flux. (c) Tunability test 3 (blue curve in (a)) showing the modulation of heat flux between 50 and ~150 W cm^{-2} at a fixed wall superheat of 30 °C by tuning P_L. (d) Tunability test 4 (magenta curve in (a)) showing the modulation of wall superheat between 10 and ~50 °C at a fixed heat flux of 100 W cm^{-2} by tuning P_L.

Tunability test 1, as shown by the red curve in Figure 3.8 (a), demonstrates that the transition points under different liquid pressure conditions can be achieved on one sample,

indicating the ability of achieving an effective boiling curve with high heat flux and low superheat for the entire heat flux range by simply adjusting the liquid pressure. This effective boiling curve is highly desirable for cooling of high flux devices with small superheat, and its heat flux and the thermal conductance outperform those using nanostructured superhydrophilic surface [22] and even the superbiphilic surfaces, which was designed to achieve low superheat at high flux [152].

The results of the tunability tests 2, 3, and 4 are shown in Figures 3.8 (b), (c), and (d), respectively. Tunability test 2 (purple curve in Figure 3.8 (a)) demonstrated the ability to modulate the thermal conductance by over 60 times, from ~0.3 W cm^{-2} K^{-1} to ~18 W cm^{-2} K^{-1} during thin film boiling by modulating the heat flux and liquid pressure, as shown in Figure 3.8 (b). Figure 3.8 (c) displays the tunability test 3 (also the blue curve in Figure 3.8 (a)), showing tunable heat flux from 50 to 150 W cm^{-2} with a fixed wall superheat of ~30 °C, while the tunability test 4 (Figure 3.8 (c) and the magenta curve in Figure 3.8 (a)) shows a large tunable superheat between 10 and ~50 °C under the same heat flux of 100 W cm^{-2}. These tests clearly demonstrated the abilities to maintain the same superheat with varying heat flux and to stabilize the same heat flux at different wall superheats. These unusual heat transfer characteristics are enabled by the unique negative slope regimes exhibited in the thin film boiling phenomena.

3.6 Modeling and analysis

3.6.1 Fluid temperature inside the membrane

Since the sensible heat $c_p(T_s - T_L)$ of the liquid under the experimental conditions is at least an order of magnitude smaller than the latent heat h_{fg}, the Reynolds number of liquid flow inside the pore can be roughly estimated by

$$\mathrm{Re}_{D_h} = \frac{q'' D_h}{\eta \mu h_{fg}} \tag{3.2}$$

where μ is the viscosity of the fluid, η is the membrane porosity, q'' is the applied heat flux, and D_h is the hydraulic diameter of the nanopores, as similarly defined in Eq. (3.4) later. Under the experimental conditions, the calculated Reynolds number is on the order of 10^{-3} or smaller, which indicates that the convective heat transfer of liquid flow inside the pores can be negligible and the heat transfer across the membrane can be considered as pure conduction. The thermal resistance network is shown in Figure 3.9.

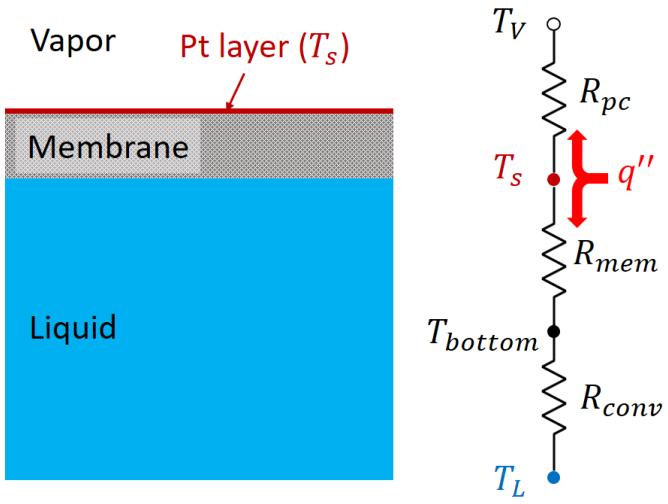

Figure 3.9: Schematic and the thermal circuit of the membrane configuration.

Here we demonstrate the calculation using the experiment of ethanol with 101.3 kPa liquid pressure (the purple curve shown in Figure 3.2 (a)) as an example. The superheat close to the ending of thin film boiling is ~10 °C. The convective heat transfer coefficient between the membrane and the bottom liquid bath below the membrane surface can be estimated using the correlation for natural convection of a heated horizontal plate facing down as [158]

$$h = \frac{k}{L}\mathrm{Nu}_L = \frac{k}{L}0.82\mathrm{Ra}_L{}^{1/5} \tag{3.3}$$

where k is the thermal conductivity of the liquid. With the thermophysical properties of ethanol, the heat transfer coefficient $h = 238\ \mathrm{W\ m^{-2}K^{-1}}$, which gives a thermal resistance $R_{conv} = 4.2 \times 10^{-3}\ \mathrm{m^2K\,W^{-1}}$. Note that the heat transfer coefficient is overestimated, since the correlation deals with free space convection while the actual liquid bath below the membrane is constrained by the liquid feeding column. Still, this convective thermal resistance is significantly larger than the overall thermal resistance of the system (~$10^{-5}\ \mathrm{m^2K\,W^{-1}}$), which indicates that the phase change thermal resistance R_{pc} is close to the overall thermal resistance. Therefore, the heat flux flowing along the thermal pathway on the downward direction in Figure 3.9 is at most ~0.24% of the total heat flux q'' supplied to the heater. The membrane thermal resistance R_{mem} can be estimated by t_{mem}/k_{mem} where k_{mem} is the effective thermal conductivity of the liquid-filled membrane. Thus, the upper bound of the temperature drop across the membrane $T_s - T_{bottom}$ is $0.24\% \cdot q'' t_{mem}/k_{mem}$. We further conservatively assume that k_{mem} is as low as that for an air-filled membrane (close to the membrane itself) which has cross-plane thermal conductivity of ~1.5 W m^{-1} K^{-1} [177], which leads to an upper bound of only ~0.1 °C. This small temperature difference indicates that the liquid flowing along the pores has

temperature very close to the measured wall temperature, which justifies our choice of using the wall temperature as the reference temperature for fluid viscosity.

3.6.2 Maximum heat flux of thin film boiling

In order to predict the maximum heat flux that can be sustained by thin film boiling, a model based on fluid transport was developed. As shown in Figure 3.2, the maximum heat flux within the *thin film boiling* regime corresponds to the CHFs in the water experiments and the transition heat flux in the experiments with other fluids. This maximum heat flux in thin film boiling was achieved when the liquid flow rate driven by the pressure difference between the liquid and vapor chambers was balanced with the vapor flux from the boiling process. Therefore, the maximum heat flux can be estimated as

$$q_t'' = \frac{{D_h}^2(P_L - P_V)}{32\mu L}\rho_l\left[h_{fg} + c_p(T_s - T_L)\right]\eta \qquad (3.4)$$

if assuming circular pore geometry in the AAO. Here, D_h is the average hydraulic diameter of the pores, L is the membrane thickness, η is the membrane porosity, T_s and T_L are the wall temperature and liquid reservoir temperature, respectively, μ, ρ_l, h_{fg}, and c_p are the viscosity, density, latent heat, and specific heat capacity of the working fluid, respectively. In this equation, the viscosity of the liquid μ is highly temperature dependent. By using viscosity values at different temperatures within the experimental temperature range, the calculated heat flux can vary by several times. We choose the wall temperature T_s, which was also the sample surface temperature measured from the Pt thin film heater, to extract the viscosity, as the fluid inside the AAO was estimated to be at the same temperature as T_s based on our heat transfer analysis in Section 3.6.1.

3.6.3 Estimated capillary pressure

For the low surface tension fluid tested in this work, thin film evaporation regime is realized in the experiments, and thus, the CHF of these experiments are higher than the maximum heat flux in thin film boiling calculated using Eq. (3.4). We can estimate the capillary pressure at the highest heat flux using the following equation

$$q''_{CHF} = \frac{{D_h}^2 (P_L - P_V + P_c)}{32\mu L} \rho_l \left[h_{fg} + c_p (T_s - T_L) \right] \eta \tag{3.5}$$

where P_c is the capillary pressure providing extra liquid supply. For an exemplary curve of ethanol with 101.3 kPa liquid pressure shown in Figure 3.2 (a), CHF of 196.2 W cm^{-2} was achieved at a superheat of 26.9 °C. Using this equation, the capillary pressure at CHF is ~45 kPa, which is much smaller than ~331 kPa estimated by the Young-Laplace equation as $P_c = 2\gamma / r_p$ assuming zero contact angle for ethanol on alumina, where γ is the surface tension of ethanol and r_p is the radius of the nanopore. The much smaller capillary pressure realized is likely resulted from the vapor resistance, as will be discussed later.

3.6.4 Kinetic limit calculation

The kinetically limited interfacial heat flux is calculated using the Hertz-Knudsen equation as [178]

$$q''_k = h_{fg} \dot{m} = \sigma h_{fg} \frac{1}{\sqrt{2\pi R}} \left(\frac{P_{eq}}{\sqrt{T_i}} - \frac{P_V}{\sqrt{T_V}} \right) \tag{3.6}$$

where the interface temperature T_i is taken as the membrane surface temperature T_s, and the equilibrium pressure P_{eq} is taken as the saturation pressure at T_s. Due to the small temperature difference, the dimensionless kinetic limited heat flux is almost proportional

to the dimensionless driving potential $\Delta P/P_s$ and fluid-independent, as seen in Figures 3.11 and 3.13 (c) later.

3.7 Discussion

3.7.1 Universal thin film boiling behaviors on multiple fluids

In Section 3.6.2, the maximum heat flux of thin film boiling was modeled. In order to better reflect the effect of the thermophysical properties of the liquid on thin film boiling performance, we defined a normalized liquid property factor Π as [179]

$$\Pi = \frac{\rho_l h_{fg}}{\mu} \Big/ \frac{\rho_{water} h_{fg,water}}{\mu_{water}} \tag{3.7}$$

Π is normalized using water properties and represents the ability to achieve high heat flux in thin film boiling according to Eq. (3.4). The experimental maximum heat fluxes achieved by thin film boiling for different liquids (the CHF for water, including the data reported in Chapter 1, and the transition heat flux for other fluids in Figure 3.2) are divided by the respective liquid property factor, and are plotted against the pressure difference as shown in Figure 3.10. The properties used for calculation of the Π factor are all chosen at 20 °C for simplicity, since the wall temperature at the maximum heat flux points of thin film boiling varies for different liquids.

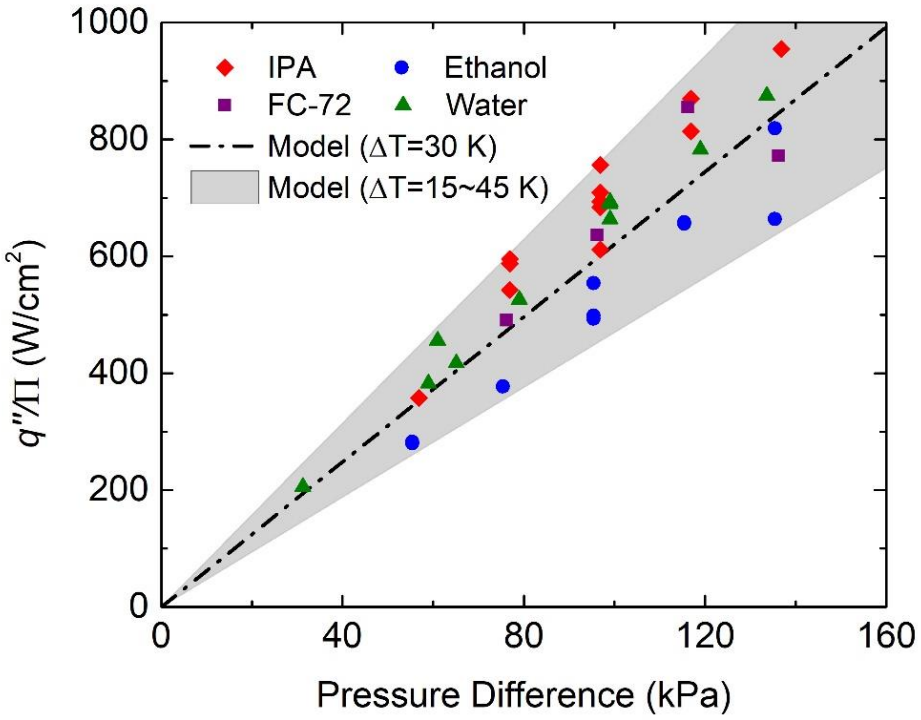

Figure 3.10: Maximum heat flux for thin film boiling (shown by the stars in Figure 3.2, or heat flux at transition points for ethanol, IPA, FC-72, and the CHF for water) divided by the liquid property factor Π (defined in Eq. (3.7)) as a function of pressure difference for various fluids. Experimental data for water from Chapter 2 are also included. The model of transition for water calculated using Eq. (3.4) is also shown, where the dash dot line corresponds to a superheat of 30 K and the grey band corresponds to the superheat range of 15~45 K.

It can be seen from Figure 3.10 that the Π-normalized maximum thin film boiling heat flux as a function of pressure difference for various fluids are converged into one straight line from the origin. In another word, the normalized maximum heat flux has a linear relationship with the pressure difference, and the slopes of this linear relationship for different fluids are almost the same. The calculated results from Eq. (3.4) for water with different superheat are also shown in Figure 3.10. The agreement between the normalized heat flux and the calculated transition further confirmed the validity of the model. We

notice that there is still certain mismatch in the results, and the convergence of the data points are not perfect. For example, the data points for ethanol are slightly below the points for other fluids. This can be attributed to the fact that we used 20 °C to evaluate all the liquid properties. In the real experiments, the liquids were not at exact 20 °C, and the thermophysical properties of different fluid could have different extent of temperature dependence, which may have resulted in errors in using the liquid property factor Π. Nevertheless, we can still use the liquid property factor for the purpose of fluid selection and heat flux prediction in the thin film boiling configuration. And the fact that these four fluids with vastly different surface tension values all show the same behaviors strongly demonstrate the universality for the thin film boiling scheme. This is especially important for organic solvents and dielectric fluids, as they tend to have much lower boiling CHFs due to their low latent heat and are difficult to engineer due to their low surface tension (virtually all the surfaces are highly wettable for these fluids).

3.7.2 Near kinetic limit at the onset of pore-level thin film evaporation

The evaporative heat flux q'' can be normalized using the maximum heat flux equation [178] as $\overline{q''} = q''/(\rho_{v,s} h_{fg} \sqrt{\frac{RT_s}{2\pi}})$ where R is the gas constant, T_s is the membrane surface temperature which also represents the liquid temperature, and $\rho_{v,s}$ is the density of saturated vapor at T_s. The experimental results at the transition points between the boiling and evaporation regimes (i.e., onset of pore-level evaporation or the termination point of thin film boiling regime) shown by stars in Figure 3.2 for different fluids are normalized and shown in Figure 3.11, where the horizontal axis is the dimensionless driving potential for evaporation [173] $\Delta P/P_s$ where $\Delta P = P_s - P_V$ and P_s is the saturated pressure at T_s.

Although this dimensionless driving potential is not directly calculated from superheat, it is closely related to superheat which is calculated as $T_s - T_V$ where T_V is the saturation temperature at P_V.

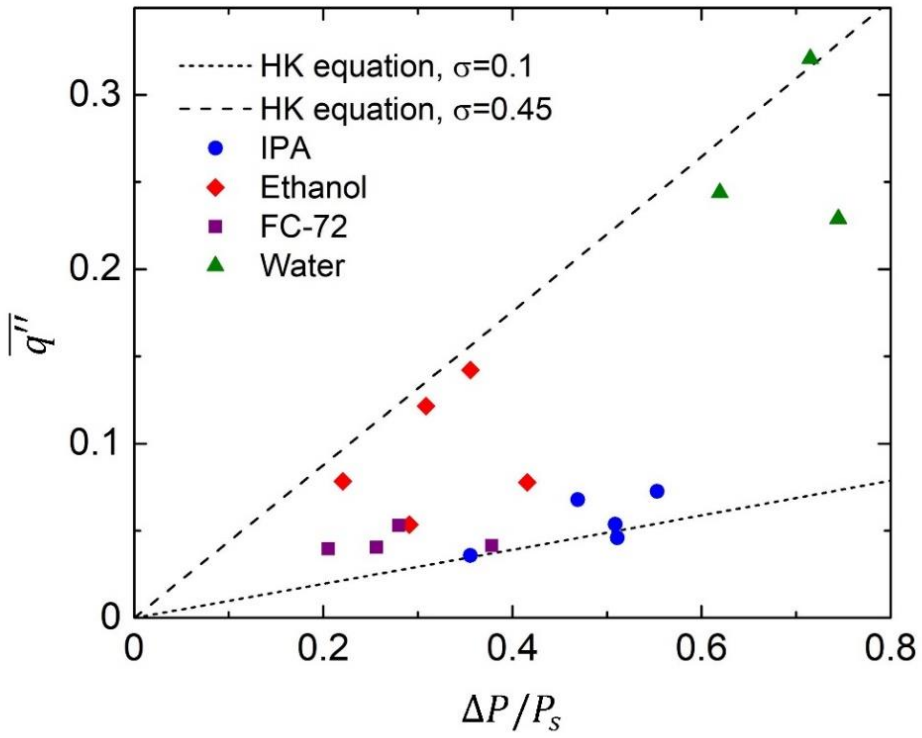

Figure 3.11: Normalized evaporative heat flux for different fluids at the onset of pore-level evaporation regime shown in Figure 4.2 as a function of the dimensionless driving potential.The two dashed lines represents the kinetic limit results calculated from the HK equation (Eq. (3.6)) with different values for the accommodation coefficient (σ= 0.1 and 0.45).

The kinetic limited evaporation heat flux is also calculated using the Hertz-Knudsen equation (HK equation, see Section 3.6.4, Eq. (3.6)) and plotted in Figure 3.11 with different values for the accommodation coefficient (σ), which represents the ratio of the number of molecules evaporated from the interface to the number of liquid molecules at

the interface. Note that this model calculates the heat flux from a flat liquid-vapor interface, corresponding to the case where the liquid is evaporating from the entire membrane surface, which could be true at the transition points since the liquid might spread outside the pores when the interface is pinned at the entrance of the pores [174], while the interface receding inside the pores is more likely to happen with higher heat flux. The experimental results at the onset of the evaporation regime showed near kinetic limit behavior and agree well with the calculated results from the kinetic limit with a reasonable range for the accommodation coefficient range (0.1 to 0.45) [67, 173], which indicate that the heat transfer characteristics for the transition points are close to those of the kinetic limit. This agreement shows that the liquid-vapor interfacial resistance is the dominant one, compared to other possible resistances in the system (such as fluid flow and vapor transport).

In the thin film boiling regime, the thickness of the liquid induces thermal resistance for conduction. Right after the transition happened, the characteristic length scale of the liquid layer became the pore radius r_p. That is, the conduction thermal resistance in the liquid phase (scales with r_p/k_l, where k_l is the liquid thermal conductivity) became small and resulted in low superheat to sustain the heat flux at the transition point. For example, in the IPA experiment with 101.3 kPa liquid pressure (the purple circles in Figure 3.2 (b)), the conduction resistance estimated by r_p/k_l is ~7×10^{-7} m^2 K W^{-1}, which is still orders of magnitude smaller than the overall thermal resistance of the system (~1.6×10^{-5} m^2 K W^{-1} achieved at the transition point). Therefore, the liquid thermal conduction resistance is not important in the thin film evaporation regime.

At the pore-level evaporation regime, three possible resistances could limit the highest heat flux that can be dissipated: the kinetic limited interfacial resistance of

evaporation, the hydraulic resistance of liquid transport, and the vapor diffusion/advection resistance from interface to the far field in the vapor space. At the onset of evaporation regime, the liquid-vapor interface forms menisci and provides sufficient liquid transport, rendering the liquid transport resistance less important, and the interface is mostly likely either pinned on top of the pores or spread outside the pores, rendering the vapor removal resistance small. Therefore, at these transition conditions, the kinetic limited interfacial resistance becomes the dominant resistance, resulting in the heat transfer characteristics close to those predicted by the kinetic limit.

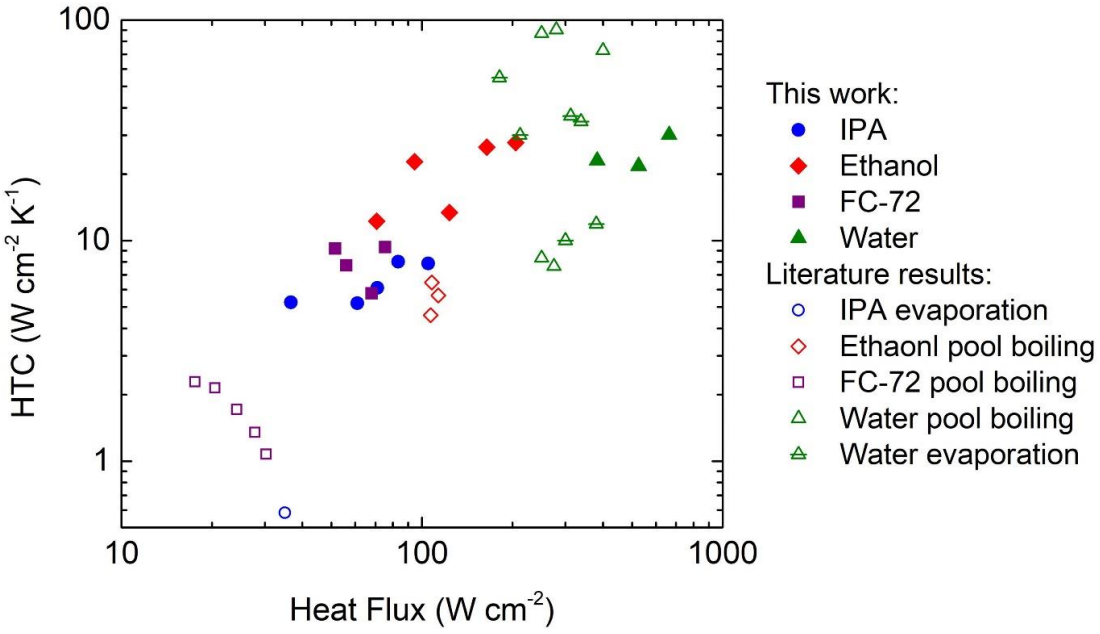

Figure 3.12: HTC-heat flux plot at the transition points for different fluids. PCHT experiments for these fluids reported in literature are also plotted for comparison, including evaporation of IPA [157] and water [67, 173], and pool boiling of ethanol [176], FC-72 [180], and water [33, 37, 45].

Due to the near-kinetic-limit condition, PCHT at the transition show high heat flux achieved at small superheat. Figure 3.12 shows the heat flux vs. HTC plot of the transition points measured in this work for various fluids (stars in Figure 3.2), along with other experimental results on PCHT of these fluids reported in the literature, showing that the transition points for these fluids possess both high heat flux and high HTC, compared to the same fluids from the previously reported pool boiling and evaporation experiments. In our previous work, a CHF of over 1.8 kW cm^{-2} was achieved for experiments with water, which is close to the previously reported record-high CHF in boiling heat transfer by Moghaddam et al. [49]. In this work, what is perhaps more remarkable is for the other three fluids with lower surface tension, which showed that the heat fluxes and HTC at the transition points are significantly higher than those from the traditional pool boiling or evaporation. For example, CHF of ~60 W cm^{-2} and HTC of 2.7 W cm^{-2} K^{-1} on a plain surface and CHF of ~110 W cm^{-2} and HTC of 6.5 W cm^{-2} K^{-1} on structured surfaces were achieved in pool boiling with ethanol at atmospheric pressure [176], and the CHF decreases with decreasing saturation pressure. In comparison, the transition heat flux of our current work using ethanol is exceeding 200 W cm^{-2} with HTC close to 28 W cm^{-2} K^{-1} with 5.9 kPa saturation pressure. Moreover, the maximum transition heat flux for FC-72 is 75 W cm^{-2} and corresponding HTC is over 9 W cm^{-2} K^{-1}, which is significantly higher than the CHF (<30 W cm^{-2}) and HTC (<2.3 W cm^{-2} K^{-1}) reported in pool boiling literature [50, 180, 181]. More importantly, the significant CHF and HTC enhancement achieved at the transition points, which were universally demonstrated for various fluids, indicates the possibility of using nanoporous membranes for achieving kinetic limited high heat flux PCHT.

3.7.3 Vapor resistances in thin film evaporation regime

For all of the curves for low surface tension liquids, although there were stable thin film evaporation regimes beyond the transition points shown in the previous section, the HTC (or slope of heat flux vs. superheat) decreased and became far lower than that of the transition points as shown in Figure 3.2. We believe this rapid decrease in HTC is most likely caused by the increasing vapor resistance when the evaporation progressed beyond the transition points. Since the HTC of the evaporation regime is smaller than that of the transition points which is close to the kinetic limit (see Figure 3.14), there must be another dominant resistance that is much greater than the interfacial resistance in this evaporation regime. While we were unable to directly measure the remaining two resistances (namely, fluid flow and vapor transport) in our experiments, here we carried out additional experiments that suggested the dominant effect of the vapor resistance.

We used IPA as an example, and conducted experiments with various vapor pressures while maintaining the pressure difference across the membrane in a narrow range, as shown in Figure 3.13 (a). The vapor pressure was varied from 5 values: 1.1, 2.3, 4.4, 8.2, and 14.3 kPa, corresponding to the saturated IPA vapor temperature of 0, 10, 20, 30, and 40 °C, respectively. Except for the experiments with vapor pressure at 14.3 kPa, the liquid pressure was fixed at atmospheric pressure (101.3 kPa). For the vapor pressure at 14.3 kPa, the liquid pressure was fixed at 111.3 kPa so that the pressure difference across the membrane (97.0 kPa) was close to that of the other experimental conditions (ranging from 93.1 to 100.2 kPa). In Figure 3.13 (b), the curves from Figure 3.13 (a) are truncated

at the transition points (between the boiling and evaporation regimes), and are shown as heat flux as a function of superheat.

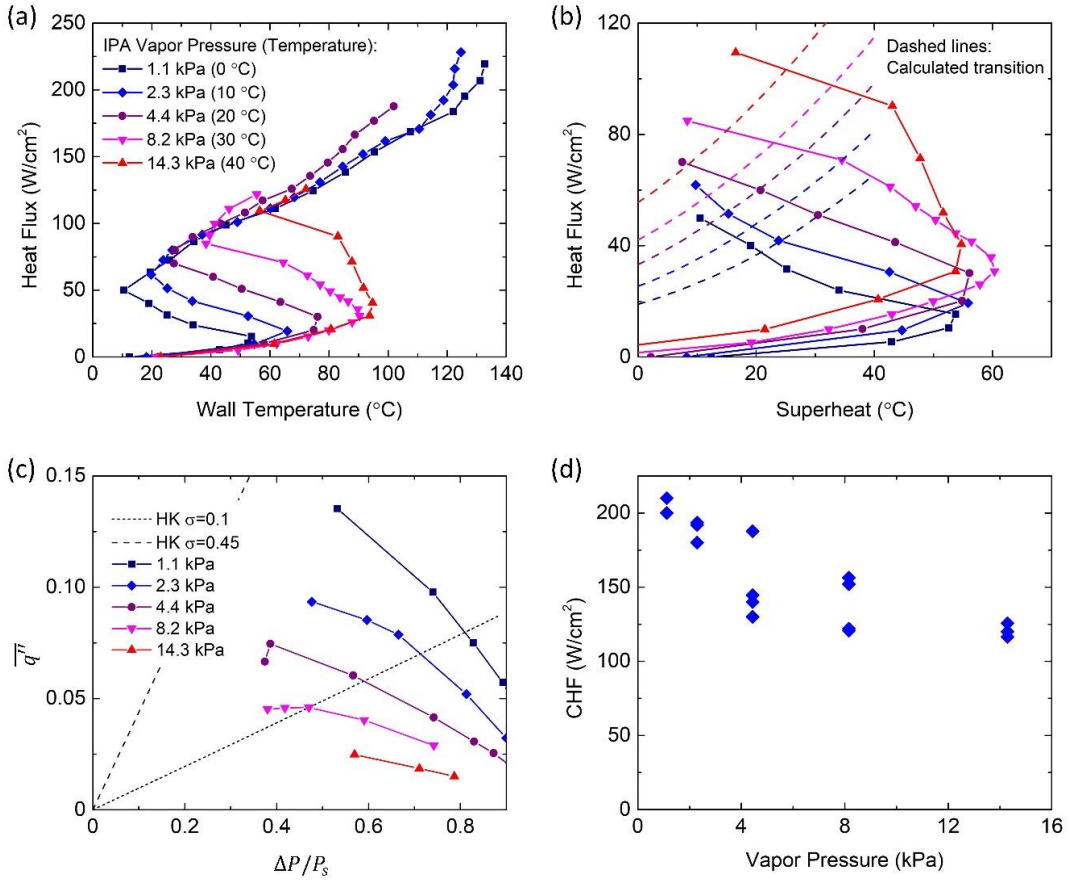

Figure 3.13: Heat transfer experimental results with IPA under various vapor pressures. (a) Heat flux as a function of wall temperature with varying vapor pressure and similar pressure difference (ranging from 93.1 to 100.2 kPa) using IPA as the working fluid. For vapor pressure of 1.1, 2.3, 4.4, and 8.2 kPa, the liquid pressure was 101.3 kPa; for vapor pressure of 14.3 kPa, the liquid pressure was 111.3 kPa. (b) Heat flux as a function of superheat for the thin film boiling part of the curves shown in (a), along with the model for transition (dashed lines). The color of the dashed lines corresponds to the experimental conditions of the curves with the same color shown in (a). (c) Dimensionless heat flux as a function of the dimensionless driving potential for the evaporation part of the curves shown in (a), along with the HK models. (d) Experimental CHF of IPA under different vapor pressure conditions.

It can be seen in Figure 3.13 (a) that all of the curves display the typical profile with three regimes as discussed above, but the experiments under different vapor pressures show different transition heat fluxes and at different wall temperatures. This can be explained again by the fluid transport through the membrane. As discussed before, the transition point shows near kinetic limit behavior with small wall superheat, as seen in Figure 3.13 (b). The different saturation pressures with similarly small superheat gave different wall temperatures (which are also fluid temperatures) and thus significantly different fluid viscosities, and with similar driving force for liquid transport ($P_L - P_V$), vastly different transition heat fluxes were obtained. Due to the varying saturation temperature for the curves shown in Figure 3.13 (b), the transition points of the curves were not plotted in Figure 3.10 which is based on the liquid property factor Π evaluated at 20 °C. The transition heat flux estimated by Eq. (3.4) is also shown in Figure 3.13 (b) as dashed lines with different colors representing corresponding vapor pressure conditions, showing good agreement between the expected transition heat flux and the experimental results.

In Figure 3.13 (c), the experimental evaporation regime for the experiments with IPA at various vapor pressures (shown in Figure 3.13 (a)) are normalized and plotted along with the HK models. In Figure 3.14 below, the HK models and the experimental curves are also plotted together in heat flux-superheat plot. Figure 3.14 (a) is the exact same plot as Figure 3.13 (c), while Figure 3.14 (b-f) each shows the experimental curve for one vapor pressure condition along with two HK models under that condition. For different vapor pressure, the HK models with the same accommodation coefficient produce different heat flux under the same superheat, but they collapse into one curve in the dimensionless plot as shown in Figure 3.14 (a).

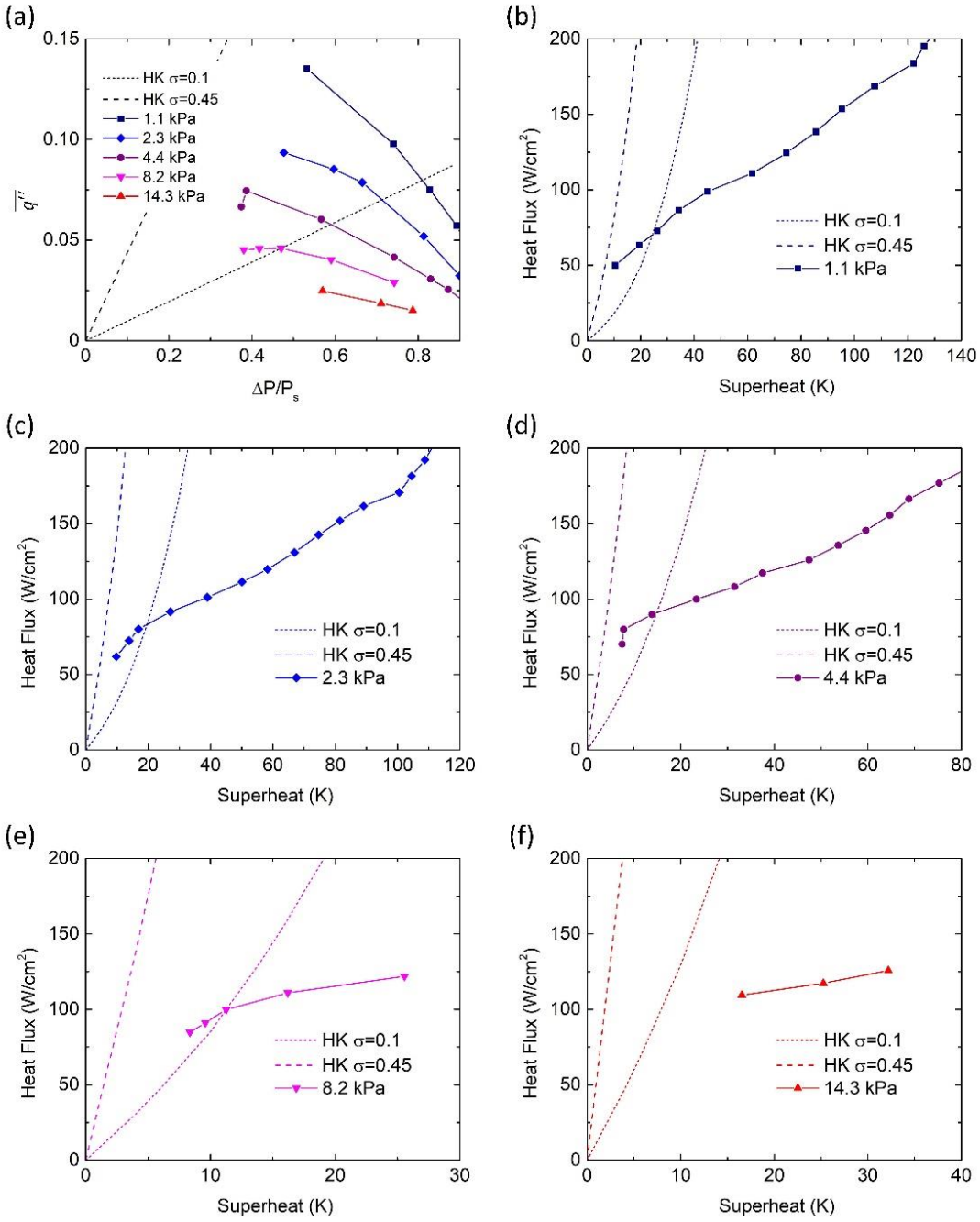

Figure 3.14: (a) The same as Figure 3.13 (c), showing the dimensionless heat flux vs. driving potential for the evaporation part of the curves shown in Figure 3.13 (a). (b-f) Heat flux vs. superheat curves along with HK model calculation results for the curves shown in panel (a), where each panel represents one vapor pressure condition.

The experimental heat flux deviates away from the kinetic limit as the driving potential increases (which corresponds to the superheat increase, as shown in Figure 3.14), which is likely due to the increasing vapor resistance. When heat flux (and also superheat) is increased during the experiment for the evaporation regime, a higher flux of vapor molecules need to be removed from the interface. Meanwhile, the interface is more likely to recede inside the pores and result in extra resistance for vapor to escape from the pores. Both the increased flux of vapor molecules and the possibility of interface receding increase the vapor diffusion/advection resistance, and thus the experimentally achieved heat flux is significantly smaller than the kinetic limit. The normalized flux is decreasing as heat flux increases, and the CHF achieved is still much smaller than what could be expected (see Section 3.6.3), indicating the increasing dominance of vapor resistance. We also notice that the experimental curves with smaller vapor pressure is closer to the calculated kinetic limit, which can also be attributed to the smaller vapor resistance at the lower pressure (a situation that is similar to the near-kinetic limit behavior at low Mach number, as reported by Lu et al. [173]).

More experiments are carried out following the same conditions shown in Figure 3.13 (a), and Figure 3.13 (d) shows the recorded CHF as a function of the vapor pressure in these experiments with IPA. The pressure difference across the membrane for these experiments are all similar (93.1~100.2 kPa) despite different vapor pressures, but the resulting CHF values show a decreasing trend with increasing vapor pressure, which further proved the dominance of vapor resistance. If a nanoporous membrane with highly uniform pore geometry and heater deposition is used to eliminate the hotspot, and a pure

vapor ambient with low pressure is maintained, a much higher heat flux could be possibly realized through thin film evaporation [173].

3.8 Conclusion

In this work, we experimentally studied thin film boiling and evaporation heat transfer of different types of fluids through nanoporous membranes. Transition from thin film boiling to evaporation was observed for the three low surface tension fluids (ethanol, IPA, and FC-72) but not for water, which was attributed to hotspot formation due to membrane nonuniformity. The transition heat flux for these fluids universally agreed with the model prediction. At the transition points, interfacial resistance dominates the heat transfer behavior which resulted in heat flux and HTC close to the kinetic limit. After transition into the pore-level evaporation regime, the vapor resistance became increasingly dominant and eventually limited the achievable CHF. Our work provides a systematic study of PCHT through nanoporous membranes and can benefit the understanding and application of PCHT through nanoporous membranes for thermal management and modulation.

Chapter 3, in part, is a reprint of the material as it appears in “Widely tunable thin film boiling heat transfer through nanoporous membranes”, *Nano Energy* 54 (2018): 297-303, by Qingyang Wang and Renkun Chen [182]. The dissertation author was the first author of this paper.

Chapter 3, in part, is a reprint of the material as it appears in “Transition between

thin film boiling and evaporation on nanoporous membranes near the kinetic limit", *International Journal of Heat and Mass Transfer* 154 (2020): 119673, by Qingyang Wang, Yang Shi, and Renkun Chen [147]. The dissertation author was the first author of this paper.

Chapter 4 Understanding length scale of radiation thermal conductivity at high temperature

4.1 Introduction

The increase of the operation temperature of combustion engines directly increases the efficiency according to thermodynamic theory. Typically made of refractory-oxide ceramic materials, thermal barrier coatings (TBCs) possess low thermal conductivity and high temperature stability, which are of great importance in reducing the surface temperature of the metal parts in the engine which cannot withstand high temperature for long time, thus enabling the operation under much higher temperature [89].

Low thermal conductivity at high temperature is one of the most important features for TBC materials. The most commonly used TBC material is yttria-stablized zirconia (YSZ), in which a few mol% of Y_2O_3 was introduced into ZrO_2 to stabilize the phase and also act as impurities to enhance phonon scattering [90]. One of the typical formula, 8YSZ ($(Zr_{0.852}Y_{0.148})O_{2-\delta}$), has a thermal conductivity of ~2.2 W m^{-1} K^{-1} at 1000 °C [9]. Significant efforts have been made in searching for new TBC materials with lower thermal conductivity in the past several decades, mostly focused on the reduction of thermal conductivity through increased phonon scattering [90, 98, 112, 113], including the newly emerged concept of high entropy oxides with multiple (typically five) cations and a "severely distorted lattice" [148, 183, 184]. A great number of new TBC materials have been reported with thermal conductivity below that of 8YSZ, with some compositions possessing thermal conductivity as low as ~1.3 W m^{-1} K^{-1} at 1000 °C [146].

In order to understand the physics behind the low thermal conductivity of the new TBC materials and obtain guidelines for searching for future materials, modeling of the temperature-dependent thermal conductivity of the materials has been explored in conjunction with the experimental measurements for thermal conductivity [8, 145]. Notably, the reported experimental thermal conductivity for some of the TBC materials showed significant increase at high temperatures, which could not be explained by either phonon Umklapp scattering or amorphous limit model, and was usually explained by the increased internal radiation [108, 122, 128]. However, even though it is well-known that the radiative thermal transport within the solid could be significant at high temperature [13], no prior study has been reported to quantify the radiative contribution in TBC materials. The lack of a model to separate conductive and radiative contribution in the thermal conductivity makes it difficult for researchers to compare their delicate phonon/diffuson model with the experimental measurements, especially at high temperatures which is of most interest for practical applications.

Traditionally, the radiative thermal conductivity within a participating medium is described by the Rosseland diffusion approximation model as [185]

$$k_r = \frac{16n^2\sigma T^3}{3\beta_R} \tag{4.1}$$

where n is the refractive index, σ is the Stefan-Boltzmann constant, T is the temperature, and β_R is the Rosseland mean extinction coefficient. The underlying assumption is that for the entire spectrum, the photons have mean free path much smaller than the physical size of the sample, and the photon transport is diffusive (hence the name of the diffusion approximation). However, the Rosseland diffusion approximation might be invalid for some refractory oxide with some extent of semi-transparency in the infrared, such as

zirconia [14], as the photon mean free path could be larger than the dimension of the samples used for thermal measurement.

Due to the simplicity in sample preparation, the high throughput, and the availability of commercial equipment, the laser flash analysis (LFA) is usually used for characterizing the thermal property of a dense solid at high temperatures, including the measurement of TBC materials. The thermal conductivity of TBC materials can then be determined by multiplying the thermal diffusivity measured by LFA with the separately measured density and specific heat capacity. In a typical LFA measurement, a laser pulse heats up the front surface of a sample, which is usually in a pellet geometry, while the time-dependent temperature rise on the rear surface is monitored by an infrared detector. In order to enhance the laser absorption of the front surface and the infrared emission of the rear surface, both surfaces are coated with a thin layer of highly absorbing material, such as graphite. When the sample is semi-transparent, the black coatings on the two surfaces of the sample could have direct radiative transfer, which would result in an instantaneous temperature rise on the rear surface right after the laser pulse, and consequently, the thermal diffusivity of the material could not be accurately extracted from the traditional analytical model for LFA.

This inaccuracy caused by the direct transmission between surfaces could be minimized by coating both surfaces with low emissivity metal layer to reduce the radiative emission [98]. However, the coating process of metal layer is expensive and slow [186], especially for high temperature measurements which require ~μm thick noble metal such as gold or platinum that is stable at high temperature. An alternative way is to apply the transparent fitting model by Mehling, et al. [187] which used a transparency parameter in

the boundary conditions to account for the direct radiative exchange between surfaces. Although the thermal diffusivity extracted from this transparent model excludes the radiation by long mean free path photons that ballistically transmit from the front to rear surfaces, it can still include the internal radiation by the short mean free path photons that transport diffusively. Consequently, for some materials whose thermal diffusivities are measured and extracted by the transparent model, the reported thermal diffusivity still increases with increasing temperature at high temperatures, indicating the inclusion of the radiative contribution in the reported thermal diffusivity [9].

In order to accurately separate the conductive and radiative contributions from the LFA measurement, coupled conduction-radiation heat transfer modeling is needed. Transient coupled heat transfer problem has been studied in the past, which was motivated from glass forming applications and thus mostly focused on glass materials [188-191]. Although some researchers [192] tried to use the coupled heat transfer model in conjunction with experimental measurements to extract the phonon thermal diffusivity of glass materials, the measurements were constrained to relatively low temperature, and the model was under the assumption of no heat loss which is invalid especially at high temperatures. None of the models have been implemented to accurately obtain the conductive thermal diffusivity from the widely used LFA equipment with <1 ms pulse time (which makes numerical calculation within the pulse time infeasible).

In this work, we develop a numerical model for the transient coupled conduction-radiation problem simulating the laser flash measurement condition. Given the conductive thermal diffusivity and optical property of the material, the temperature rise as a function of time on the rear surface of a sample during LFA measurements can be predicted, which

was then compared with the experimental temperature rise profile obtained in LFA measurement. By sweeping the input conductive thermal diffusivity over a range of values, the "true" diffusivity was obtained as the value whose corresponding temperature rise profile shows the best fit with experimental curve based on a least square method. Fused silica was used to demonstrate the current methodology. It is found that at high temperatures, the thermal diffusivity obtained from the widely implemented transparent model [187] contains non-negligible radiative contribution, since it only excludes the photons that transmit directly across the sample. In comparison, the diffusivity obtained from the coupled heat transfer model contains only the conductive contribution, since the photons with wide range of mean free paths have all been correctly accounted for. Our work provides a methodology to quantify the radiative contribution for the measured thermal conductivity of TBC materials at high temperatures, and could help the physical understanding of the abundant data for the reported new material compositions in recent years.

4.2 Experimental

4.2.1 Laser flash measurement

The samples chosen in this study is quartz glass, which has richly documented properties and is used to validate the model. The quartz pellet with 12.7 mm diameter and 1.53 mm thickness were purchased from McMaster Carr. It is worth noting that although the sample is labeled as quartz by the vendor, we believe it is similar to fused silica (or sometimes called fused quartz) instead of crystalline quartz based on the room temperature

thermal conductivity of 1.4 W m^{-1} K^{-1} listed in its product data sheet, which was also confirmed by our measurement shown later.

A Netzsch LFA 467 HT HyperFlash Analyzer was used to measure the thermal diffusivity of the sample pellet in an argon gas environment from 25 °C to 1200 °C with 200 °C interval. Prior to measurements, the sample was spray coated with a thin layer of graphite on both surfaces to enhance the front surface laser absorption and rear surface infrared emission.

At each specified temperature, the sample was placed in thermal equilibrium with the furnace temperature for four minutes before measurements started. The front surface of the sample was subjected to a laser pulse whose intensity profile was close to a square function with a pulse time of 0.6 ms. The rear surface temperature rise was monitored by an infrared detector, which was exported after the measurements. The conductive thermal diffusivity of the sample was then obtained by fitting using two different models, namely, the transparent model and the coupled heat transfer model, which will be described in Section 4.3.

4.2.2 Spectral optical property measurement

The laser flash measurement requires a thin layer of high emissivity graphite coating on both the front and the rear surfaces of the sample. The spectral absorptance of the coating is an important input parameter in the coupled heat transfer model described later in Section 4.3, which was measured using a UV-Vis spectrometer (Jasco V780 UV-Vis) with a Spectralon-coated integrating sphere for wavelength range from 280 nm to 2.5 μm and a Fourier-transform infrared (FTIR) spectrometer (ThermoFisher Nicolet 6700,

with a Perkin Elmer gold integrating sphere) for wavelength range from 2.5 μm to 16 μm. A silicon wafer was used as the substrate, and the graphite spray was applied on the Si substrate using same procedure as the coating on the sample for laser flash measurement.

The optical property of the sample also serves as an input parameter for the coupled model, as it is directly related to the internal emission/absorption behavior. The spectral refractive index and absorption index are widely reported for various types of silica glass in the literature. Here, we also performed spectral transmittance measurement using FTIR spectrometer for the quartz sample used in this study, which was used to obtain the absorption index of the sample and compare with the reference values, as will be discussed later.

4.3 Modeling

4.3.1 Mathematical formulation

In order to simulate the experimental conditions of the laser flash measurement process, we develop the model based on a homogeneous, isotropic, and infinitely wide slab with thickness of d, as shown in Figure 4.1.

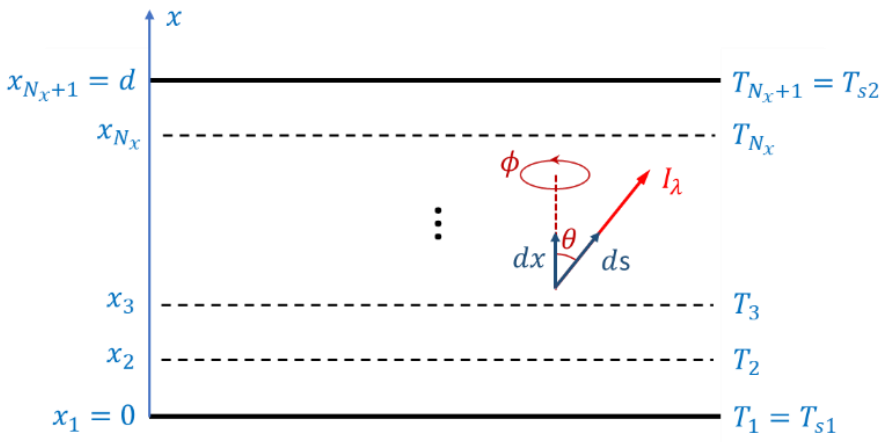

Figure 4.1: Schematic of the heat transfer domain of the coupled model.

The slab material is assumed to be absorbing and not scattering in our current model, which represents the typical condition in the laser flash measurement of dense ceramic materials. The temperature profile $T(x,t)$ of the transient coupled conduction-radiation problem is governed by the following equation [185]:

$$\rho c_p \frac{\partial T(x,t)}{\partial t} = -\nabla \cdot \left(-k \frac{\partial T(x,t)}{\partial x} + q_r \right) \tag{4.2}$$

where ρ, c_p, and k are the density, specific heat capacity, and thermal conductivity of the slab material, respectively, and q_r is the radiative heat flux. For isotropic material with constant thermal conductivity, Eq. (4.2) becomes

$$\rho c_p \frac{\partial T(x,t)}{\partial t} = k \frac{\partial^2 T(x,t)}{\partial x^2} - \text{div } q_r \tag{4.3}$$

The radiative heat flux q_r can be represented by the integration of spectral directional radiative intensity I_λ over the full spectrum and all solid angles as [191]

$$q_r = \int_0^\infty \left(2\pi \int_{-1}^{1} \mu I_\lambda \, d\mu \right) d\lambda \tag{4.4}$$

where the parameter 2π comes from the integration of azimuthal angle and μ is the cosine of the polar angle. The spectral directional intensity I_λ in the material is described by the following equation of radiative transfer in an absorbing-emitting (but no scattering) medium [185]:

$$\frac{dI_\lambda}{ds} = \kappa_\lambda (I_{b\lambda} - I_\lambda) \tag{4.5}$$

where κ_λ is the absorption coefficient, $I_{b\lambda}$ is the black body emissive intensity at wavelength λ, and ds is the differential optical path as shown in Figure 4.1. Substituting $ds = dx/\cos\theta = dx/\mu$ in Eq. (4.5), the radiative transfer equation becomes

$$\mu \frac{dI_\lambda}{dx} = \kappa_\lambda (I_{b\lambda} - I_\lambda) \tag{4.6}$$

Thus, the divergence of the radiative heat flux (div q_r) in Eq. (4.3) can be obtained as

$$\text{div } q_r = \frac{dq_r}{dx} = \int_0^\infty \left(2\pi \int_{-1}^{1} \mu \frac{dI_\lambda}{dx} d\mu \right) d\lambda \tag{4.7}$$

Substituting Eq. (4.6) into Eq. (4.7), we have

$$\text{div } q_r = \int_0^\infty \left(2\pi \kappa_\lambda \int_{-1}^{1} (I_{b\lambda} - I_\lambda) d\mu \right) d\lambda \tag{4.8}$$

We apply the well-known two-flux approximation, assuming isotropic hemispherical intensities on the positive and negative x directions, and transform the integration over μ in Eq. (4.8) into the summation of two terms, and Eq. (4.8) becomes

$$\text{div } q_r = \int_0^\infty 2\pi \kappa_\lambda \left(2I_{b\lambda} - {I_\lambda}^+ - {I_\lambda}^- \right) d\lambda \tag{4.9}$$

where ${I_\lambda}^+$ and ${I_\lambda}^-$ represents the two constant hemispherical intensities.

The integration over the entire wavelength spectrum in Eq. (4.9) is replaced by the summation of N_m spectral bands for numerical reasons. Within each spectral band $(\lambda_m, \lambda_{m+1})$, the refractive index n_λ and absorption coefficient κ_λ are taken as constants n_m and κ_m.

$$\int_0^\infty 2\pi\kappa_\lambda\left(2I_{b\lambda} - {I_\lambda}^+ - {I_\lambda}^-\right) d\lambda = \sum_{m=1}^{N_m} 2\pi\kappa_m\left(2I_{b\lambda_m} - {I_m}^+ - {I_m}^-\right) \qquad (4.10)$$

in which the black body emissive intensity within the m-th wavelength band $I_{b\lambda_m}$ is represented by

$$I_{b\lambda_m}(T) = \frac{{n_m}^2}{\pi}\sigma T^4 f_{(\lambda_m,\lambda_{m+1})} \qquad (4.11)$$

where $f_{(\lambda_m,\lambda_{m+1})}$ is the fractional emissive power of Planck distribution within the wavelength band $(\lambda_m, \lambda_{m+1})$ at temperature T. The radiative intensities at a specific coordinate x $(0 \le x \le d)$ within the m-th wavelength band in the positive and negative directions can be obtained from the following equations:

$${I_m}^+(x) = {I_m}^+(0)e^{-\kappa_m x} + \kappa_m \int_0^x I_{b\lambda_m}(T_{x'})e^{-\kappa_m(x-x')}dx' \qquad (4.12a)$$

$${I_m}^-(x) = {I_m}^-(d)e^{-\kappa_m(d-x)} + \kappa_m \int_x^d I_{b\lambda_m}(T_{x'})e^{-\kappa_m(x'-x)}dx' \qquad (4.12b)$$

where $T_{x'}$ represents the temperature at location x'.

During the LFA measurement, the sample is sprayed with thin graphite coatings on both sides of the surfaces to enhance flash absorption and infrared emission. To simulate the simplified experimental condition, we assume that the graphite coatings on both surfaces of the sample (at $x = 0$ and $x = d$) are opaque and have no thickness, with its spectral absorptance (equal to the emittance) represented by ε_λ. This spectral absorptance

(or emittance) is also assumed to be constant (ε_m.) in each wavelength band (gray-band assumption). Thus, the boundary condition for the radiative intensities are

$$I_m{}^+(0) = \varepsilon_m I_{b\lambda_m}(T_{s1}) + (1-\varepsilon_m) I_m{}^-(0) \tag{4.13a}$$

$$I_m{}^-(d) = \varepsilon_m I_{b\lambda_m}(T_{s2}) + (1-\varepsilon_m) I_m{}^+(d) \tag{4.13b}$$

where T_{s1} and T_{s2} are the surface temperatures at $x = 0$ and $x = d$, respectively.

Therefore, the governing equation (4.3) becomes

$$\rho c_p \frac{\partial T(x,t)}{\partial t} = k \frac{\partial^2 T(x,t)}{\partial x^2} - \sum_{m=1}^{N_m} 2\pi\kappa_m \left(2I_{b\lambda_m} - I_m{}^+ - I_m{}^-\right) \tag{4.14}$$

with the following boundary conditions representing the experimental condition:

$$-k\frac{\partial T}{\partial x}\Big|_{x=0} = h(T_0 - T_{s1}) - \pi \sum_{m=1}^{N_m} I_m{}^+(0) + \pi \sum_{m=1}^{N_m} I_m{}^-(0) \tag{4.15a}$$

$$-k\frac{\partial T}{\partial x}\Big|_{x=d} = h(T_{s2} - T_0) + \pi \sum_{m=1}^{N_m} I_m{}^-(d) - \pi \sum_{m=1}^{N_m} I_m{}^+(d) \tag{4.15b}$$

where T_0 is the ambient temperature, and $h = 4\varepsilon\sigma {T_0}^3$ is the heat transfer coefficient of radiative heat loss at the two surfaces with ε being the average emittance of the graphite coating.

In the LFA measurement, the sample is initially maintained at the ambient temperature inside the furnace before the front surface of the sample is heated by a short laser pulse. The pulse time in the laser flash experiment in our current study is ~0.6 ms, which makes numerical treatment of the pulse time unfeasible. Since the pulse time is orders of magnitude shorter than the characteristic time of heat transfer process (~d^2/α where α is the thermal diffusivity), here we neglect the detailed heat transfer process within the pulse time range and consider only conduction. Since the thermal penetration depth

within the pulse time is significantly smaller than the sample dimension, and the pulse heating power can be assumed constant within the pulse time, the temperature distribution at the end of the pulse (which is also taken as the initial temperature condition for the model) is estimated by the semi-infinite solid subject to a constant boundary heat flux [158]. Therefore, the initial condition for Eq. (4.14) is

$$T(x,0) = T_0 + \frac{q_s}{k}\left[\left(\frac{4\alpha t_s}{\pi}\right)^{1/2} e^{-x^2/4\alpha t_s} - x\,\mathrm{erfc}\left(\frac{x}{\sqrt{4\alpha t_s}}\right)\right] \tag{4.16}$$

where q_s and t_s are the pulse heat flux and the pulse time, respectively.

4.3.2 Numerical method

The coupled conduction-radiation problem described above has to be numerically solved since no analytical solution exists. We used finite difference method and solved the temperature distribution step-by-step, following the method used in Hahn et al. [191]. The temperature distribution over the spatial dimension d is calculated at $(N_x + 1)$ equally spaced discrete points x_i $(i = 1,2,\dots,N_x + 1,$ with $x_1 = 0$ and $x_{N_x+1} = d,$ as shown in Figure 4.1), which divide the sample thickness d into N_x equal segments. The governing equation (4.3) becomes

$$\begin{aligned}\rho c_p \frac{T(x_i,t_{j+1}) - T(x_i,t_j)}{t_{j+1} - t_j} \\ = \frac{k}{2}\left(\frac{\partial^2 T(x_i,t_{j+1})}{\partial x^2} + \frac{\partial^2 T(x_i,t_j)}{\partial x^2}\right) \\ - \frac{1}{2}\left(\mathrm{div}\, q_r(x_i,t_j) + \mathrm{div}\, q_r(x_i,t_{j+1})\right)\end{aligned} \tag{4.17}$$

Starting from the initial condition, the temperature distribution array for the next time step $T(x_i, t_{j+1})$ is solved from the temperature array from the previous time step $T(x_i, t_j)$ through Eq. (4.17).

The numerical strategy of the current model is to convert the complex set of Eq. (4.17) evaluated at $i = 1,2, \dots, N_x + 1$ into a linear system of equations about $T(x_i, t_{j+1})$ to improve the calculation speed. Finite difference method was used to treat the second order derivative in Eq. (4.17)

$$\frac{\partial^2 T(x_i, t_j)}{\partial x^2} = \frac{T(x_{i+1}, t_j) + T(x_{i-1}, t_j) - 2T(x_i, t_j)}{\delta x^2} \tag{4.18}$$

where $\delta x = d/N_x$ is the spatial mesh size. Eq. (4.18) is evaluated at both t_j and t_{j+1} to transform the first term on the right-hand side of Eq. (4.17) into linear combination of temperatures at the grid points. At the two surfaces where $T(x_0, t_j)$ and $T(x_{N_x+2}, t_j)$ don't exist inside the material, fictional points were employed to apply boundary conditions.

We notice that the radiation term on the right-hand side of Eq. (4.17) includes $I_{b\lambda_m}(T)$ which is complicatedly dependent on temperature, including both T^4 factor and $f_{(\lambda_m, \lambda_{m+1})}$ which depends on temperature implicitly. However, during typical laser flash measurements, the samples were kept at the ambient temperature T_0 and would only increase at most a few kelvins in temperature. Therefore, we apply the following assumptions to simplify the calculation. Firstly, we assume that the slight temperature increase during the measurement would only negligibly affect the black body spectral radiation emission, especially at high temperatures where radiative contribution is significant and warrants the use of the current coupled conduction-radiation model, and thus the fraction function $f_{(\lambda_m, \lambda_{m+1})}$ was taken at the temperature of ambient T_0 throughout

the calculation. Secondly, we linearize the T^4 factor in $I_{b\lambda_m}(T)$ by Taylor expansion. Eq. (4.10) for $I_{b\lambda_m}(T)$ then becomes the following linear function of temperature

$$I_{b\lambda_m}(T) = \frac{{n_m}^2}{\pi}\sigma f_{(\lambda_m,\lambda_{m+1})}\left(4{T_0}^3 T - 3{T_0}^4\right) \tag{4.19}$$

The radiation term in Eq. (4.17) also includes integration over the coordinate x in evaluating ${I_m}^+(x)$ and ${I_m}^-(x)$, as shown in Eq. (4.12). The integration was transformed into a summation of multiple terms, each term represents the integration over a spatial length of δx, within which the emissive intensity was considered a constant and evaluated at the average temperature between the two adjacent grid points. the integration terms at location x_i in the forward and backward radiative intensities in Eq. (4.12) becomes

$$\kappa_m \int_0^{x_i} I_{b\lambda_m}(T_{x'}) e^{-\kappa_m(x_i - x')} dx' = \sum_{k=1}^{i-1} I_{b\lambda_m}\left(\frac{T_k + T_{k+1}}{2}\right)\left[e^{-\kappa_m(i-k-1)\delta x} - e^{-\kappa_m(i-k)\delta x}\right] \tag{4.20a}$$

$$\kappa_m \int_{x_i}^{d} I_{b\lambda_m}(T_{x'}) e^{-\kappa_m(x' - x_i)} dx' = \sum_{k=i}^{N_x} I_{b\lambda_m}\left(\frac{T_k + T_{k+1}}{2}\right)\left[e^{-\kappa_m(k-i)\delta x} - e^{-\kappa_m(k+1-i)\delta x}\right] \tag{4.20b}$$

4.3.3 Input parameters

The thermophysical properties of the material needs to be known and used as input parameters in the model, including the density, temperature-dependent specific heat capacity, refractive index, and absorption index. The density used for calculation is 2214 kg m^{-3} as provided in the product data sheet and also verified by our experimental

measurement. The specific heat capacity were obtained from Ref. [193] as shown in Figure 4.2 below.

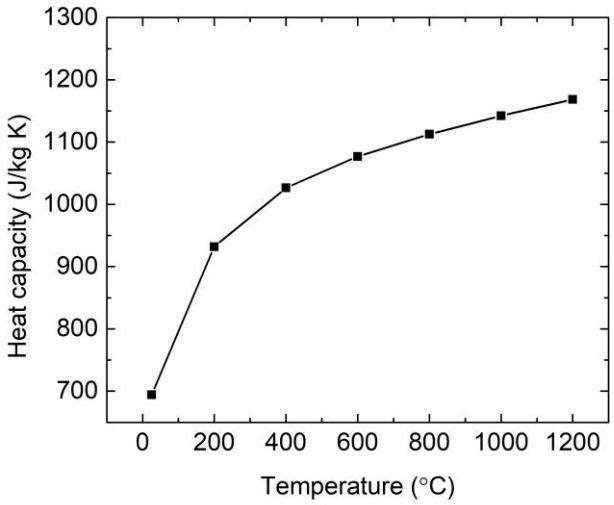

Figure 4.2: Specific heat capacity of fused quartz reported in Ref. [193] and used in this work.

The wavelength bands should also be determined for the quartz sample. In this work, 12 bands are selected such that the bands are finest at 1.5~5 μm which is the major wavelength spectrum contributing to radiative heat transfer at 1200 °C. Within each band, the refractive index and absorption coefficient were obtained by Planck average and Rosseland average methods, respectively.

The spectral absorptance of the graphite coating should also be obtained for accurate modeling of the experimental condition, which was measured as described in Section 4.2, and the results are shown in Figure 4.3, along with the gray-band emissivity ε_m and the average emissivity ε for boundary heat loss used in the model at 1200 °C. Note that both ε_m and ε are averaged using the black body emissive spectrum (Planck average)

within the wavelength band or over the entire wavelength spectrum, which means the values used in the model are changing with temperature.

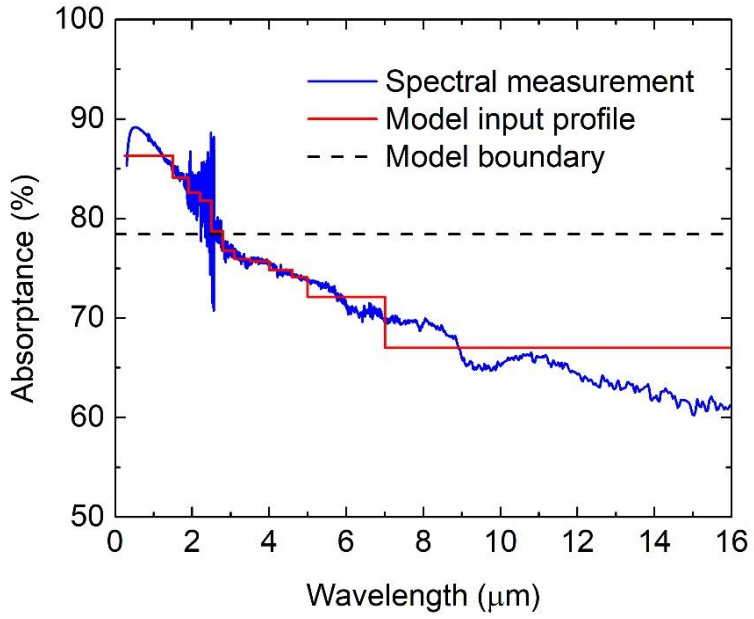

Figure 4.3: Measured spectral absorptance of graphite coating along with the gray absorption band profile and the boundary gray absorptivity used in the model

The spectral refractive index of quartz is obtained from Ref. [194] (500 nm to 5 μm) and from Ref. [195] (beyond 5 μm). Although the refractive index is expected to increase at high temperatures [194, 196, 197], the temperature coefficient is usually on the order of ~10^{-5} °C^{-1}, which results in less than 1% change for the temperature range we study, and is thus neglected.

The spectral absorption index of quartz sample is also obtained from Ref. [195]. However, we notice that the data reported in Ref. [195] has large variation. To verify the values we obtained are applicable, we also performed optical measurement on the quartz

sample. Figure 4.4 shows the spectral transmittance of the quartz sample from 2.5 μm to 16 μm measured by FTIR spectrometer.

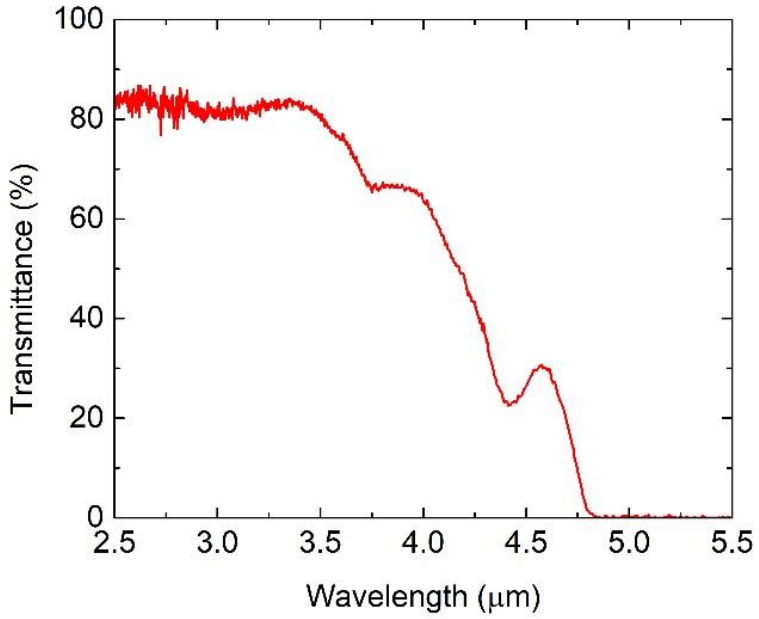

Figure 4.4: Measured spectral transmittance of the quartz sample.

According to the electromagnetic wave theory, the apparent transmittance of a slab with thickness d at one particular wavelength λ can be described by [185]

$$T_\lambda = \frac{(1-\rho)^2\tau}{1-\rho^2\tau^2} \tag{4.21}$$

where ρ is the interface reflection represented by

$$\rho = \frac{(n_\lambda - 1)^2 + {k_\lambda}^2}{(n_\lambda + 1)^2 + {k_\lambda}^2} \tag{4.22}$$

where n_λ and k_λ are the refractive index and absorption index, respectively. Under the assumption that k_λ is several orders of magnitude smaller than $(n_\lambda - 1)$, the Eq. (4.22) is simplified as

$$\rho = \frac{(n_\lambda - 1)^2}{(n_\lambda + 1)^2} \tag{4.23}$$

In Eq. (4.21), $\tau = e^{-\kappa d}$ where $\kappa = 4\pi k_\lambda / \lambda$ is the absorption coefficient. From the refractive index obtained before, ρ at each wavelength can be calculated, which is then plugged into Eq. (4.21) along with the measured transmittance data to solve for τ and eventually k_λ. The calculated absorption index is shown in Figure 4.5 which was obtained from Ref. [195], and the results are in reasonable agreement with the reference values. The profile we used in the model is also shown as red curve in Figure 4.5, which is a simplified linear connection over multiple ranges.

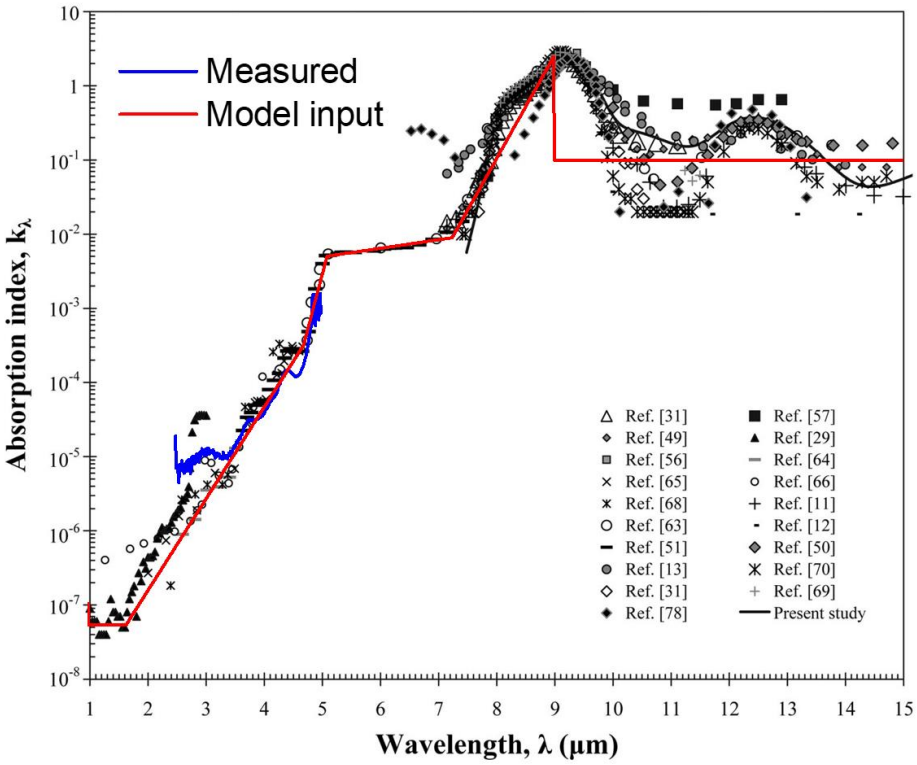

Figure 4.5: Spectral absorption index reported in Ref. [195] (black symbols), calculated from FTIR measurement (blue curve), and the profile used in the model (red curve).

We notice that the absorption index parameter reported in the literature has certain variations among different samples and different studies. It is also not in perfect agreement with the values calculated by us using the FTIR data. Moreover, the absorption index for silica is shown to change with temperature [194, 198, 199] in the near infrared spectrum, which could be changed by a few times within certain wavelength range. Therefore, we introduce an additional parameter k_f, which is the ratio of the absorption index used for calculation over the input absorption index. In other words, $k_f = 0.1$ means for the entire spectrum, the absorption index used in the coupled model calculation is 10 times smaller than the absorption index shown by the red curve in Figure 4.5.

4.3.4 Fitting principle

After the aforementioned linearization process and numerical treatments, the unknown temperature array $T(x_i, t_{j+1})$ is described by a linear system of equations, which was solved from $T(x_i, t_j)$ using linear solver from Matlab. Since the temperature varies the most at the beginning and gradually reduces its non-equilibrium, the time step was increased exponentially such that the initial time step is shortest (on the order of 1 ms) and the last time step is longest (on the order of 300 ms) to increase the calculation speed. For a given diffusivity α, the dynamic temperature rise (the thermogram) on the rear surface was calculated. The thermogram is then normalized over the maximum temperature rise and used for fitting with experimental curve, which is also normalized against the experimental maximum temperature rise.

The time range for model calculation was selected as roughly 5 times of the widely used half-rise time $t_{1/2} = 0.1388d^2/\alpha$. The time range for fitting is selected as $4t_{1/2}$. Within the fitting time range, the deviation of modeling result from experimental curve for 100 equally spaced points are evaluated, and the square of the difference between model and experiment at each of the 100 points are summarized. By sweeping the input diffusivity α over certain range, the α is obtained as the one with the smallest summation of the difference square, i.e., using the least square principle. The absorption index ratio k_f defined in the previous section is also swept over five values: 0.1, 0.32, 1, 3.2, and 10, which is equal spacing in log-scale. This allows the variation and uncertainty of the absorption index parameter to be accounted for.

4.3.5 Transparent model for LFA

In typical LFA measurement of semi-transparent samples, the transparent model [187] is applied to fit the experimental thermogram of the rear surface and obtain the thermal diffusivity of the sample. The transparent model sets the direct radiative heat transfer as an additional term on the boundary condition, and neglects the internal emission and absorption of radiation. The transparent model is also re-developed here for comparison with the coupled heat transfer model developed in this work. The exact same assumptions and numerical methods were used in the transparent model, except that the radiation source term in the governing equation is omitted, while the boundary conditions are set as

$$-k\frac{\partial T}{\partial x}\Big|_{x=0} = h(T_0 - T_{s1}) - \eta h(T_{s1} - T_{s2}) \tag{4.24a}$$

$$-k\frac{\partial T}{\partial x}\Big|_{x=d} = h(T_{s2} - T_0) - \eta h(T_{s1} - T_{s2}) \tag{4.24b}$$

where η is a transparency fitting parameter. The diffusivity and transparency parameter η are both swept over certain range to obtain the temperature rise on the rear surface of the sample, and the best fit with experimental curve (also determined by least square principle) gives the diffusivity fitted by the transparent model.

4.4 Results and discussion

Figure 4.6 shows the fitting results of the quartz sample, including the experimental rear surface thermogram of the sample captured during the laser flash measurement process, and the calculated best fit thermogram using both the transparent model and the coupled heat transfer model, from 25 °C up to 1000 °C. Each panel represents the

measurement and fitting at one temperature. The fitting results at 1200 °C are shown in Figure 4.7.

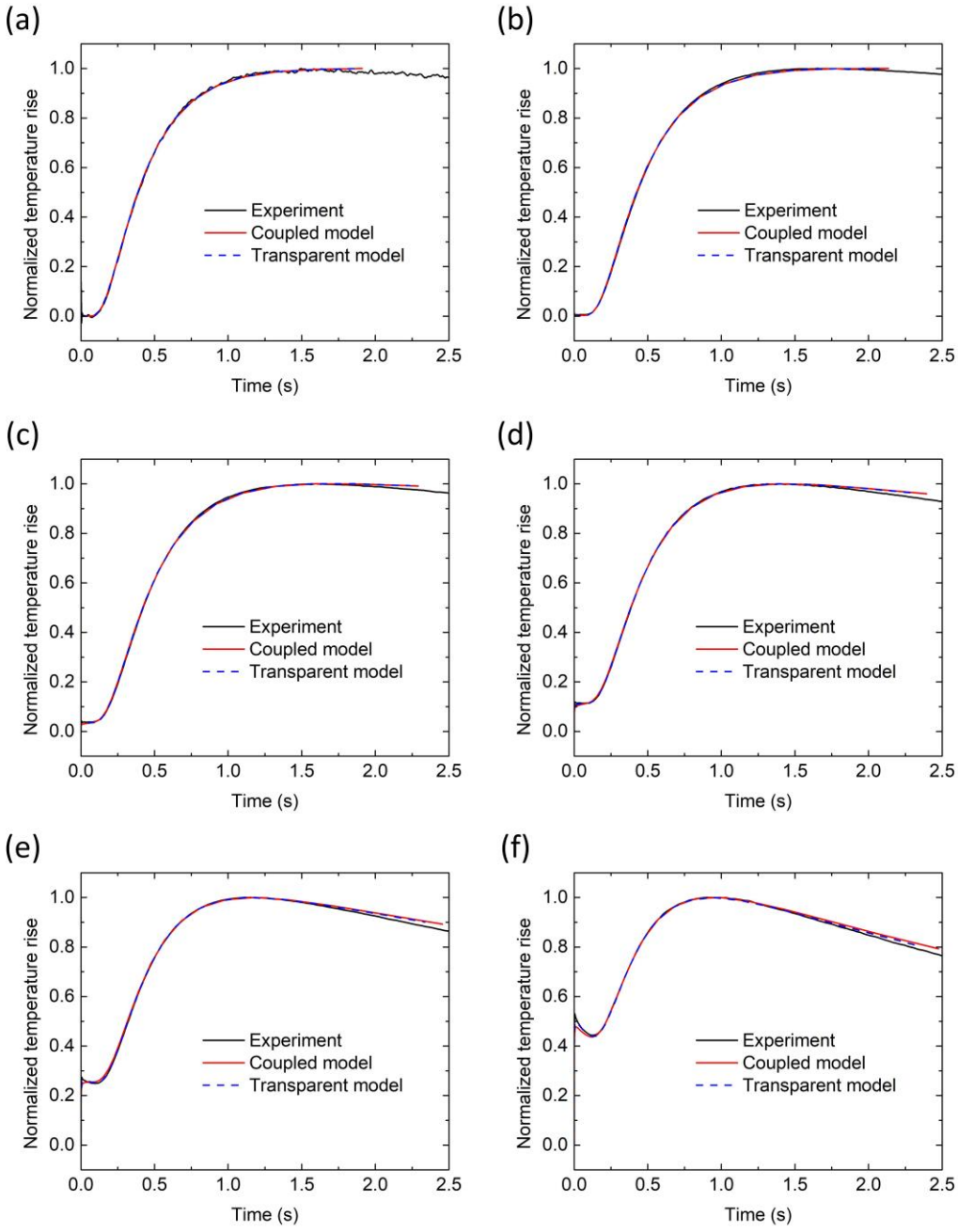

Figure 4.6: Fitting curves of the laser flash measurement experiments by transparent model and the coupled heat transfer model at (a) 25, (b) 200, (c) 400, (d) 600, (e) 800, and (f) 1000 °C.

It can be seen that generally, both the transparent model and the coupled heat transfer model fits the experimental curve well. At low temperatures (25 and 200 °C), the shape of the curve follows the traditional thermogram of LFA measurement for opaque samples, showing a gradual rise from zero up to the maximum rise with small heat loss, indicating the negligible contribution of radiation. As temperature increases over 400 °C, the shape of the curve changed into the well-known thermogram of a semitransparent material, including an initial temperature rise right after the laser pulse and a gradual smooth temperature rise later. The initial rise corresponds to the part of photons having small absorption coefficient that are emitted from the front surface, whose long mean free path exceeds the sample thickness, causing a direct transmission of radiant energy with the speed of light. The magnitude of this initial rise increases with temperature due to the increasing radiation energy and the shift of the emissive peak towards near infrared with small wavelength which has smaller absorption coefficient and larger mean free path. The later gradual rise represents the heat diffusion by phonons and short mean free path photons that were traveling diffusively. The heat loss profile at long times after the diffusion peak also becomes increasingly important at higher temperatures indicated by the faster drop in the thermograms, which is due to the radiative heat loss boundary scaling with T^3.

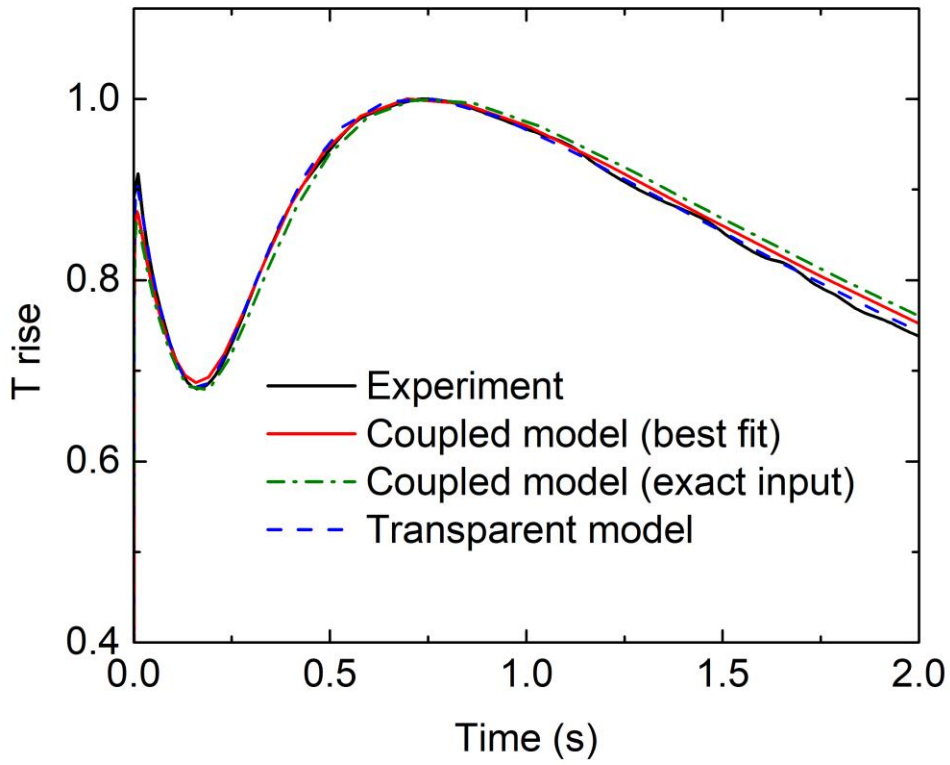

Figure 4.7: Fitting curves of the laser flash measurement experiments by transparent model and the coupled heat transfer model at 1200 °C. The fitting results of coupled model include both k_f fitted (best fit) and $k_f = 1$ (exact input) conditions.

In Figure 4.7, the thermogram at 1200 °C follows the trend described above, containing a drastic initial temperature rise, which is because silica is largely transparent for photons with wavelength ranging from 1~4 μm (indicated by the small absorption index shown in Figure 4.5) which is the dominant wavelength range for the radiation emissive power at 1200 °C. Transparent model fitted curve matches well with the experimental thermogram, with the fitted diffusivity being 0.692 $mm^2\ s^{-1}$. The fitting curve from the coupled heat transfer model were obtained for two conditions: k_f best fit and $k_f = 1$. As described in Section 4.3.4, the uncertainty in the optical properties of the sample can be

accounted for by introducing the parameter k_f as a fitting parameter, fitted from 0.1 to 10. The best fit at 1200 °C gives a diffusivity of 0.638 mm^2 s^{-1} and $k_f = 0.1$, as shown in Figure 4.7 by the red curve. To verify the possible error caused by introducing the k_f parameter, the coupled model is also used to fit the experimental curve with a fixed $k_f = 1$ representing the case when the optical properties are exactly the same as the input values shown in Figure 4.5, which gives a fitted diffusivity of 0.618 mm^2 s^{-1} shown as the green dash-dot curve. The difference in the fitted results between when k_f is fitted and when it is fixed is ~3%, which is comparable to the error caused by typical laser flash analysis [200]. For lower temperature, this difference could be even smaller since radiation is less important. Therefore, the uncertainty of the thermal diffusivity caused by introducing the k_f parameter in the coupled heat transfer model is not significant.

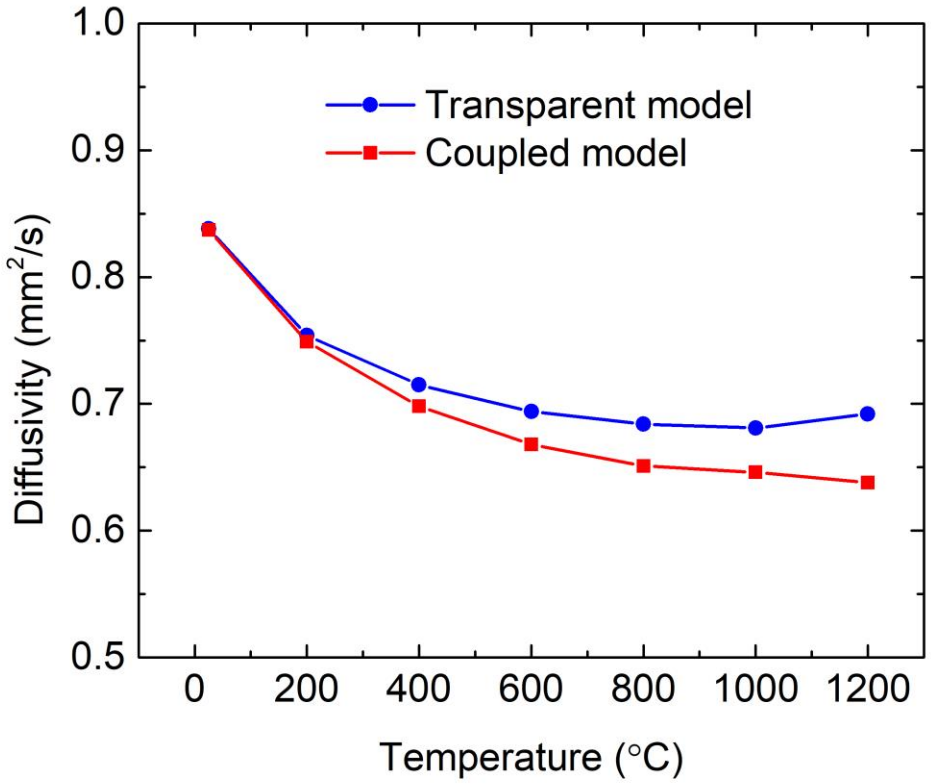

Figure 4.8: Temperature dependent thermal diffusivity of the quartz sample obtained from laser flash measurements using both the transparent model and the coupled heat transfer model.

Figure 4.8 shows the temperature dependent thermal diffusivity of the quartz sample, including the results fitted by the transparent model and by the coupled heat transfer model. At low temperatures, the fitted diffusivity results between these two models have negligible difference, with <1% for 25 and 200 °C, due to the negligible contribution from radiation. The difference increases with increasing temperature and reaches ~5% at 800 °C due to increased radiative contribution. Since the transparent model treats the radiation contribution as boundary condition and hence only exclude the radiation contribution from direct transmission of photons with mean free path much longer than the

sample thickness. Figure 4.9 shows the photon mean free path as a function of wavelength calculated from the absorption index (shown in Figure 4.5) as $l_\lambda = \lambda/4\pi k_\lambda$. The photons with wavelength of 4~8 μm have mean free path comparable to or smaller than the sample thickness ranges from tens of microns to ~1 mm, which are not excluded by the transparent model, and could contribute to the thermal diffusivity fitted by the transparent model. On the contrary, the coupled model excludes all radiation contribution and the fitted diffusivity contains only the conductive component. The difference between the thermal diffusivities obtained from the two models exceeds 8% at 1200 °C, indicating non-negligible contribution of radiation in the diffusivity obtained from the transparent model.

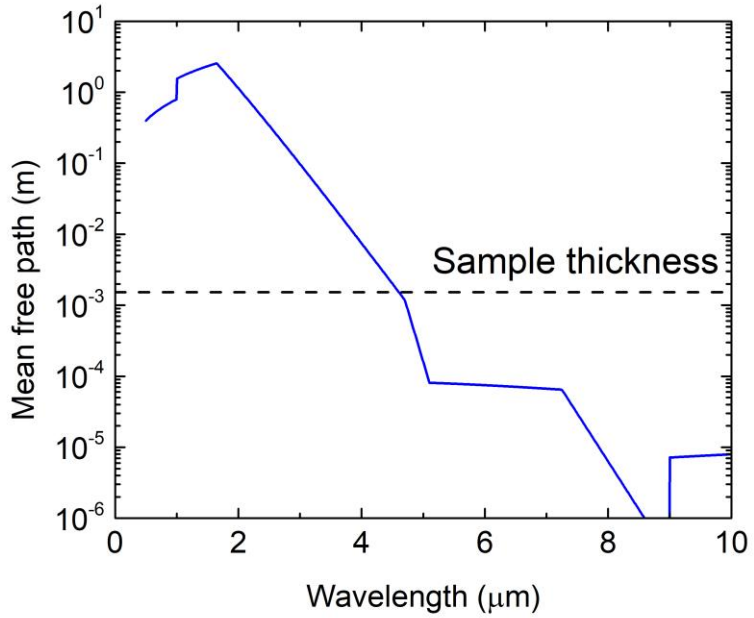

Figure 4.9: Mean free path of photons in the fused quartz sample in comparison with the sample thickness.

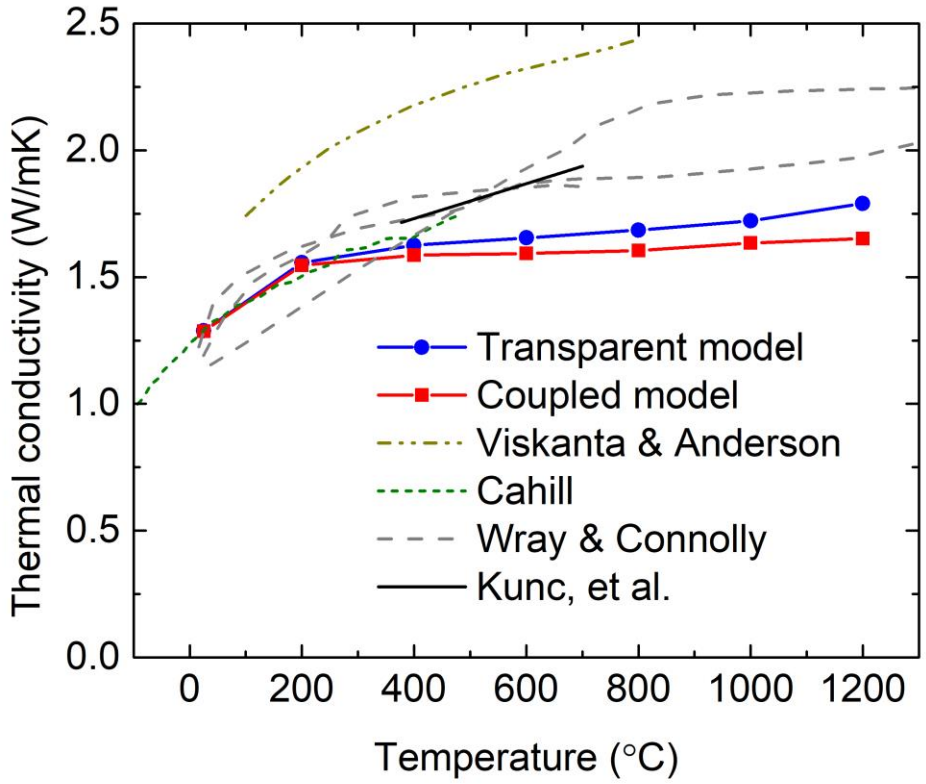

Figure 4.10: Temperature dependent thermal conductivity of the quartz sample obtained from laser flash measurements using both the transparent model and the coupled heat transfer model, along with values reported in the literature.

Figure 4.10 shows the temperature dependent thermal conductivity calculated from the diffusivity values shown in Figure 4.8 and the temperature-dependent specific heat capacity shown in Figure 4.2, along with references [201-204] reported values for the phonon thermal conductivity for various silica glass. The thermal conductivity obtained from the transparent model shows a slight increase at highest temperature, whose concavity is opposite to the trend expected for thermal conductivity of amorphous solid, indicating the radiation contribution becomes important. The coupled model fitted temperature dependent thermal conductivity follows the trend for amorphous solid, which shows a

plateau at high temperature, indicating the successful elimination of the radiative contribution. We notice that the thermal conductivity values are smaller than some of the reported values for silica, which can be attributed to the uncertainty in the determination of the sample specific heat or the intrinsic material difference. Nevertheless, using the coupled heat transfer model, we quantified the radiative contribution contained in the fitted diffusivity by the widely implemented transparent model, and identified non-negligible radiative contribution in the diffusivity at high temperatures for the quartz sample studied here.

4.5 Conclusion

In this work, we developed a coupled conduction-radiation heat transfer model to quantify the radiative heat transfer contribution in the thermal properties (thermal diffusivity and conductivity) measured by the laser flash analysis. Quartz sample was selected to demonstrate the feasibility of the model and the methodology. By fitting the experimental temperature rise profile using the coupled heat transfer model, the conductive thermal diffusivity was obtained, which eliminated the radiation contribution from internal emission and absorption within the quartz material. Compared with the widely used transparent model for extracting the purely conductive thermal diffusivity of semi-transparent materials, non-negligible radiative contribution were found to be included in the diffusivity obtained from the transparent model at high temperatures. Our model can be applied to the characterization of thermal barrier coating materials for their phonon thermal conductivity and quantification of the radiative contribution in high temperature thermal transport.

Chapter 4, in part is currently being prepared for submission for publication of the material, by Qingyang Wang, Andrew J. Wright, Jian Luo, and Renkun Chen. The dissertation author was the first author of this material.

Chapter 5 Conclusion

5.1 Summary of the dissertation

Heat transfer is critically important for a variety of energy technologies, including energy conversion, transport, storage, and utilization. Identifying and engineering the characteristic length scale of a heat transfer mode helps both the fundamental understanding of the heat transfer physics and the development of technologies for practical applications. In this dissertation, two different heat transfer modes were studied, and their respective characteristic length scales were explored. For liquid-vapor phase change heat transfer, the liquid film thickness was effectively reduced using a nanoporous membrane configuration, which resulted in superior heat transfer performance due to small conduction resistance and efficient vapor removal and liquid rewetting. For high temperature coupled conduction-radiation heat transfer in dense solids, we developed a numerical model to simulate the transient temperature rise profile during laser flash measurement, which successfully described the photon transport with different magnitudes of mean free path, and accurately obtained the conductive thermal diffusivity in high temperature laser flash measurement.

In Chapter 2, we proposed a new "*thin film boiling*" regime for the first time and realized this mechanism using a nanoporous membrane configuration. We demonstrated an unprecedentedly high CHF of over 1.23 kW cm^{-2} (demonstrated over 1.8 kW cm^{-2}) on a planar surface, which is among the highest reported values for boiling heat transfer. We further demonstrated the feasibility of reaching a higher CHF by improving the mechanical strength of the membranes. The thickness of the boiling liquid film supported by the

nanoporous membranes automatically decreases as heat flux increases. The thin film configuration reduces the conductive thermal resistance, leads to high frequency bubble departure, and provides separate liquid-vapor pathways, therefore significantly enhances the heat transfer. Our study provides a new approach to achieve ultrahigh heat flux in phase change heat transfer and will benefit both theoretical understanding and application in thermal management of high power devices of boiling heat transfer.

In Chapter 3, we systematically studied the thin film boiling and evaporation heat transfer under various working conditions for four different types of fluids (water, ethanol, IPA, FC-72), which cover a wide span of surface tension. We demonstrated the reversibility of the thin film boiling mechanism and its tunability by changing the liquid pressure. Owing this unique feature, the thermal conductance was experimentally regulated over a wide range of working conditions. We unambiguously showed the controllable transition from boiling to evaporation, when the liquid receded into the nanopores and provided additional driving force from capillary pumping sustained in the nanoscale pores. This transition was found to be universal among the four fluids examined, and the experimental results were in good agreement with a fluid transport model developed by us. Additionally, we found that the heat transfer characteristics at the transition points between boiling and evaporation were close to those of the kinetic limit of evaporation described by the Hertz-Knudsen equation. Further increase of the heat flux beyond the transition points led to decreasing HTC and deviation from the kinetic limit, which can be attributed to the increasing vapor resistance in the vapor space and inside the nanopores. This increasing vapor resistance was also confirmed by experiments on IPA with different vapor pressures. Our work could shed light on PCHT on nanoporous structures with respect to the kinetic

limit, and could advance the development of high heat-flux heat dissipation devices, especially using dielectric fluids.

In Chapter 4, a numerical model describing the transient coupled conduction-radiation heat transfer is developed to quantify the radiative contribution in the thermal properties measured by the laser flash analysis (LFA), especially at high temperatures where the radiation is contributing significantly. The conductive thermal diffusivity of quartz was obtained by fitting the experimentally measured temperature profile using the coupled heat transfer model. The model correctly eliminated the radiation contribution from internal emission and absorption within the quartz material used in this study, while the diffusivity obtained from the widely used transparent model for extracting the purely conductive thermal diffusivity of semi-transparent materials in LFA was found to include non-negligible radiation contribution at high temperatures. Our model provides a possible solution to the characterization of thermal barrier coating materials for their phonon thermal conductivity and quantification of the radiative contribution in high temperature thermal transport.

5.2 Outlook for future work

5.2.1 Thin film boiling through nanoporous membranes

Our experiments and models showed that the thin film boiling concept has its intrinsic advantages compared with traditional boiling and evaporation studied in the literature, thus it can find possible application in high heat flux thermal management and regulation in the future. However, “thin film boiling” concept is still in its infancy. Many

fundamental questions remain to be answered, and there are also plenty of opportunities existed for further improvements for practical applications.

In all our previous experiments, commercial AAO membranes with 200 nm nominal pore size was used as the nanoporous membranes, which was mainly due to its mechanical strength to the large pressure difference across it. The availability of the geometrical parameters of AAO limits the ability of performing a systematic study over various pore sizes and porosities to determine the best-performing combinations. Besides, AAO has low thermal conductivity, and it is not widely used for heat sink applications and is not easy to bond or interface with other components. Silicon has mature fabrication technology and can allow us to obtain well-defined micro- and nanostructure, but porous silicon membrane has shown to be brittle and prone to cracking when subjecting to even a small pressure difference. The material for thin film boiling application needs to be ductile to sustain high pressure difference without cracking to achieve high heat flux, while also not too soft so the deformation under pressure difference is not too severe and cause issues. Porous metal could provide a possible solution to address the need. Fabrication of porous metal using electrodeposition with sacrificial template or dealloying has been demonstrated in the literature, which provides a possible opportunity for us to explore.

From application point of view, the nanoporous membrane configuration is not practically useful in its current form. When the porous membrane is attached to a planar surface which is producing high heat flux and needs to be cooled, the pores will be blocked, which either cause large resistance for fluid transport or large resistance for vapor removal depending on the direction of the membrane attachment, making the phase change process inefficient and the cooling performance significantly deteriorated. Therefore, it is

imperative to develop a heat sink structure which could utilize the thin film boiling concept. Our proposed structure is similar to the one demonstrated by Hanks et al. [68, 205], where a nanoporous membrane is bonded on top of an open microchannel array, as also shown schematically in Figure 5.1. Liquid is pumped to flow along the microchannels, with its pressure inside the channels larger than the vapor pressure on top of the nanoporous membrane. Due to the pressure difference, liquid will flow across the membrane and flood on top of it. The heat is conducted from the substrate of the microchannel, along the ridges, towards the nanoporous membrane, and finally dissipated by thin film boiling happening on top of the membrane. With careful design of the structure, fluid property, and working conditions, the liquid film can be maintained at a small thickness and the heat sink can achieve high cooling performance. The dominant flow resistance is expected to be the flow through the membrane, since the nanopore size in the membrane is much smaller than the microchannel size. The small thickness of the nanoporous membrane can further minimize the flow resistance. Moreover, the idea of thermal regulation demonstrated in Chapter 3 could also be experimentally realized when the heat sink is properly integrated with a feedback control algorithm to dynamically change the liquid pressure inside the channel and the vapor pressure outside the membrane.

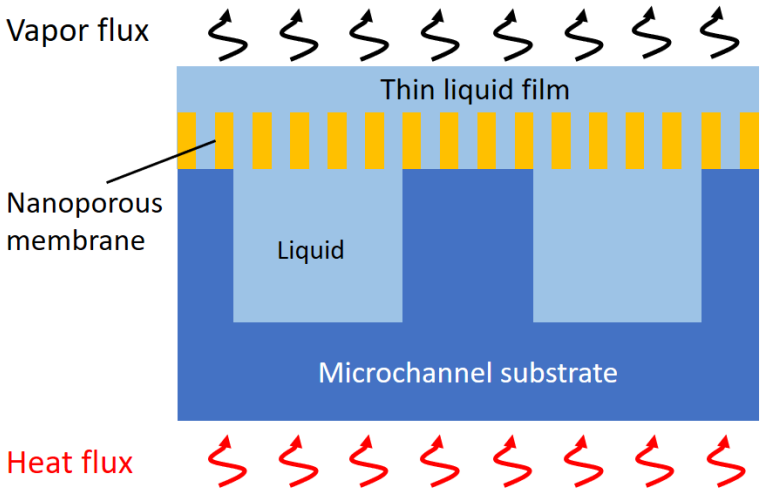

Figure 5.1: Schematic showing the microchannel heat sink implementing the thin film boiling concept

As discussed before, as of now, the heat flux of thin film boiling we demonstrated experimentally has been limited by the flow resistance. Increasing the pressure difference could drive more liquid through the membrane for vaporization, which poses demanding mechanical requirements. To reduce the pressure difference applied to the membrane while still achieve high heat flux, the flow resistance of the membrane needs to be reduced, which can be realized by either increasing the porosity or the pore size, but both could be detrimental to the mechanical property. Meanwhile, larger pore size cause larger thermal resistance for conduction inside liquid, and it also means the solid "wall thickness" between adjacent pores would be larger. For the thin liquid film to form on top of the membrane, liquid has to laterally spread over the distance of half the "wall thickness" after exiting the pores. Therefore, the interpore "wall thickness" needs to be small to reduce the lateral liquid spreading resistance and eliminate the potential dry-out. Therefore, a systematic study of the geometrical parameters of the membranes could be useful to a better understanding of the thin film boiling heat transfer.

Moreover, the thickness of the liquid is for now estimated using scaling analysis. It is interesting to know what thickness is the "cutoff" or "threshold" thickness, below which the boiling heat transfer performance is significantly enhanced. This can be realized by utilizing a hydrophobic vapor-permeable membrane, as shown schematically in Figure 5.2. The hydrophobic permeable membrane is placed above the nanoporous membrane, and the distance between the two membranes is accurately controlled using spacers. If the hydrophobic permeable membrane can block the liquid transport due to the hydrophobicity while allow the vapor to transmit through with very small resistance due to the vapor permeability, the heat transfer characteristics with well-defined liquid layer thickness can be studied by adjusting the spacer thickness. Meanwhile, a higher heat transfer performance can be expected even for small heat flux range, since the liquid layer thickness can be controlled to avoid the pool boiling regime.

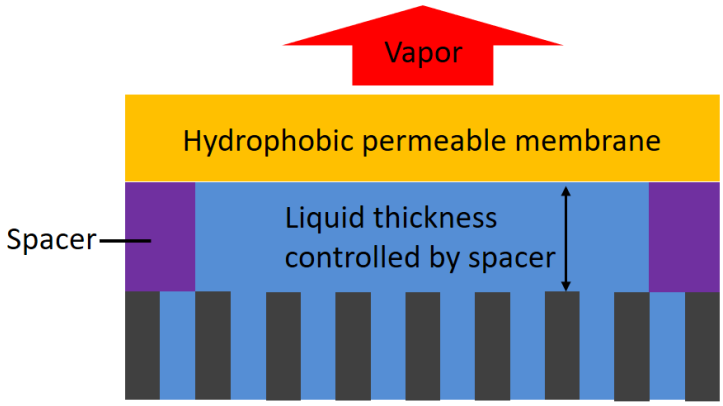

Figure 5.2: Schematic showing the concept of using hydrophobic permeable membrane to control the liquid layer thickness.

5.2.2 High temperature thermal transport

The transient coupled conduction-radiation model developed in this dissertation described in Chapter 4 successfully quantified the radiative contribution from LFA measurement of quartz. It is of greater interest to apply the model on TBC materials to obtain the conductive thermal diffusivities, since the inclusion of radiative contribution in the reported thermal properties of TBC materials has been widely observed, represented by the thermal conductivity increase at high temperatures [9, 98, 107, 108, 128]. By applying the coupled model and eliminating the radiative contribution from the thermal conductivity, the temperature-dependent phonon thermal conductivity can be obtained, which can provide a better understanding on the thermal transport property of the material systems and a better guidance on the design of new materials.

Moreover, the coupled model described in Chapter 4 is based on assumptions that might become invalid under certain conditions. One example is the non-scattering assumption, which works for the quartz sample investigated in this study, but for other samples which contains certain percentage of porosity, scattering within the media can greatly alter the radiative transport behavior. For example, the measured thermal conductivity of $La_2Zr_2O_7$ increases with temperature at high temperatures, and the increasing trend is less pronounced in samples with slight porosity compared with dense samples [206], which is due to the scattering of radiation by the pores inside the material. When thermal barrier coating materials are designed and studied, the samples used for thermal measurement, especially using laser flash analysis, are sintered into a pellet shape from synthesized particles, which could possess several percent of porosity. Therefore,

incorporating scattering of photons into the radiative source term in the model could broaden the application of the model on wider range of samples.

The coupled heat transfer model accounts for both the long mean free path photons which transfer directly from surface to surface and the short mean free path photons which travel diffusively within the material, thereby separate the radiation contribution from conduction and helps the understanding of the radiative transport by photons with different mean free paths. Based on a thorough understanding of the mean free path of photons, it is more important to engineer the mean free path of photons to realize desirable material properties. For thermal insulation applications, besides enhancing phonon scattering by increasing the disorder of the material system to reduce thermal conductivity, suppressing the radiative heat transfer can be an additional pathway to realizing high quality insulation property, especially for high temperature applications where radiation contribution is significant. For example, it has been shown that under the same boundary conditions and for the same configuration, if both conduction and radiation heat transfer occur within the TBC layer coated on a metal wall, the temperature of the metal wall can be significantly larger compared to when the TBC is opaque and only has conduction, and the heat flux transferred through the TBC layer can be twice larger than the case with opaque coating [13]. Therefore, reducing the mean free path of photons to suppress the radiative heat transfer within the material provide substantial opportunity for minimizing the total heat transfer. The mean free path of photons can be represented by the inverse of the extinction coefficient as $l_\lambda = 1/\beta_\lambda$, where the extinction coefficient β_λ is dependent on both the absorption coefficient α_λ and the scattering coefficient $\sigma_{s\lambda}$, namely, $\beta_\lambda = \alpha_\lambda + \sigma_{s\lambda}$. Therefore, the photon mean free path can be reduced by increasing either the absorption

coefficient or the scattering coefficient. Since some rare-earth ions has strong absorption in particular spectral range within the near-infrared spectrum where radiation is most dominant in the high temperature relevant to TBC applications, doping the TBC materials with these rare-earth ions can effectively increase the absorption coefficient of the material [13]. Imbedding high absorptance black particles, such as spinel oxides, can also increase the absorption of the material. Moreover, introducing pores or high reflectance metallic particles into the material can greatly increase the scattering coefficient, thereby reduce the radiative heat transfer. But of course, the pore size or particle size which should correlate with the wavelength of the photons being scattered, and the inter-pore or inter-particle distance which determines the scattering mean free path of the photons, should both be rigorously designed and experimentally verified.

Appendix

MATLAB codes for the transient temperature rise calculation in LFA measurement of quartz using the coupled conduction-radiation heat transfer model

```
%% Input numbers
d = 1.531e-3; % thickness of sample
rho = 2214; % density
Cp = 1169; % specific heat
alpha = 0.65e-6; % diffusivity
T0 = 1273; % ambient temperature
k_factor = 1; % fitting parameter
sigma_b = 5.67e-8; % S-B constant
t_pulse = 0.6e-3; % laser pulse time
q_pulse = 1e6; % laser pulse power in W/m^2
t_end = 0.1388*d^2/alpha*5; % Real time range for
calculation
delta_t_factor = 1.2; % time step ratio
N_x = 50; % number of grid for x

%% Refractive index input
wavelength_grid =
[1.5,1.9,2.2,2.5,2.8,3.1,3.5,4,4.6,5,7]*1e-6;
lamda_grid = [0.25e-6,wavelength_grid,16e-6]; % the
wavelength bands
N_lamda = length(lamda_grid);
n_lamda = zeros(1,N_lamda-1); % refractive index in each
band

%% Emissivity of coating
FTIR_data = csvread('C:\XXX\Graphit coating FTIR.CSV');
UV_vis_data = csvread('C:\XXX\Graphit coating UV-vis.csv');
epsilon =
emittance_of_coating(0.3,15,T0,FTIR_data,UV_vis_data);
h0 = 4*epsilon*sigma_b*T0^3; % HTC of radiative heat loss

%% Variables for calculation
k_c = alpha*rho*Cp;
delta_x = d/N_x;

delta_t_0 = t_end/1.2/N_x^2;
N_t_approx = log(1.2*N_x^2*(delta_t_factor-
1)+1)/log(delta_t_factor);
N_t = round(N_t_approx);
```

```
T_mat = zeros(N_x+1, N_t+1)+T0; % temperature matrix

delta_t = zeros(1,N_t);
delta_t(1) = delta_t_0;
for k=2:N_t
   delta_t(k) = delta_t(k-1)*delta_t_factor;
end

t_array = zeros(N_t+1,1);
t_sum = 0;
for i=1:N_t
    t_sum = t_sum+delta_t(i);
    t_array(i+1) = t_sum;
end

%% Optical property variable array calculation
kappa_lamda = zeros(1,N_lamda-1);
numerator = zeros(1,N_lamda-1);
denominator = zeros(1,N_lamda-1);
fraction = zeros(1,N_lamda-1);
I_tot = integral(@(w) i_b(w,T0), 0, Inf);
eps = zeros(1,N_lamda-1); % emissivity of each band

for m=1:(N_lamda-1)
    % Planck mean n
    n_lamda(m) = integral(@(w)
n_of_SiO2(w.*1e6).*i_b(w,T0),lamda_grid(m),lamda_grid(m+1))
        ./ integral(@(w)
i_b(w,T0),lamda_grid(m),lamda_grid(m+1));
    % Rosseland mean kappa
    numerator(m) = integral(@(w)
i_b_over_T(w,T0),lamda_grid(m),lamda_grid(m+1));
    denominator(m) = integral(@(w)
w./4./pi./k_of_SiO2(w.*1e6).*i_b_over_T(w,T0),lamda_grid(m)
,lamda_grid(m+1));

    kappa_lamda(m) = numerator(m)/denominator(m)*k_factor;
    fraction(m) = integral(@(w)
i_b(w,T0),lamda_grid(m),lamda_grid(m+1))/I_tot;

    eps(m) =
emittance_of_coating(lamda_grid(m)*1e6,lamda_grid(m+1)*1e6,
T0,FTIR_data,UV_vis_data);
end

%% Initial temperature condition
```

```
for i=1:(N_x+1)% front side, semi-infinite with constant
heat flux
    T_mat(i,1) =
T0+q_pulse/k_c*((4*alpha*t_pulse)^(1/2)*exp(-((i-
1)*delta_x)^2/4/alpha/t_pulse)...
        -(i-1)*delta_x*erfc((i-
1)*delta_x/sqrt(4*alpha*t_pulse)));
end

%% Coefficient for fictional points
A = zeros(N_x,N_lamda-1); % the coefficient for I_fwd
B = zeros(1,N_lamda-1);
C = zeros(1,N_lamda-1); % i_b(m,T) = B(m)*T + C(m)
E = zeros(1,N_lamda-1); % exp(-kappa_lamda(m)*delta_x*N_x)
P = zeros(1,N_lamda-1); % 1/(1-(1-eps)^2*exp^2)

for m=1:(N_lamda-1)
    for i=1:N_x
        A(i,m) = exp(-kappa_lamda(m)*delta_x*(N_x-i))-exp(-
kappa_lamda(m)*delta_x*(N_x+1-i));
    end
    B(m) = n_lamda(m)^2*sigma_b*fraction(m)*4*T0^3;
    C(m) = -n_lamda(m)^2*sigma_b*fraction(m)*3*T0^4;
    E(m) = exp(-kappa_lamda(m)*delta_x*N_x);
    P(m) = 1/(1-(1-eps(m))^2*E(m)^2);
end

Coefficient_1 = zeros(1,N_x+1); % the coefficients for T
array in T_fictional_1
Coefficient_2 = zeros(1,N_x+1); % the coefficients for T
array in T_fictional_2
Constant_var = 0;

for m=1:(N_lamda-1)
    Coefficient_1(N_x+1) =
Coefficient_1(N_x+1)+2*delta_x/k_c*eps(m)*P(m)*B(m)*(eps(m)
*E(m)+(1-eps(m))*E(m)*A(N_x,m)/2+A(1,m)/2);
    Coefficient_2(1) =
Coefficient_2(1)+2*delta_x/k_c*eps(m)*P(m)*B(m)*(eps(m)*E(m
)+(1-eps(m))*E(m)*A(N_x,m)/2+A(1,m)/2);
    for i=2:N_x
        Coefficient_1(i) =
Coefficient_1(i)+delta_x/k_c*eps(m)*P(m)*B(m)*(A(N_x-
i+2,m)+A(N_x-i+1,m)+(1-eps(m))*E(m)*(A(i-1,m)+A(i,m)));
        Coefficient_2(i) =
Coefficient_2(i)+delta_x/k_c*eps(m)*P(m)*B(m)*(A(i-
1,m)+A(i,m)+(1-eps(m))*E(m)*(A(N_x-i+2,m)+A(N_x-i+1,m)));
```

```
    end
    Coefficient_1(1) =
Coefficient_1(1)+2*delta_x/k_c*B(m)*eps(m)*(P(m)*((1-
eps(m))*eps(m)*E(m)^2+(1-eps(m))*E(m)*A(1,m)/2+A(N_x,m)/2)-
1);
    Coefficient_2(N_x+1) =
Coefficient_2(N_x+1)+2*delta_x/k_c*B(m)*eps(m)*(P(m)*((1-
eps(m))*eps(m)*E(m)^2+(1-eps(m))*E(m)*A(1,m)/2+A(N_x,m)/2)-
1);
    Constant_var =
Constant_var+2*delta_x/k_c*eps(m)*C(m)*(P(m)*(eps(m)*E(m)+(
1-eps(m))*eps(m)*E(m)^2+(1-eps(m))*E(m)*(1-E(m))+(1-E(m)))-
1);
end
Coefficient_1(2) = Coefficient_1(2)+1;
Coefficient_2(N_x) = Coefficient_2(N_x)+1;
Coefficient_1(1) = Coefficient_1(1)-2*delta_x/k_c*h0;
Coefficient_2(N_x+1) = Coefficient_2(N_x+1)-
2*delta_x/k_c*h0;
Constant = Constant_var + 2*delta_x/k_c*h0*T0;

T_fictional_mat = zeros(2,N_t+1); % fictional points of
temperature
T_fictional_mat(1,1) = Coefficient_1*T_mat(:,1)+Constant;
T_fictional_mat(2,1) = Coefficient_2*T_mat(:,1)+Constant;

%% Formal calculation
fprintf("Total steps: %d\n",N_t);
for j = 1:N_t
    fprintf("j=%d: ",j);

    Matrix = zeros(N_x+1,N_x+1); % Matrix A on the left
side of the equation
    Vector = zeros(N_x+1,1); % right side of the equation
Ax=b
    for i=1:(N_x+1)
        Matrix(1,i) = -k_c/2/delta_x^2*Coefficient_1(i);
        Matrix(N_x+1,i) = -
k_c/2/delta_x^2*Coefficient_2(i);
    end
    Matrix(1,1) =
Matrix(1,1)+rho*Cp/delta_t(j)+k_c/delta_x^2;
    Matrix(1,2) = Matrix(1,2)-k_c/2/delta_x^2;
    Matrix(N_x+1,N_x) = Matrix(N_x+1,N_x)-k_c/2/delta_x^2;
    Matrix(N_x+1,N_x+1) =
Matrix(N_x+1,N_x+1)+rho*Cp/delta_t(j)+k_c/delta_x^2;
    Vector(1) = rho*Cp*T_mat(1,j)/delta_t(j)...
```

```
        +k_c/2*(T_fictional_mat(1,j)+T_mat(2,j)-
2*T_mat(1,j))/delta_x^2 ...
        -div_q_rad(1,j)+k_c/2/delta_x^2*Constant;
    Vector(N_x+1) = rho*Cp*T_mat(N_x+1,j)/delta_t(j)...
        +k_c/2*(T_fictional_mat(2,j)+T_mat(N_x,j)-
2*T_mat(N_x+1,j))/delta_x^2 ...
        -div_q_rad(N_x+1,j)+k_c/2/delta_x^2*Constant;

    for i=2:N_x
        Matrix(i,i-1) = -k_c/2/delta_x^2;
        Matrix(i,i+1) = -k_c/2/delta_x^2;
        Matrix(i,i) = rho*Cp/delta_t(j)+k_c/delta_x^2;
        Vector(i) = rho*Cp*T_mat(i,j)/delta_t(j)...
            +k_c/2*(T_mat(i+1,j)+T_mat(i-1,j)-
2*T_mat(i,j))/delta_x^2 ...
            -div_q_rad(i,j);
    end

    T_new = Matrix\Vector; % linsolve(Matrix,Vector);
    T_mat(:,j+1) = T_new;

% Iteration for div_q_rad to average the radiation term at
the current time step with that at the next time step
    Vector(1) = rho*Cp*T_mat(1,j)/delta_t(j)...
        +k_c/2*(T_fictional_mat(1,j)+T_mat(2,j)-
2*T_mat(1,j))/delta_x^2 ...
        -
(div_q_rad(1,j)+div_q_rad(1,j+1))/2+k_c/2/delta_x^2*Constan
t;
    Vector(N_x+1) = rho*Cp*T_mat(N_x+1,j)/delta_t(j)...
        +k_c/2*(T_fictional_mat(2,j)+T_mat(N_x,j)-
2*T_mat(N_x+1,j))/delta_x^2 ...
        -
(div_q_rad(N_x+1,j)+div_q_rad(N_x+1,j+1))/2+k_c/2/delta_x^2
*Constant;
    for i=2:N_x
        Vector(i) = rho*Cp*T_mat(i,j)/delta_t(j)...
            +k_c/2*(T_mat(i+1,j)+T_mat(i-1,j)-
2*T_mat(i,j))/delta_x^2 ...
            -(div_q_rad(i,j)+div_q_rad(i,j+1))/2;
    end
    T_new_1 = Matrix\Vector;
    T_mat(:,j+1) = T_new_1;
    while sum(abs(T_new_1./T_new-1))>(1e-8*N_x)
        T_new = T_new_1;
        Vector(1) = rho*Cp*T_mat(1,j)/delta_t(j)...
```

```
            +k_c/2*(T_fictional_mat(1,j)+T_mat(2,j)-
2*T_mat(1,j))/delta_x^2 ...
            -
(div_q_rad(1,j)+div_q_rad(1,j+1))/2+k_c/2/delta_x^2*Constan
t;
        Vector(N_x+1) = rho*Cp*T_mat(N_x+1,j)/delta_t(j)...
            +k_c/2*(T_fictional_mat(2,j)+T_mat(N_x,j)-
2*T_mat(N_x+1,j))/delta_x^2 ...
            -
(div_q_rad(N_x+1,j)+div_q_rad(N_x+1,j+1))/2+k_c/2/delta_x^2
*Constant;
        for i=2:N_x
            Vector(i) = rho*Cp*T_mat(i,j)/delta_t(j)...
                +k_c/2*(T_mat(i+1,j)+T_mat(i-1,j)-
2*T_mat(i,j))/delta_x^2 ...
                -(div_q_rad(i,j)+div_q_rad(i,j+1))/2;
        end
        T_new_1 = Matrix\Vector;
    end
    T_mat(:,j+1) = T_new_1;
    T_fictional_mat(1,j+1) =
Coefficient_1*T_new_1+Constant;
    T_fictional_mat(2,j+1) =
Coefficient_2*T_new_1+Constant;

    fprintf("T_rise=%.4f\n",T_new_1(N_x+1)-T0);
end

T_rise = T_mat(N_x+1,:)'-T0;
T_max = max(T_rise);
T_rise_non = T_rise./T_max; % dimensionless temperature
rise
fprintf("\nCalculation Finished.\n\n");
plot(t_array, T_rise_non);
```

```
function a_eff = emittance_of_coating(w1, w2, T0,
FTIR_data, UV_vis_data)
% Planck averaged absorptance (=emittance) between
wavelengths w1 and w2 based on measurement results from
FTIR and UV-vis spectrometers

lamda_IR = 10000./FTIR_data(:,1); % unit in um
Ref_IR = FTIR_data(:,2)./100; % reflectance
lamda_vis = UV_vis_data(:,1)./1000; % unit in um
Ref_vis = UV_vis_data(:,2)./100;

N_lamda_span = 2000;
lamda_span = linspace(0.2,17,N_lamda_span);
a_span = zeros(0,N_lamda_span);
N1 = 0;
N2 = 0;
for i=1:N_lamda_span
    lamda = lamda_span(i);
    if lamda<=2.5
        R = interp1(lamda_vis,Ref_vis,lamda);
    elseif lamda<15
        R = interp1(lamda_IR,Ref_IR,lamda);
    end
    a_span(i) = 1-R;
    if lamda<=w1 && lamda_span(i+1)>w1
        N1 = i;
    end
    if i>1
        if lamda_span(i-1)<w2 && lamda>=w2
        N2 = i-1;
        end
    end
end

Tot = integral(@(w) i_b(w,T0),lamda_span(N1)*1e-
6,lamda_span(N2+1)*1e-6);
sum = 0;
for i=N1:N2
    lamda1 = lamda_span(i)*1e-6;
    lamda2 = lamda_span(i+1)*1e-6;
    a_ave = (a_span(i)+a_span(i+1))/2;
    sum = sum + integral(@(w)
a_ave.*i_b(w,T0),lamda1,lamda2);
end
a_eff = sum/Tot;
end
```

```
function i_b = i_b(lamda,T) % directional black body
emissive intensity
% equals to the spectral form of sigma_b*T^4 divided by pi

h = 6.62607004e-34;
c = 299792458;
kB = 1.38064852e-23;
i_b = 2.*h.*c.^2./lamda.^5./(exp(h.*c./lamda./kB./T)-1);

end
```

```
function i_b_over_T = i_b_over_T(lamda,T)
% Partial derivative of black body emissive intensity over
temperature

h = 6.62607004e-34;
c = 299792458;
kB = 1.38064852e-23;
i_b_over_T =
(2.*h.*c.^2).*(h.*c./kB).*exp(h.*c./lamda./kB./T)./lamda.^6
./T.^2./(exp(h.*c./lamda./kB./T)-1).^2;

end
```

Bibliography

[1] D.G. Cahill, W.K. Ford, K.E. Goodson, G.D. Mahan, A. Majumdar, H.J. Maris, R. Merlin, S.R. Phillpot, Nanoscale thermal transport, Journal of applied physics, 93(2) (2003) 793-818.

[2] D.G. Cahill, P.V. Braun, G. Chen, D.R. Clarke, S. Fan, K.E. Goodson, P. Keblinski, W.P. King, G.D. Mahan, A. Majumdar, Nanoscale thermal transport. II. 2003–2012, Applied physics reviews, 1(1) (2014) 011305.

[3] G. Chen, Nanoscale energy transport and conversion: a parallel treatment of electrons, molecules, phonons, and photons, Oxford University Press, 2005.

[4] C.L. Tien, Microscale energy transfer, CRC Press, 1997.

[5] Z.M. Zhang, Nano/microscale heat transfer, 2007.

[6] T.S. Fisher, Thermal energy at the nanoscale, World Scientific Publishing Company, 2013.

[7] A.I. Hochbaum, R. Chen, R.D. Delgado, W. Liang, E.C. Garnett, M. Najarian, A. Majumdar, P. Yang, Enhanced thermoelectric performance of rough silicon nanowires, Nature, 451(7175) (2008) 163-167.

[8] A.J. Wright, Q. Wang, S.-T. Ko, K.M. Chung, R. Chen, J. Luo, Size disorder as a descriptor for predicting reduced thermal conductivity in medium-and high-entropy pyrochlore oxides, Scripta Materialia, 181 (2020) 76-81.

[9] A.J. Wright, Q. Wang, C. Huang, A. Nieto, R. Chen, J. Luo, From High-Entropy Ceramics to Compositionally-Complex Ceramics: A Case Study of Fluorite Oxides, Journal of the European Ceramic Society, (2020).

[10] G.P. Srivastava, Theory of Thermal Conduction in Nonmetals, MRS Bulletin, 26(6) (2011) 445-450.

[11] C. Dames, Ultrahigh thermal conductivity confirmed in boron arsenide, Science, 361(6402) (2018) 549-550.

[12] J. Plawsky, A. Fedorov, S. Garimella, H. Ma, S. Maroo, L. Chen, Y. Nam, Nano-and microstructures for thin-film evaporation—A review, Nanoscale and microscale thermophysical engineering, 18(3) (2014) 251-269.

[13] Q. Flamant, D.R. Clarke, Opportunities for minimizing radiative heat transfer in future thermal and environmental barrier coatings, Scripta Materialia, 173 (2019) 26-31.

[14] R. Siegel, C. M. Spuckler, Analysis of thermal radiation effects on temperatures in turbine engine thermal barrier coatings, Materials Science and Engineering: A, 245(2) (1998) 150-159.

[15] G. Ni, G. Li, S.V. Boriskina, H.X. Li, W.L. Yang, T.J. Zhang, G. Chen, Steam generation under one sun enabled by a floating structure with thermal concentration, Nat Energy, 1 (2016).

[16] H. Ghasemi, G. Ni, A.M. Marconnet, J. Loomis, S. Yerci, N. Miljkovic, G. Chen, Solar steam generation by heat localization, Nat Commun, 5 (2014).

[17] I.U. Vakarelski, N.A. Patankar, J.O. Marston, D.Y.C. Chan, S.T. Thoroddsen, Stabilization of Leidenfrost vapour layer by textured superhydrophobic surfaces, Nature, 489(7415) (2012) 274-277.

[18] H.J. Cho, D.J. Preston, Y.Y. Zhu, E.N. Wang, Nanoengineered materials for liquid-vapour phase-change heat transfer, Nat Rev Mater, 2(2) (2017).

[19] N.S. Dhillon, J. Buongiorno, K.K. Varanasi, Critical heat flux maxima during boiling crisis on textured surfaces, Nat Commun, 6 (2015).

[20] D. Li, G.S. Wu, W. Wang, Y.D. Wang, D. Liu, D.C. Zhang, Y.F. Chen, G.P. Peterson, R.G. Yang, Enhancing Flow Boiling Heat Transfer in Microchannels for Thermal Management with Monolithically-Integrated Silicon Nanowires, Nano Lett, 12(7) (2012) 3385-3390.

[21] H.J. Cho, J.P. Mizerak, E.N. Wang, Turning bubbles on and off during boiling using charged surfactants, Nat Commun, 6 (2015).

[22] R. Chen, M.-C. Lu, V. Srinivasan, Z. Wang, H.H. Cho, A. Majumdar, Nanowires for enhanced boiling heat transfer, Nano letters, 9(2) (2009) 548-553.

[23] J. Zeng, Q. Wang, Y. Shi, P. Liu, R. Chen, Osmotic Pumping and Salt Rejection by Polyelectrolyte Hydrogel for Continuous Solar Desalination, Advanced Energy Materials, 9(38) (2019) 1900552.

[24] A. Bar-Cohen, K. Matin, N. Jankowski, D. Sharar, Two-Phase Thermal Ground Planes: Technology Development and Parametric Results, Journal of Electronic Packaging, 137(1) (2014) 010801.

[25] S.V. Garimella, T. Persoons, J.A. Weibel, V. Gektin, Electronics thermal management in information and communications technologies: Challenges and future directions, IEEE Transactions on Components, Packaging and Manufacturing Technology, 7(8) (2016) 1191-1205.

[26] E. Pop, Energy dissipation and transport in nanoscale devices, Nano Research, 3(3) (2010) 147-169.

[27] K.R. Bagnall, Device-level thermal analysis of GaN-based electronics, Massachusetts Institute of Technology, 2013.

[28] Y. Won, J. Cho, D. Agonafer, M. Asheghi, K.E. Goodson, Cooling limits for GaN HEMT technology, in: 2013 IEEE Compound Semiconductor Integrated Circuit Symposium (CSICS), IEEE, 2013, pp. 1-5.

[29] H.J. Cho, D.J. Preston, Y. Zhu, E.N. Wang, Nanoengineered materials for liquid–vapour phase-change heat transfer, Nature Reviews Materials, 2(2) (2017) 16092.

[30] M.-C. Lu, R. Chen, V. Srinivasan, V.P. Carey, A. Majumdar, Critical heat flux of pool boiling on Si nanowire array-coated surfaces, International Journal of Heat and Mass Transfer, 54(25) (2011) 5359-5367.

[31] Y. Liu, J. Tang, L. Li, Y.N. Shek, D. Xu, Design of Cassie-wetting nucleation sites in pool boiling, International Journal of Heat and Mass Transfer, 132 (2019) 25-33.

[32] Y. Liu, M.-C. Lu, D. Xu, The suppression effect of easy-to-activate nucleation sites on the critical heat flux in pool boiling, International Journal of Thermal Sciences, 129 (2018) 231-237.

[33] S. Shin, G. Choi, B. Rallabandi, D. Lee, D.I. Shim, B.S. Kim, K.M. Kim, H.H. Cho, Enhanced Boiling Heat Transfer using Self-Actuated Nanobimorphs, Nano letters, 18(10) (2018) 6392-6396.

[34] P. Raghupathi, S. Kandlikar, Pool boiling enhancement through contact line augmentation, Applied Physics Letters, 110(20) (2017) 204101.

[35] A. Zou, D.P. Singh, S.C. Maroo, Early evaporation of microlayer for boiling heat transfer enhancement, Langmuir : the ACS journal of surfaces and colloids, 32(42) (2016) 10808-10814.

[36] S.G. Kandlikar, Enhanced Macroconvection Mechanism With Separate Liquid–Vapor Pathways to Improve Pool Boiling Performance, Journal of Heat Transfer, 139(5) (2017) 051501.

[37] R. Wen, Q. Li, W. Wang, B. Latour, C.H. Li, C. Li, Y.-C. Lee, R. Yang, Enhanced bubble nucleation and liquid rewetting for highly efficient boiling heat transfer on two-level hierarchical surfaces with patterned copper nanowire arrays, Nano Energy, 38 (2017) 59-65.

[38] T.P. Allred, J.A. Weibel, S.V. Garimella, Enabling Highly Effective Boiling from Superhydrophobic Surfaces, Physical review letters, 120(17) (2018) 174501.

[39] A.R. Betz, J. Xu, H. Qiu, D. Attinger, Do surfaces with mixed hydrophilic and hydrophobic areas enhance pool boiling?, Applied Physics Letters, 97(14) (2010) 141909.

[40] X. Dai, P. Wang, F. Yang, X. Li, C. Li, Decoupling the influence of surface structure and intrinsic wettability on boiling heat transfer, Applied Physics Letters, 112(25) (2018) 253901.

[41] C. Li, Z. Wang, P.I. Wang, Y. Peles, N. Koratkar, G. Peterson, Nanostructured copper interfaces for enhanced boiling, small, 4(8) (2008) 1084-1088.

[42] K.-H. Chu, R. Enright, E.N. Wang, Structured surfaces for enhanced pool boiling heat transfer, Applied Physics Letters, 100(24) (2012) 241603.

[43] S.G. Kandlikar, Controlling bubble motion over heated surface through evaporation momentum force to enhance pool boiling heat transfer, Applied Physics Letters, 102(5) (2013) 051611.

[44] H. Lee, T. Maitra, J. Palko, D. Kong, C. Zhang, M.T. Barako, Y. Won, M. Asheghi, K.E. Goodson, Enhanced Heat Transfer Using Microporous Copper Inverse Opals, Journal of Electronic Packaging, 140(2) (2018).

[45] A. Jaikumar, T. Emery, S. Kandlikar, Interplay between developing flow length and bubble departure diameter during macroconvection enhanced pool boiling, Applied Physics Letters, 112(7) (2018) 071603.

[46] M.M. Rahman, J. Pollack, M. McCarthy, Increasing Boiling Heat Transfer using Low Conductivity Materials, Scientific reports, 5 (2015) 13145.

[47] A. Jaikumar, S.G. Kandlikar, Pool boiling enhancement through bubble induced convective liquid flow in feeder microchannels, Applied Physics Letters, 108(4) (2016) 041604.

[48] J.W. Palko, H. Lee, C. Zhang, T.J. Dusseault, T. Maitra, Y. Won, D.D. Agonafer, J. Moss, F. Houshmand, G. Rong, Extreme Two-Phase Cooling from Laser-Etched Diamond and Conformal, Template-Fabricated Microporous Copper, Advanced Functional Materials, 27(45) (2017).

[49] A. Fazeli, S. Moghaddam, A New Paradigm for Understanding and Enhancing the Critical Heat Flux (CHF) Limit, Scientific reports, 7(1) (2017) 5184.

[50] H. Seo, J.H. Chu, S.-Y. Kwon, I.C. Bang, Pool boiling CHF of reduced graphene oxide, graphene, and SiC-coated surfaces under highly wettable FC-72, International Journal of Heat and Mass Transfer, 82 (2015) 490-502.

[51] S.J. Thiagarajan, R. Yang, C. King, S. Narumanchi, Bubble dynamics and nucleate pool boiling heat transfer on microporous copper surfaces, International Journal of Heat and Mass Transfer, 89 (2015) 1297-1315.

[52] F. Yang, X. Dai, C.-J. Kuo, Y. Peles, J. Khan, C. Li, Enhanced flow boiling in microchannels by self-sustained high frequency two-phase oscillations, International Journal of Heat and Mass Transfer, 58(1-2) (2013) 402-412.

[53] Y. Zhu, D.S. Antao, K.-H. Chu, S. Chen, T.J. Hendricks, T. Zhang, E.N. Wang, Surface Structure Enhanced Microchannel Flow Boiling, Journal of Heat Transfer, 138(9) (2016) 091501.

[54] W. Li, X. Qu, T. Alam, F. Yang, W. Chang, J. Khan, C. Li, Enhanced flow boiling in microchannels through integrating multiple micro-nozzles and reentry microcavities, Applied Physics Letters, 110(1) (2017) 014104.

[55] T. Zhang, Y. Peles, J.T. Wen, T. Tong, J.-Y. Chang, R. Prasher, M.K. Jensen, Analysis and active control of pressure-drop flow instabilities in boiling microchannel systems, International Journal of Heat and Mass Transfer, 53(11-12) (2010) 2347-2360.

[56] J. Ma, W. Li, C. Ren, J.A. Khan, C. Li, Realizing highly coordinated, rapid and sustainable nucleate boiling in microchannels on HFE-7100, International Journal of Heat and Mass Transfer, 133 (2019) 1219-1229.

[57] C. Woodcock, C. Ng'oma, M. Sweet, Y. Wang, Y. Peles, J. Plawsky, Ultra-high heat flux dissipation with Piranha Pin Fins, International Journal of Heat and Mass Transfer, 128 (2019) 504-515.

[58] K.P. Drummond, D. Back, M.D. Sinanis, D.B. Janes, D. Peroulis, J.A. Weibel, S.V. Garimella, Characterization of hierarchical manifold microchannel heat sink arrays under simultaneous background and hotspot heating conditions, International Journal of Heat and Mass Transfer, 126 (2018) 1289-1301.

[59] X. Dai, M. Famouri, A.I. Abdulagatov, R. Yang, Y.-C. Lee, S.M. George, C. Li, Capillary evaporation on micromembrane-enhanced microchannel wicks with atomic layer deposited silica, Applied Physics Letters, 103(15) (2013) 151602.

[60] X. Dai, F. Yang, R. Yang, Y.-C. Lee, C. Li, Micromembrane-enhanced capillary evaporation, International Journal of Heat and Mass Transfer, 64 (2013) 1101-1108.

[61] X. Dai, F. Yang, R. Yang, X. Huang, W.A. Rigdon, X. Li, C. Li, Biphilic nanoporous surfaces enabled exceptional drag reduction and capillary evaporation enhancement, Applied Physics Letters, 105(19) (2014) 191611.

[62] R. Wen, S. Xu, Y.-C. Lee, R. Yang, Capillary-Driven Liquid Film Boiling Heat Transfer on Hybrid Mesh Wicking Structures, Nano Energy, (2018).

[63] R. Xiao, S.C. Maroo, E.N. Wang, Negative pressures in nanoporous membranes for thin film evaporation, Applied Physics Letters, 102(12) (2013) 123103.

[64] D.F. Hanks, Z. Lu, S. Narayanan, K.R. Bagnall, R. Raj, R. Xiao, R. Enright, E.N. Wang, Nanoporous evaporative device for advanced electronics thermal management, in: Thermal and Thermomechanical Phenomena in Electronic Systems (ITherm), 2014 IEEE Intersociety Conference on, IEEE, 2014, pp. 290-295.

[65] Z. Lu, S. Narayanan, E.N. Wang, Modeling of Evaporation from Nanopores with Nonequilibrium and Nonlocal Effects, Langmuir : the ACS journal of surfaces and colloids, 31(36) (2015) 9817-9824.

[66] Z. Lu, K.L. Wilke, D.J. Preston, I. Kinefuchi, E. Chang-Davidson, E.N. Wang, An Ultrathin Nanoporous Membrane Evaporator, Nano letters, 17(10) (2017) 6217-6220.

[67] K.L. Wilke, B. Barabadi, Z. Lu, T. Zhang, E.N. Wang, Parametric study of thin film evaporation from nanoporous membranes, Applied Physics Letters, 111(17) (2017) 171603.

[68] D.F. Hanks, Z. Lu, J. Sircar, T.R. Salamon, D.S. Antao, K.R. Bagnall, B. Barabadi, E.N. Wang, Nanoporous membrane device for ultra high heat flux thermal management, Microsystems & Nanoengineering, 4(1) (2018) 1.

[69] J.W. Palko, H. Lee, C. Zhang, T.J. Dusseault, T. Maitra, Y. Won, D.D. Agonafer, J. Moss, F. Houshmand, G.G. Rong, J.D. Wilbur, D. Rockosi, I. Mykyta, D. Resler, D. Altman, M. Asheghi, J.G. Santiago, K.E. Goodson, Extreme Two-Phase Cooling from Laser-Etched Diamond and Conformal, Template-Fabricated Microporous Copper, Advanced Functional Materials, 27(45) (2017).

[70] F. Abe, Research and Development of Heat-Resistant Materials for Advanced USC Power Plants with Steam Temperatures of 700 degrees C and Above, Engineering, 1(2) (2015) 211-224.

[71] R. Viswanathan, K. Coleman, U. Rao, Materials for ultra-supercritical coal-fired power plant boilers, Int J Pres Ves Pip, 83(11-12) (2006) 778-783.

[72] M. Mehos, C. Turchi, J. Vidal, M. Wagner, Z. Ma, C. Ho, W. Kolb, C. Andraka, A. Kruizenga, Concentrating Solar Power Gen3 Demonstration Roadmap, National Renewable Energy Laboratory, Golden, CO, 2017.

[73] J.H. Perepezko, The Hotter the Engine, the Better, Science, 326(5956) (2009) 1068-1069.

[74] W.C. Chueh, C. Falter, M. Abbott, D. Scipio, P. Furler, S.M. Haile, A. Steinfeld, High-Flux Solar-Driven Thermochemical Dissociation of CO2 and H2O Using Nonstoichiometric Ceria, Science, 330(6012) (2010) 1797-1801.

[75] S. Zhai, J. Rojas, N. Ahlborg, K. Lim, M.F. Toney, H.Y. Jin, W.C. Chueh, A. Majumdar, The use of poly-cation oxides to lower the temperature of two-step thermochemical water splitting, Energ Environ Sci, 11(8) (2018) 2172-2178.

[76] E.D. Wachsman, K.T. Lee, Lowering the Temperature of Solid Oxide Fuel Cells, Science, 334(6058) (2011) 935-939.

[77] Z. Gao, L.V. Mogni, E.C. Miller, J.G. Railsback, S.A. Barnett, A perspective on low-temperature solid oxide fuel cells, Energ Environ Sci, 9(5) (2016) 1602-1644.

[78] Y. Chen, Y. Chen, D. Ding, Y. Ding, Y. Choi, L. Zhang, S. Yoo, D.C. Chen, B. Deglee, H. Xu, Q.Y. Lu, B.T. Zhao, G. Vardar, J.Y. Wang, H. Bluhm, E.J. Crumlin, C.H. Yang, J. Liu, B. Yildiz, M.L. Liu, A robust and active hybrid catalyst for facile oxygen reduction in solid oxide fuel cells, Energ Environ Sci, 10(4) (2017) 964-971.

[79] G.J. Snyder, E.S. Toberer, Complex thermoelectric materials, Nat Mater, 7(2) (2008) 105-114.

[80] A. Fiorino, L.X. Zhu, D. Thompson, R. Mittapally, P. Reddy, E. Meyhofer, Nanogap near-field thermophotovoltaics, Nat Nanotechnol, 13(9) (2018) 806-+.

[81] A. Lenert, D.M. Bierman, Y. Nam, W.R. Chan, I. Celanovic, M. Soljacic, E.N. Wang, A nanophotonic solar thermophotovoltaic device, Nat Nanotechnol, 9(2) (2014) 126-130.

[82] J.W. Schwede, I. Bargatin, D.C. Riley, B.E. Hardin, S.J. Rosenthal, Y. Sun, F. Schmitt, P. Pianetta, R.T. Howe, Z.X. Shen, N.A. Melosh, Photon-enhanced thermionic emission for solar concentrator systems, Nat Mater, 9(9) (2010) 762-767.

[83] A. Henry, R. Prasher, The prospect of high temperature solid state energy conversion to reduce the cost of concentrated solar power, Energ Environ Sci, 7(6) (2014) 1819-1828.

[84] G. Xiao, G.H. Zheng, M. Qiu, Q. Li, D.S. Li, M.J. Ni, Thermionic energy conversion for concentrating solar power, Appl Energ, 208 (2017) 1318-1342.

[85] K.A.A. Khalid, T.J. Leong, K. Mohamed, Review on Thermionic Energy Converters, Ieee T Electron Dev, 63(6) (2016) 2231-2241.

[86] K.F. Mustafa, S. Abdullah, M.Z. Abdullah, K. Sopian, A review of combustion-driven thermoelectric (TE) and thermophotovoltaic (TPV) power systems, Renew Sust Energ Rev, 71 (2017) 572-584.

[87] A. Datas, A. Marti, Thermophotovoltaic energy in space applications: Review and future potential, Sol Energ Mat Sol C, 161 (2017) 285-296.

[88] Fitriani, R. Ovik, B.D. Long, M.C. Barma, M. Riaz, M.F.M. Sabri, S.M. Said, R. Saidur, A review on nanostructures of high-temperature thermoelectric materials for waste heat recovery, Renew Sust Energ Rev, 64 (2016) 635-659.

[89] D.R. Clarke, M. Oechsner, N.P. Padture, Thermal-barrier coatings for more efficient gas-turbine engines, MRS Bulletin, 37(10) (2012) 891-898.

[90] W. Pan, S.R. Phillpot, C. Wan, A. Chernatynskiy, Z. Qu, Low thermal conductivity oxides, MRS Bulletin, 37(10) (2012) 917-922.

[91] C. Degueldre, P. Tissot, H. Lartigue, M. Pouchon, Specific heat capacity and Debye temperature of zirconia and its solid solution, Thermochim Acta, 403(2) (2003) 267-273.

[92] D.R. Clarke, M. Oechsner, N.P. Padture, Thermal-barrier coatings for more efficient gas-turbine engines, Mrs Bull, 37(10) (2012) 891-902.

[93] J.P. Goff, W. Hayes, S. Hull, M.T. Hutchings, K.N. Clausen, Defect structure of yttria-stabilized zirconia and its influence on the ionic conductivity at elevated temperatures, Physical Review B, 59(22) (1999) 14202-14219.

[94] S. Xiwen, X. Min, Z. Fen, J. Guixiao, H. Xihong, A. Shengli, High-temperature thermal properties of yttria fully stabilized zirconia ceramics, Journal of Rare Earths, 29(2) (2011) 155-159.

[95] J. Feng, X. Ren, X. Wang, R. Zhou, W. Pan, Thermal conductivity of ytterbia-stabilized zirconia, Scripta Materialia, 66(1) (2012) 41-44.

[96] J. Wu, N.P. Padture, P.G. Klemens, M. Gell, E. García, P. Miranzo, M.I. Osendi, Thermal conductivity of ceramics in the ZrO2-GdO1.5system, Journal of Materials Research, 17(12) (2011) 3193-3200.

[97] M. Rahaman, J. Gross, R. Dutton, H. Wang, Phase stability, sintering, and thermal conductivity of plasma-sprayed ZrO2–Gd2O3 compositions for potential thermal barrier coating applications, Acta Materialia, 54(6) (2006) 1615-1621.

[98] M.R. Winter, D.R. Clarke, Oxide Materials with Low Thermal Conductivity, Journal of the American Ceramic Society, 90(2) (2007) 533-540.

[99] M.R. Winter, D.R. Clarke, Thermal conductivity of yttria-stabilized zirconia–hafnia solid solutions, Acta Materialia, 54(19) (2006) 5051-5059.

[100] M. Zhao, X. Ren, J. Yang, W. Pan, Thermo-mechanical properties of ThO2-doped Y2O3 stabilized ZrO2 for thermal barrier coatings, Ceramics International, 42(1) (2016) 501-508.

[101] S. Raghavan, H. Wang, W. Porter, R. Dinwiddie, M. Mayo, Thermal properties of zirconia co-doped with trivalent and pentavalent oxides, Acta Materialia, 49(1) (2001) 169-179.

[102] S. Raghavan, H. Wang, R.B. Dinwiddie, W.D. Porter, R. Vaβen, D. Stöver, M.J. Mayo, Ta2O5/Nb2O5 and Y2O3 Co-doped Zirconias for Thermal Barrier Coatings, Journal of the American Ceramic Society, 87(3) (2004) 431-437.

[103] J. Gild, M. Samiee, J.L. Braun, T. Harrington, H. Vega, P.E. Hopkins, K. Vecchio, J. Luo, High-entropy fluorite oxides, Journal of the European Ceramic Society, 38(10) (2018) 3578-3584.

[104] N.P. Bansal, D.M. Zhu, Effects of doping on thermal conductivity of pyrochlore oxides for advanced thermal barrier coatings, Mat Sci Eng a-Struct, 459(1-2) (2007) 192-195.

[105] J. Feng, B. Xiao, R. Zhou, W. Pan, Thermal conductivity of rare earth zirconate pyrochlore from first principles, Scripta Materialia, 68(9) (2013) 727-730.

[106] C.L. Wan, W. Pan, Q. Xu, Y.X. Qin, J.D. Wang, Z.X. Qu, M.H. Fang, Effect of point defects on the thermal transport properties of(LaxGd1−x)2Zr2O7: Experiment and theoretical model, Physical Review B, 74(14) (2006).

[107] Z.-G. Liu, J.-H. Ouyang, Y. Zhou, Preparation and thermophysical properties of (NdxGd1−x)2Zr2O7 ceramics, Journal of Materials Science, 43(10) (2008) 3596-3603.

[108] Z.-G. Liu, J.-H. Ouyang, Y. Zhou, Structural evolution and thermophysical properties of (SmxGd1−x)2Zr2O7 (0≤x≤1.0) ceramics, Journal of Alloys and Compounds, 472(1-2) (2009) 319-324.

[109] C. Wan, Z. Qu, A. Du, W. Pan, Order-Disorder Transition and Unconventional Thermal Conductivities of the (Sm1−xYbx)2Zr2O7 Series, Journal of the American Ceramic Society, 94(2) (2011) 592-596.

[110] C. Wan, W. Zhang, Y. Wang, Z. Qu, A. Du, R. Wu, W. Pan, Glass-like thermal conductivity in ytterbium-doped lanthanum zirconate pyrochlore, Acta Materialia, 58(18) (2010) 6166-6172.

[111] C. Wan, Z. Qu, A. Du, W. Pan, Influence of B site substituent Ti on the structure and thermophysical properties of A2B2O7-type pyrochlore Gd2Zr2O7, Acta Materialia, 57(16) (2009) 4782-4789.

[112] M. Zhao, W. Pan, C. Wan, Z. Qu, Z. Li, J. Yang, Defect engineering in development of low thermal conductivity materials: A review, Journal of the European Ceramic Society, 37(1) (2017) 1-13.

[113] B. Liu, Y. Liu, C. Zhu, H. Xiang, H. Chen, L. Sun, Y. Gao, Y. Zhou, Advances on strategies for searching for next generation thermal barrier coating materials, Journal of Materials Science & Technology, 35(5) (2019) 833-851.

[114] P.K. Schelling, S.R. Phillpot, R.W. Grimes, Optimum pyrochlore compositions for low thermal conductivity, Philosophical Magazine Letters, 84(2) (2004) 127-137.

[115] X. Cao, R. Vassen, W. Fischer, F. Tietz, W. Jungen, D. Stoever, Lanthanum–cerium oxide as a thermal barrier-coating material for high-temperature applications, Advanced materials, 15(17) (2003) 1438-1442.

[116] J. Feng, B. Xiao, R. Zhou, W. Pan, Thermal expansion and conductivity of RE2Sn2O7 (RE=La, Nd, Sm, Gd, Er and Yb) pyrochlores, Scripta Materialia, 69(5) (2013) 401-404.

[117] W. Ma, D.E. Mack, R. Vaßen, D. Stöver, Perovskite-Type Strontium Zirconate as a New Material for Thermal Barrier Coatings, Journal of the American Ceramic Society, 91(8) (2008) 2630-2635.

[118] W. Ma, M.O. Jarligo, D.E. Mack, D. Pitzer, J. Malzbender, R. Vaßen, D. Stöver, New Generation Perovskite Thermal Barrier Coating Materials, Journal of Thermal Spray Technology, 17(5-6) (2008) 831-837.

[119] M.O. Jarligo, D.E. Mack, R. Vassen, D. Stöver, Application of Plasma-Sprayed Complex Perovskites as Thermal Barrier Coatings, Journal of Thermal Spray Technology, 18(2) (2009) 187-193.

[120] C. Wan, Z. Qu, Y. He, D. Luan, W. Pan, Ultralow thermal conductivity in highly anion-defective aluminates, Phys Rev Lett, 101(8) (2008) 085901.

[121] C. Wan, T.D. Sparks, P. Wei, D.R. Clarke, Thermal Conductivity of the Rare-Earth Strontium Aluminates, Journal of the American Ceramic Society, (2010).

[122] Y. Shen, D.R. Clarke, P.A. Fuierer, Anisotropic thermal conductivity of the aurivillus phase, bismuth titanate (Bi 4 Ti 3 O 12): A natural nanostructured superlattice, Applied Physics Letters, 93(10) (2008) 102907.

[123] M.T. Agne, R. Hanus, G.J. Snyder, Minimum thermal conductivity in the context of diffuson-mediated thermal transport, Energy & Environmental Science, 11(3) (2018) 609-616.

[124] S. Mukhopadhyay, D.S. Parker, B.C. Sales, A.A. Puretzky, M.A. McGuire, L. Lindsay, Two-channel model for ultralow thermal conductivity of crystalline Tl3VSe4, Science, 360(6396) (2018) 1455-1458.

[125] Y. Luo, X. Yang, T. Feng, J. Wang, X. Ruan, Vibrational hierarchy leads to dual-phonon transport in low thermal conductivity crystals, Nature Communications, 11(1) (2020) 1-10.

[126] J.M. Larkin, A.J.H. McGaughey, Thermal conductivity accumulation in amorphous silica and amorphous silicon, Phys Rev B, 89(14) (2014).

[127] X. Wang, H. Xiang, X. Sun, J. Liu, F. Hou, Y. Zhou, Thermal properties of a prospective thermal barrier material: Yb3Al5O12, Journal of Materials Research, 29(22) (2014) 2673-2681.

[128] A. Du, C. Wan, Z. Qu, W. Pan, Thermal Conductivity of Monazite-Type REPO4(RE=La, Ce, Nd, Sm, Eu, Gd), Journal of the American Ceramic Society, 92(11) (2009) 2687-2692.

[129] Z. Qu, T.D. Sparks, W. Pan, D.R. Clarke, Thermal conductivity of the gadolinium calcium silicate apatites: Effect of different point defect types, Acta Materialia, 59(10) (2011) 3841-3850.

[130] Z. Tian, L. Zheng, Z. Li, J. Li, J. Wang, Exploration of the low thermal conductivities of γ-Y2Si2O7, β-Y2Si2O7, β-Yb2Si2O7, and β-Lu2Si2O7 as novel environmental barrier coating candidates, Journal of the European Ceramic Society, 36(11) (2016) 2813-2823.

[131] Z. Tian, L. Zheng, J. Wang, P. Wan, J. Li, J. Wang, Theoretical and experimental determination of the major thermo-mechanical properties of RE 2 SiO 5 (RE = Tb, Dy, Ho, Er, Tm, Yb, Lu, and Y) for environmental and thermal barrier coating applications, Journal of the European Ceramic Society, 36(1) (2016) 189-202.

[132] J.-W. Yeh, S.-J. Lin, T.-S. Chin, J.-Y. Gan, S.-K. Chen, T.-T. Shun, C.-H. Tsau, S.-Y. Chou, Formation of simple crystal structures in Cu-Co-Ni-Cr-Al-Fe-Ti-V alloys with multiprincipal metallic elements, Metallurgical and Materials Transactions A, 35(8) (2004) 2533-2536.

[133] B. Cantor, I.T.H. Chang, P. Knight, A.J.B. Vincent, Microstructural development in equiatomic multicomponent alloys, Materials Science and Engineering: A, 375-377 (2004) 213-218.

[134] C.M. Rost, E. Sachet, T. Borman, A. Moballegh, E.C. Dickey, D. Hou, J.L. Jones, S. Curtarolo, J.P. Maria, Entropy-stabilized oxides, Nat Commun, 6 (2015) 8485.

[135] J. Gild, Y. Zhang, T. Harrington, S. Jiang, T. Hu, M.C. Quinn, W.M. Mellor, N. Zhou, K. Vecchio, J. Luo, High-Entropy Metal Diborides: A New Class of High-Entropy Materials and a New Type of Ultrahigh Temperature Ceramics, Scientific reports, 6 (2016) 37946.

[136] S. Jiang, T. Hu, J. Gild, N. Zhou, J. Nie, M. Qin, T. Harrington, K. Vecchio, J. Luo, A new class of high-entropy perovskite oxides, Scripta Materialia, 142 (2018) 116-120.

[137] J. Dąbrowa, M. Stygar, A. Mikuła, A. Knapik, K. Mroczka, W. Tejchman, M. Danielewski, M. Martin, Synthesis and microstructure of the (Co,Cr,Fe,Mn,Ni) 3 O 4 high entropy oxide characterized by spinel structure, Materials Letters, 216 (2018) 32-36.

[138] T.J. Harrington, J. Gild, P. Sarker, C. Toher, C.M. Rost, O.F. Dippo, C. McElfresh, K. Kaufmann, E. Marin, L. Borowski, P.E. Hopkins, J. Luo, S. Curtarolo, D.W. Brenner, K.S. Vecchio, Phase stability and mechanical properties of novel high entropy transition metal carbides, Acta Materialia, 166 (2019) 271-280.

[139] X. Yan, L. Constantin, Y. Lu, J.F. Silvain, M. Nastasi, B. Cui, (Hf0.2Zr0.2Ta0.2Nb0.2Ti0.2)C high-entropy ceramics with low thermal conductivity, Journal of the American Ceramic Society, 101(10) (2018) 4486-4491.

[140] Y. Qin, J.-X. Liu, F. Li, X. Wei, H. Wu, G.-J. Zhang, A high entropy silicide by reactive spark plasma sintering, Journal of Advanced Ceramics, 8(1) (2019) 148-152.

[141] J. Gild, J. Braun, K. Kaufmann, E. Marin, T. Harrington, P. Hopkins, K. Vecchio, J. Luo, A high-entropy silicide: (Mo0.2Nb0.2Ta0.2Ti0.2W0.2)Si2, Journal of Materiomics, (2019).

[142] K.P. Chen, X.T. Pei, L. Tang, H.R. Cheng, Z.M. Li, C.W. Li, X.W. Zhang, L.A. An, A five-component entropy-stabilized fluorite oxide, J Eur Ceram Soc, 38(11) (2018) 4161-4164.

[143] X. Ren, Z. Tian, J. Zhang, J. Wang, Equiatomic quaternary (Y1/4Ho1/4Er1/4Yb1/4) 2SiO5 silicate: A perspective multifunctional thermal and environmental barrier coating material, Scripta Materialia, 168 (2019) 47-50.

[144] Z. Zhao, H. Xiang, F.-Z. Dai, Z. Peng, Y. Zhou, (La0. 2Ce0. 2Nd0. 2Sm0. 2Eu0. 2) 2Zr2O7: A novel high-entropy ceramic with low thermal conductivity and sluggish grain growth rate, Journal of Materials Science & Technology, (2019).

[145] J.L. Braun, C.M. Rost, M. Lim, A. Giri, D.H. Olson, G.N. Kotsonis, G. Stan, D.W. Brenner, J.P. Maria, P.E. Hopkins, Charge-Induced Disorder Controls the Thermal Conductivity of Entropy-Stabilized Oxides, Advanced materials, 30(51) (2018) e1805004.

[146] J. Yang, X. Qian, W. Pan, R. Yang, Z. Li, Y. Han, M. Zhao, M. Huang, C. Wan, Diffused Lattice Vibration and Ultralow Thermal Conductivity in the Binary Ln-Nb-O Oxide System, Advanced materials, 31(24) (2019) e1808222.

[147] Q. Wang, Y. Shi, R. Chen, Transition between thin film boiling and evaporation on nanoporous membranes near the kinetic limit, International Journal of Heat and Mass Transfer, 154 (2020) 119673.

[148] S. Shin, Q. Wang, J. Luo, R. Chen, Advanced Materials for High-Temperature Thermal Transport, Advanced Functional Materials, (2019) 1904815.

[149] I. Mudawar, Assessment of high-heat-flux thermal management schemes, IEEE Transactions on Components and Packaging Technologies, 24(2) (2001) 122-141.

[150] S.V. Garimella, V. Singhal, D. Liu, On-chip thermal management with microchannel heat sinks and integrated micropumps, Proceedings of the IEEE, 94(8) (2006) 1534-1548.

[151] V.P. Carey, Liquid-vapor phase-change phenomena, (1992).

[152] A.R. Betz, J. Jenkins, C.-J.C. Kim, D. Attinger, Boiling heat transfer on superhydrophilic, superhydrophobic, and superbiphilic surfaces, International Journal of Heat and Mass Transfer, 57(2) (2013) 733-741.

[153] B.S. Kim, H. Lee, S. Shin, G. Choi, H.H. Cho, Interfacial wicking dynamics and its impact on critical heat flux of boiling heat transfer, Applied Physics Letters, 105(19) (2014) 191601.

[154] Y.X. Li, K. Zhang, M.C. Lu, C.H. Duan, Single bubble dynamics on superheated superhydrophobic surfaces, International Journal of Heat and Mass Transfer, 99 (2016) 521-531.

[155] A. Kalani, S.G. Kandlikar, Combining liquid inertia with pressure recovery from bubble expansion for enhanced flow boiling, Applied Physics Letters, 107(18) (2015) 181601.

[156] D.a. Ćoso, V. Srinivasan, M.-C. Lu, J.-Y. Chang, A. Majumdar, Enhanced Heat Transfer in Biporous Wicks in the Thin Liquid Film Evaporation and Boiling Regimes, Journal of Heat Transfer, 134(10) (2012) 101501.

[157] K. Wilke, Evaporation from Nanoporous Membranes, Master's thesis, Massachusetts Institute of Technology, Cambridge, 2016.

[158] A.F. Mills, C. Coimbra, Basic heat transfer, Temporal Publishing, LLC, 2015.

[159] A. Jaikumar, S.G. Kandlikar, Pool boiling inversion through bubble induced macroconvection, Applied Physics Letters, 110(9) (2017) 094107.

[160] Y. Hsu, On the size range of active nucleation cavities on a heating surface, Journal of Heat Transfer, 84(3) (1962) 207-213.

[161] C. Tien, A hydrodynamic model for nucleate pool boiling, International Journal of Heat and Mass Transfer, 5(6) (1962) 533-540.

[162] Y. Nam, S. Sharratt, G. Cha, Y.S. Ju, Characterization and Modeling of the Heat Transfer Performance of Nanostructured Cu Micropost Wicks, Journal of Heat Transfer, 133(10) (2011) 101502.

[163] J.W. Palko, C. Zhang, J.D. Wilbur, T.J. Dusseault, M. Asheghi, K.E. Goodson, J.G. Santiago, Approaching the limits of two-phase boiling heat transfer: High heat flux and low superheat, Applied Physics Letters, 107(25) (2015) 253903.

[164] C.-J. Kuo, Y. Peles, Flow boiling instabilities in microchannels and means for mitigation by reentrant cavities, Journal of Heat Transfer, 130(7) (2008) 072402.

[165] T. Zhang, T. Tong, J.-Y. Chang, Y. Peles, R. Prasher, M.K. Jensen, J.T. Wen, P. Phelan, Ledinegg instability in microchannels, International Journal of Heat and Mass Transfer, 52(25-26) (2009) 5661-5674.

[166] S. Narayanan, A.G. Fedorov, Y.K. Joshi, Interfacial transport of evaporating water confined in nanopores, Langmuir : the ACS journal of surfaces and colloids, 27(17) (2011) 10666-10676.

[167] Y. Li, M.A. Alibakhshi, Y. Zhao, C. Duan, Exploring Ultimate Water Capillary Evaporation in Nanoscale Conduits, Nano Letters, (2017).

[168] W. Gambill, J. Lienhard, An upper bound for the critical boiling heat flux, ASME J. Heat Transfer, 111(3) (1989) 815-818.

[169] D. Labuntsov, A. Kryukov, Analysis of intensive evaporation and condensation, International Journal of Heat and Mass Transfer, 22(7) (1979) 989-1002.

[170] H. Wang, S.V. Garimella, J.Y. Murthy, Characteristics of an evaporating thin film in a microchannel, International Journal of Heat and Mass Transfer, 50(19-20) (2007) 3933-3942.

[171] H.K. Dhavaleswarapu, S.V. Garimella, J.Y. Murthy, Microscale temperature measurements near the triple line of an evaporating thin liquid film, Journal of Heat Transfer, 131(6) (2009) 061501.

[172] Q. Wang, R. Chen, Ultrahigh Flux Thin Film Boiling Heat Transfer Through Nanoporous Membranes, Nano Letters, 18(5) (2018) 3096-3103.

[173] Z. Lu, I. Kinefuchi, K.L. Wilke, G. Vaartstra, E.N. Wang, A unified relationship for evaporation kinetics at low Mach numbers, Nature Communications, 10(1) (2019) 2368.

[174] Y. Li, H. Chen, S. Xiao, M.A. Alibakhshi, C.-W. Lo, M.-C. Lu, C. Duan, Ultrafast Diameter-Dependent Water Evaporation from Nanopores, ACS nano, 13(3) (2019) 3363-3372.

[175] C. Kruse, A. Tsubaki, C. Zuhlke, T. Anderson, D. Alexander, G. Gogos, S. Ndao, Secondary pool boiling effects, Applied Physics Letters, 108(5) (2016) 051602.

[176] A. Kalani, S.G. Kandlikar, Enhanced pool boiling with ethanol at subatmospheric pressures for electronics cooling, Journal of Heat Transfer, 135(11) (2013) 111002.

[177] T. Borca-Tasciuc, A. Kumar, G. Chen, Data reduction in 3ω method for thin-film thermal conductivity determination, Review of scientific instruments, 72(4) (2001) 2139-2147.

[178] V.P. Carey, Liquid-vapor Phase-change Phenomena: An Introduction to the Thermophysics of Vaporization and Condensation Processes in Heat Transfert Equipment, Hemisphere publishing corporation, 1992.

[179] Z. Lu, T.R. Salamon, S. Narayanan, K.R. Bagnall, D.F. Hanks, D.S. Antao, B. Barabadi, J. Sircar, M.E. Simon, E.N. Wang, Design and modeling of membrane-based evaporative cooling devices for thermal management of high heat fluxes, IEEE Transactions on Components, Packaging and Manufacturing Technology, 6(7) (2016) 1056-1065.

[180] M.S. El-Genk, J.L. Parker, Nucleate boiling of FC-72 and HFE-7100 on porous graphite at different orientations and liquid subcooling, Energy Conversion and Management, 49(4) (2008) 733-750.

[181] Z.W. Liu , W.W. Lin , D.J. Lee, X.F. Peng Pool Boiling of FC-72 and HFE-7100, Journal of Heat Transfer, 123(2) (1999) 399-400.

[182] Q. Wang, R. Chen, Widely tunable thin film boiling heat transfer through nanoporous membranes, Nano Energy, 54 (2018) 297-303.

[183] A.J. Wright, J. Luo, A step forward from high-entropy ceramics to compositionally complex ceramics: a new perspective, Journal of Materials Science, (2020).

[184] C. Oses, C. Toher, S. Curtarolo, High-entropy ceramics, Nature Reviews Materials, 5(4) (2020) 295-309.

[185] M.F. Modest, Radiative heat transfer, Academic press, 2013.

[186] M. Lazard, S. André, D. Maillet, Diffusivity measurement of semi-transparent media: model of the coupled transient heat transfer and experiments on glass, silica glass and zinc selenide, International journal of heat and mass transfer, 47(3) (2004) 477-487.

[187] H. Mehling, G. Hautzinger, O. Nilsson, J. Fricke, R. Hofmann, O. Hahn, Thermal diffusivity of semitransparent materials determined by the laser-flash method applying a new analytical model, International Journal of Thermophysics, 19(3) (1998) 941-949.

[188] T. Heping, B. Maestre, M. Lallemand, Transient and steady-state combined heat transfer in semi-transparent materials subjected to a pulse or a step irradiation, (1991).

[189] A. Degiovanni, B. Remy, S. Andre, Transient radiation-conductive heat transfer problems:"the quadrupole method", Journal of thermal science, 11(4) (2002) 359-371.

[190] H. Tan, L. Ruan, X. Xia, Q. Yu, T.W. Tong, Transient coupled radiative and conductive heat transfer in an absorbing, emitting and scattering medium, International journal of heat and mass transfer, 42(15) (1999) 2967-2980.

[191] O. Hahn, F. Raether, M. Arduini-Schuster, J. Fricke, Transient coupled conductive/radiative heat transfer in absorbing, emitting and scattering media: application to laser-flash measurements on ceramic materials, International journal of heat and mass transfer, 40(3) (1997) 689-698.

[192] S. Andre, A. Degiovanni, A theoretical study of the transient coupled conduction and radiation heat transfer in glass: phonic diffusivity measurements by the flash technique, International journal of heat and mass transfer, 38(18) (1995) 3401-3412.

[193] H.L. Bassett, S.H. Bomar Jr, Complex permittivity measurements during high temperature recycling of space shuttle antenna window and dielectric heat shield materials, (1973).

[194] S.-D. Zhang, C. Sun, F.-X. Sun, X.-L. Xia, Spectral properties of an UV fused silica within 0.8 to 5 μm at elevated temperatures, Infrared Physics & Technology, 85 (2017) 293-299.

[195] R. Kitamura, L. Pilon, M. Jonasz, Optical constants of silica glass from extreme ultraviolet to far infrared at near room temperature, Applied optics, 46(33) (2007) 8118-8133.

[196] C. Tan, J. Arndt, Temperature dependence of refractive index of glassy SiO2 in the infrared wavelength range, Journal of Physics and Chemistry of Solids, 61(8) (2000) 1315-1320.

[197] J. Wray, J.T. Neu, Refractive index of several glasses as a function of wavelength and temperature, JOSA, 59(6) (1969) 774-776.

[198] E. Beder, C. Bass, W. Shackleford, Transmissivity and absorption of fused quartz between 0.22 μ and 3.5 μ from room temperature to 1500° C, Applied Optics, 10(10) (1971) 2263-2268.

[199] O.J. Edwards, Optical transmittance of fused silica at elevated temperatures, JOSA, 56(10) (1966) 1314-1319.

[200] B. Hay, J. Filtz, J. Hameury, L. Rongione, Uncertainty of thermal diffusivity measurements by laser flash method, International journal of thermophysics, 26(6) (2005) 1883-1898.

[201] D.G. Cahill, Thermal conductivity measurement from 30 to 750 K: the 3ω method, Review of scientific instruments, 61(2) (1990) 802-808.

[202] K.L. Wray, T.J. Connolly, Thermal conductivity of clear fused silica at high temperatures, Journal of Applied Physics, 30(11) (1959) 1702-1705.

[203] R. Viskanta, E. Anderson, Heat transfer in semitransparent solids, in: Advances in heat transfer, Elsevier, 1975, pp. 317-441.

[204] T. Kunc, M. Lallemand, J. Saulnier, Some new developments on coupled radiative-conductive heat transfer in glasses—experiments and modelling, International journal of heat and mass transfer, 27(12) (1984) 2307-2319.

[205] D.F. Hanks, Z. Lu, J. Sircar, I. Kinefuchi, K.R. Bagnall, T.R. Salamon, D.S. Antao, B. Barabadi, E.N. Wang, High Heat Flux Evaporation of Low Surface Tension Liquids from Nanoporous Membranes, ACS Applied Materials & Interfaces, 12(6) (2020) 7232-7238.

[206] N.P. Bansal, D. Zhu, Effects of doping on thermal conductivity of pyrochlore oxides for advanced thermal barrier coatings, Materials Science and Engineering: A, 459(1-2) (2007) 192-195.